

In-Plasma Photo-Assisted Etching of Silicon in a High-Density Chlorine Discharge

by
Emilia W. Hirsch

A dissertation submitted to the Department of Chemical and Biomolecular Engineering,
Cullen College of Engineering
in partial fulfillment of the requirements for the degree of

DOCTOR OF PHILOSOPHY

in Chemical Engineering

Co-Chair of Committee: Vincent M. Donnelly

Co-Chair of Committee: Demetre J. Economou

Committee Member: Lars C. Grabow

Committee Member: Paul Ruchhoeft

Committee Member: John C. Wolfe

University of Houston
May 2020

Copyright 2020, Emilia W. Hirsch

Dedicated to
My husband Andrew, our parents, and our daughter Quinn

Acknowledgements

I would like to thank my advisors Dr. Vincent Donnelly and Dr. Demetre Economou for the support, guidance, and encouragement that they shared throughout my graduate study. I am lucky to have their input and direction while doing experiments. Their deep theoretical and experimental knowledge always led to thinking about problems in new and interesting ways.

Every time Dr. Donnelly came down to the lab, I would learn something new about the equipment I was using for the experiments I was performing. All the wires and Kapton tapes we pulled out together from the chamber taught me to think critically about every aspect of the experiment and pushed me to understand every facet of the system at a fundamental level. Dr. Economou graciously took his time to nominate me for Coburn and Winters Award. I appreciate that you think I deserve it. I also remember all the discussions with Dr. Economou for finishing up the paper. Outside work, Dr. Donnelly and Dr. Economou are genuinely nice and considerate. I will always appreciate the space and freedom afforded to me to think things through and do everything right on my project. I will miss working with both of you.

I would like to thank Dr. Grabow for serving on my committee since my PhD qualifying exam. He was very approachable, provided valuable insights, and taught me what Hirsch meant in German. To Dr. Paul Ruchhoeft and Dr. John Wolfe, thanks for taking time to serve on my dissertation defense committee. Additionally, thanks Dr. Ruchhoeft for the very helpful discussion on improving the sample contact with DC bias.

I would like to thank my former and current lab members for their support and cooperation. Special thanks to my coworker, Linfeng Du for the great teamwork and Dr. Shyam Sridhar and Dr. Lei Liu, currently at Applied Material and Lam Research respectively, for their guidance when I first joined the lab. This research could not have been completed without them.

I am also thankful to other group members: Dr. Qiaowei Lou, Dr. Sanbir S. Kaler, Dr. Tyler List, Dr. Tianyu Ma, Dr. Yongxin Liu, Dr. Kai Zhao, Hanyang Li, Ya-Ming Chen, Tam Nguyen, Ryan Sawadichai, Yingliang Zhou, Dong Zhang, Peng Lin, and Priyanka Arora. It was my pleasure working with them in the lab. I also want to thank Hanyang Li and Xiao Li for their help on my engineering core courses.

I would also like to recognize the department staff for their help and assistance on various issues. The administrative staff (Ms. Nicolette Solano, Ms. Patricia Cooks, Ms. Yolanda Thomas, and Ms. Hira Ahmed) were very helpful in processing purchases, reimbursements, and paperwork promptly. Special thanks to Mr. David Dawlearn for all the work related to lab safety. I would also like to thank our machinist Mr. Gerald Blosser. None of the experiments would have been possible without his precise machining work and helpful discussions.

I would like to thank my husband Andrew Hirsch for 10 years of support and sacrifice in this pursuit to find a good job in the US. Thanks to my daughter Quinn for being the constant motivation to work hard and make a nice life. And thanks to my parents and Andrew's parents for their selfless love, understanding, and encouragement throughout this long journey. None of this would have been possible without all of their love and support.

This work was supported financially by the National Science Foundation (PHY-1500518) and the Department of Energy, Office of Fusion Energy Science (DE – SC0001939).

Abstract

Plasma etching is indispensable in manufacturing of microelectronic devices. It involves the removal of material from selected regions of a substrate in a reactive plasma most often created by a radio-frequency (RF) powered gas discharge. The plasma serves as a source of neutral and ionic reactants, which combine with the atoms in the material to form volatile products. The anisotropic etching profile is achieved through the synergy between neutral species (radicals) and energetic ion bombardment, which is critical for precise pattern transfer, especially for features with lateral dimensions of <10 nm.

Low ion energies (10s eV) are required to further advance this capability to etch material with atomic resolution, low damage, and ultra-high selectivity. However, at low ion energies, photo-assisted etching (PAE) has been shown to be very important. In-plasma PAE is an alternative etching pathway catalyzed by vacuum ultraviolet (VUV) photons generated in the plasma, which could cause substantial complications for processes due to its comparable etching rate with ion-assisted etching (IAE), when ion energy is low, and its impact on profile evolution.

In this thesis, etching of p-Si in 60 mTorr 10%Cl₂/90%Ar Faraday-shielded inductively coupled, high density plasma was investigated under both ion-assisted etching (IAE) and photo-assisted etching (PAE) conditions. Real-time etching rates and after-etching Si surface chemical compositions were obtained by laser interferometry and vacuum-transfer X-ray photoelectron spectroscopy (XPS), respectively.

Precisely controlled ion energy distributions (IED) were obtained by applying pulsed negative DC bias on the conductive sample stage. Above a ~ 36 eV threshold at a

total flow rate of 250 sccm, the IAE rate increased with the square root of the ion energy. The corresponding PAE rate below the threshold energy was ~ 400 nm/min. At a relatively low flow rate (total flow rate of 50 sccm), the IAE threshold energy was ~ 25 eV and the PAE rate was ~ 300 nm/min. In contrast to DC bias, etching under RF bias did not exhibit a threshold ion energy because of the wide IED.

XPS spectra revealed that the surface layer under PAE conditions had a significantly lower chlorine content, composed of only SiCl. Under IAE conditions, however, silicon dangling bonds (Si \bullet), SiCl₂, and SiCl₃ were found on the surface, in addition to SiCl, with a relative abundance of SiCl>SiCl₂>SiCl₃. The absence of higher chlorides and Si \bullet under PAE conditions suggested that VUV photons and above threshold-energy ions interacted with the surface very differently.

By varying the duty cycle of the pulsed DC bias, it was found that the IAE rate scaled with the energetic ion dose, but only for low duty cycles. For higher duty cycles, the apparent IAE yield fell off with an *increasing* Cl coverage on the surface, as duty cycle went up, which pointed to a negative synergy (anti-synergism) between PAE and IAE as the explanation. This anti-synergism was further supported by the observed decrease of the total etching rate with increasing period of the pulsed DC bias. A plausible mechanism was that increasing the pulsing period caused more near-surface damage, creating more recombination centers that led to higher loss rate of electron-hole pairs through recombination, thereby reducing the PAE rate.

Table of Contents

Acknowledgements	iv
Abstract	vii
Table of Contents	ix
List of Tables	xii
List of Figures	xiii
Chapter 1 – Introduction	1
1.1 Plasmas etching in semiconductor processing	1
1.2 Photo-assisted etching	5
1.3 Scope of this research.....	8
Chapter 2 – Literature Review	10
2.1 PAE in the absence of a plasma	10
2.2 In-plasma PAE	22
2.2.1 Discovery of in-plasma PAE	22
2.2.2 Wavelength dependence of PAE	27
2.2.3 Surface morphology of PAE.....	28
2.2.4 Pros and cons of in-plasma PAE	30
2.3 IAE yield and threshold.....	31
Chapter 3 – Apparatus and Methods.....	36
3.1 Experimental setup.....	36
3.1.1 Inductively coupled plasma (ICP) source.....	37
3.1.2 Sample bias setup	41
3.1.3 Sample preparation	42
3.2 Etching rate measurements.....	46
3.2.1 Laser interferometry	46
3.2.2 Spectroscopic ellipsometry.....	48
3.3 Surface characterization	50
3.3.1 X-ray photoelectron spectroscopy	50

3.3.2 Scanning electron microscopy (SEM)	55
Chapter 4 – Comparison of Silicon Surface Chemical Composition between IAE and PAE	56
4.1 Introduction	56
4.1.1 Nature of the chlorinated surface layer of Si (100) after etching under IAE condition	56
4.1.2 Surface chemistry composition of trench sidewalls for SiO ₂ -masked Si (100) after etching under IAE condition	63
4.2 Experimental details – high resolution spectra fitting procedure.....	66
4.3 Results and discussion.....	68
4.3.1 Low resolution survey spectra.....	68
4.3.2 High resolution spectra.....	72
4.3.3 High resolution peak fitting.....	73
4.3.4 Duty cycle dependence of the Cl coverage	78
Chapter 5 – Anti-synergism Between IAE and In-Plasma PAE of Silicon in a High-Density Chlorine Plasma.....	80
5.1 Introduction	80
5.2 Experimental details	85
5.3 Results and discussion.....	87
5.3.1 Etching rate – ion energy dependence	87
5.3.2 Etching rate – duty cycle dependence	97
5.3.3 Mechanism.....	104
Chapter 6 – Summary, Conclusions, and Future Directions.....	113
6.1 Summary and conclusions.....	113
6.2 Future work	115
6.2.1 Plasmonics	115
6.2.2 Turning off PAE.....	117
References.....	119
Appendices.....	128
Appendix A: Related calculations.....	128
A.1 Ion collision probability in the sheath	128

A.2 Charging of SiO ₂ mask	129
A.3 Chlorine consumption.....	129
A.4 IAE yield.....	131
A.5 Plasma density	131
A.6 Cl neutral flux	132
A.7 VUV photon flux and PAE yield.....	133
A.8 Electron impact ionization rate constant.....	133
Appendix B: Hardware modifications to eliminate contamination and improve run-to-run reproducibility	135
B.1 Results obtained with chamber contamination	135
B.2 Origin of the contaminations	138
B.3 Contamination elimination.....	139
B.4 Secondary Plasma Elimination	140
B.5 Source Stability	141

List of Tables

Table 4.1: Normalized elemental composition and relative chlorine concentration measured by XPS low resolution survey spectra at take-off angles of 30° and 85° for blanket p-Si after etching in 60 mTorr Cl ₂ /Ar plasma at low flow rate with the sample stage powered by RF (-70V and -140V self-bias) or without any bias (0 V, grounded).	68
Table 5.1: Threshold values of IAE of Si with chlorine reported in the literature.	95

List of Figures

Figure 1.1: Comparison between wet etching which relies on chemically reactive species to leave an isotropic etching profile (left) and plasma etching which also employs ion bombardment to give an anisotropic etching profile (right). ⁵	2
Figure 1.2: Ion and neutral synergism for semiconductor etching process. ¹¹	3
Figure 1.3: Number of ALE publications per year from 1988 to 2014. The first wave of publications occurred in the 1990s. ¹⁴	4
Figure 1.4: Absolute etching rate at 50mTorr as a function of $E^{1/2}$ (E = ion energy) in a 1%Cl ₂ /99%Ar plasma pulsed at 10kHz with a duty cycle of 20%. The bias was applied 50 μ s into the afterglow (i.e., at $t = 70 \mu$ s) until $t = 98 \mu$ s. ¹⁷	6
Figure 2.1: Undoped poly-Si etching characteristics under different photoirradiation methods. The Cl ₂ pressure was 10 Torr. ²⁰	10
Figure 2.2: Etching rates of n ⁺ , undoped, and p ⁺ poly-Si as a function of sheet resistance. The samples were prepared with ion implantation at doses of $1 \times 10^{16} \text{ cm}^{-2}$ (150 keV for phosphorus and 50 keV for boron). The sheet resistance was changed by heat treatment at 550 °C for 40 minutes and 1000 °C for 40 minutes. ²⁰	12
Figure 2.3: Laser power dependence of the product signals during photochemical etching of n-type Si. (a) ion signals for fluorosilyl products and reflected, unreacted XeF ₂ normalized to values for spontaneous etching (no laser); (b) branching ratios for the two principal products, SiF ₄ and SiF ₃ . ²¹	13
Figure 2.4: Intensity dependence of SiF ₃ and SiF ₄ formation on n-type Si. ²¹	14
Figure 2.5: Etching rate of Si as a function of 308 nm XeCl-excimer-laser fluence for various Cl ₂ pressures. The temperatures indicated on the upper scale were calculated. ³⁷	16
Figure 2.6: Etch rate as a function of laser energy fluence for a Si (100) surface exposed to 0.7 mbar Cl ₂ at a gas flow rate of 20 sccm. Excimer laser radiation of 248 and 308 nm was used at 20 pulses per second (pps) pulse repetition rate. The etch rate curves consisted of three energy fluence ranges (I), (II), and (III) characterized by the straight lines. ²²	17
Figure 2.7: Thermal desorption spectra monitored prior and subsequent to exposure to UV radiation for increasing (A)-(C) chlorine coverage. ³⁹	19
Figure 2.8: Effects of photon irradiation (power: 38 mW/cm ² , frequency: 8 Hz) on etching depth as a function of RF bias power during Cl neutral beam etching. The Si etching depth was measured using AFM. The irradiated photon wavelength was controlled by UV photon filter. ²³	20
Figure 2.9: Dependence of etching depth on photon irradiation power at the same neutral beam energy and flux. ²³	20

Figure 2.10: Selective etching efficiency of Si/XeF ₂ on both linear scale and logarithmic scale. ⁴¹	21
Figure 2.11: IEDs generated by applying a synchronous DC bias on a boundary electrode for a specified time window during the afterglow of a pulsed Ar plasma. ¹⁷	22
Figure 2.12: Relative Si etching rates (intensity of Si 2882 Å emission) at different pressures, and absolute etching rate at 50 mTorr (hollow triangles) as a function of $E^{1/2}$ in 1%Cl ₂ /99% Ar plasma pulsed at 10 kHz with a duty cycle of 20%. The bias was applied 50 µs into the afterglow (from 70 µs to 98 µs). ¹⁷	23
Figure 2.13: Si etching rates as a function of the square root of ion energy with pulsed DC bias at 10 kHz and 50% duty cycle on the sample stage. Absolute etching rates of blanket p-type Si were obtained by calibration of the relative intensity of Si 2882 Å emission with the measured absolute etching rates (hollow stars). ¹⁸	24
Figure 2.14: PAE rates of blanket p-type Si measured by stylus profilometer in different halogen plasmas (red) and the product of the total surface halogen coverage (Cl + Br) and Ar emission (750.4 nm) intensity (green). ¹⁸	25
Figure 2.15: Time resolved normalized emission intensities recorded during Si etching in a 50%Cl ₂ /50%Ar plasma where power was modulated between 500 and 300 W at a frequency of 1 kHz and 50% duty cycle. ¹⁹	26
Figure 2.16: Absolute etching rates (calibrated based on the Si emission) under different window materials as a function of $E^{1/2}$ in 50% Cl ₂ /50% Ar plasmas. ¹⁸	28
Figure 2.17: (a) 25 µm ² AFM image of p-Si etched in 50%Cl ₂ /50%Ar plasma at 0V bias for 2 minutes. (b) 3D view showing the pyramidal features. (c) (110) planes that formed the faces of the pyramidal feature. ¹⁸	29
Figure 2.18: Cross sectional scanning electron microscope (SEM) image of a patterned (100 nm lines and 100 nm spaces with 30 nm oxide mask on top) p-type Si sample after 10 min. etching in 1%Cl ₂ /99%Ar pulsed plasma at 50 mTorr under PAE condition. ¹⁷	30
Figure 2.19: Ion-enhanced polysilicon etching yield vs. Cl atom to Ar ⁺ ion flux ratio. An initial sharp rise in the etching yield was observed at low flux ratios where reaction was limited by the supply of reactive neutrals. The etching yield then gradually saturated as the reaction became ion-flux limited at higher flux ratios. Dotted lines were fits of a surface kinetic model. ⁴⁶	32
Figure 2.20: Model fitted parameters of etching yield (β) and Cl sticking coefficient (s) as a function of square root of ion energy for Ar ⁺ /Cl etching of polysilicon. The extrapolated threshold energy was 16 eV. ⁴⁶	32
Figure 2.21: Etching yield of polysilicon by Cl ⁺ -Cl, Cl ₂ ⁺ , and Cl ⁺ as a function of the square root of ion energy. The etching yields of polysilicon by utilizing Cl ⁺ and Cl beams were taken in the saturation regime with flux ratio ≥ 300 . ⁴⁷	33
Figure 2.22: Ion-enhanced polysilicon etching yield vs. Cl atom to Ar ⁺ ion flux ratio at three different ion energy levels. ⁴⁷	34

Figure 2.23: Etching yield as a function of the square root of incident ion energy. ⁴⁸	35
Figure 3.1: Experimental apparatus.	36
Figure 3.2: Schematic of the plasma source. The Faraday-shielded ICP reactor was equipped with a He-Ne laser interferometry setup for real time etching rate measurements.	38
Figure 3.3: Schematic of the Π -matching network circuit used in this work. The variable capacitors and the inductor could be tuned to minimize the reflected power.	39
Figure 3.4: Voltage waveform measured on the floating SS sample stage at pressure 60 mTorr while plasma was on.	40
Figure 3.5: Pressure at the measurement (gauge) location (black), and pressure in the plasma region (red) vs. gas flow rate.	41
Figure 3.6: Top view (left) and side view (right) of sample (blue) on top of Si disk (grey) and sample holder (black).	44
Figure 3.7: I-V curve measured at atmospheric pressure for sample + Si disk + sample holder both before etching (black squares) and after etching (red dots).	45
Figure 3.8: A sample interferogram.	47
Figure 3.9: Schematic setup of an ellipsometry experiment (from wikipedia.org).	49
Figure 3.10: Schematic setup of XPS measurements. ⁶⁰	51
Figure 3.11: Principle of angle-resolved XPS. ⁶³ Detection depth decreases as take-off angle decreases, resulting in a more surface sensitive analysis.	53
Figure 3.12: Diagram of photoelectric process (left) and Auger process (right). ⁶⁴	54
Figure 4.1: Schematic of the helical resonator plasma reactor and attached UHV/XPS chamber. ⁶⁵	57
Figure 4.2: Cl(2p)/total Si(2p) signals (corrected with sensitivity factors) vs. θ in the near-surface region of Si (100) samples after etching for 30 s in Cl ₂ plasmas under different processing conditions. The points are experimental data, and the curves are fits. The inset shows data (for 0 V bias) after etching for an additional 270 s for a total 300 s. ⁶⁵	58
Figure 4.3: High resolution Si(2p) spectra at $\theta=30^\circ$ of: (a) HF-cleaned Si, Ar ⁺ -sputtered-cleaned Si, and plasma etched (RIE, -240 V self-bias) Si, (b) plasma etched Si with a Shirley-shaped background subtraction and 2p _{1/2} components removed. The fit (solid line) of the XPS spectrum (dots) included five peaks (dashed lines) with 85% Gaussian and 15% Lorentzian line shapes. ⁶⁵	59
Figure 4.4: Depth profiles for bulk Si, Si●, SiCl, SiCl ₂ , and SiCl ₃ , determined from an inversion of take-off angle dependent XPS data for plasma etched Si (100) under RIE conditions at -240 V self-bias. ⁶⁵	60

Figure 4.5: Schematic depiction of Si (100) surfaces after etching in a Cl ₂ plasma for (a) RIE, -240 V self-bias (280 eV mean ion energy) and (b) HR, 0 V bias (40 eV mean ion energy). ⁶⁵	61
Figure 4.6: High resolution Si(2p _{3/2}) XPS spectrum acquired at $\theta = 30^\circ$ for Si etched in (a) 10.0 and (b) 0.4 sccm Cl ₂ plasma. Empty squares are experimental. Broken lines are fits. ⁷⁶	63
Figure 4.7: (a) Overlay of Si(2p) spectra from the 1.0 μm region, etched in a 1.4 sccm Cl ₂ plasma, acquired at $\theta=30^\circ$ (sidewall, solid line) and 85° (trench bottom, solid triangles-line). Also shown are corresponding spectra from the unmasked Si (100) area obtained at $\theta_{\text{eff}}=60^\circ$ (open circles-line) and $\theta=85^\circ$ (dotted line). (b) same for 0.5 μm region. ⁷⁷	65
Figure 4.8: Surface chemical structure model of silicon single crystal after UV/HF cleaning with 1% HF solution. ⁸¹	67
Figure 4.9: Peak fitting of high resolution Si(2p) spectrum at take-off angle 30° for p-Si after HF treatment.	67
Figure 4.10: XPS low resolution survey spectra at take-off angle of 30° and 85° for Si after etching at low flow rate.	69
Figure 4.11: Relative chlorine concentration after etching in 60 mTorr Cl ₂ /Ar plasma obtained from XPS survey spectra at take-off angles of 30° (black squares) and 85° (red circles) at low flow rate.	71
Figure 4.12: High resolution Si(2p) spectra at take-off angles of 30° or 85° . Etching conditions were 0V (PAE), RF at -70V self-bias, and RF at -140V self-bias, all at low flow rate. Intensities were normalized at the maximum near 100 eV.	73
Figure 4.13: Peak fitting of high resolution Si(2p) spectra at take-off angle of 30° . Etching conditions were (a) 0V (PAE), (b) RF, -70V self-bias, and (c) RF -140V self-bias, all at low flow rate.	75
Figure 4.14: Relative chlorine concentration after etching in 60 mTorr Cl ₂ /Ar plasma obtained from XPS survey spectra at take-off angles of 30° (black squares) at low flow rate. Black stars were calculated based on the integrated areas of deconvoluted SiCl _x peaks obtained by high resolution XPS at 30° .	77
Figure 4.15: Relative chlorine concentration obtained from XPS survey spectra at take-off angle 30° . Etching conditions were RF -70 V self-bias (blue solid square) and pulsed -70 V DC bias at 10 kHz for low flow rate (black solid squares) and high flow rate (red solid dots). The inset is an enlargement of the region with duty cycle less than 10%.	78
Figure 4.16: High resolution Si(2p) spectra at take-off angle 30° . Etching conditions were 0V (PAE) and RF at -70V self-bias at low flow rate. Intensities were normalized at the maximum near 100 eV. The black dashed line is from a sample etched under pulsed -70V DC bias with 50% duty cycle at 10 kHz, also at low flow rate.	79

Figure 5.1: Synergistic etching of Si by Ar ⁺ ion beam sputtering and XeF ₂ chemical etching. Ar ⁺ energy = 450 eV, Ar ⁺ current = 0 (t < 200 sec), Ar ⁺ current = 2.5 μA (t > 200 sec), XeF ₂ flow = 2 × 10 ¹⁵ mol/sec (t < 660 sec), and XeF ₂ flow = 0 (t > 660 sec). ⁹	81
Figure 5.2: Surface roughness of the 193 nm photoresist after ion-only [(a)-(d)] and simultaneous ion + UV/VUV exposure [(e)-(h)] from 50 to 100 °C as observed with 1 × 1 μm ² AFM images. Color scale is 2.5 nm. All line plots are on the same scale with a 5 × exaggerated vertical axis. ²⁶	82
Figure 5.3: SiN _x :H and SiO ₂ etch rates caused by the interaction between VUV/UV radiation and radicals under various pallet for plasma evaluation (PAPE) conditions: (a) VUV/UV radiation (> 115 nm) and radicals, (b) UV radiation (> 170 nm) and radicals, (c) UV radiation (> 300 nm) and radicals, (g) radicals, and (h) plasma exposure. ²⁴	83
Figure 5.4: (a) AFM images and line profiles of the GaN surfaces in the initial state, after plasma etching, after radical exposure, and after simultaneous irradiation of photons and radicals. (b) Cross-sectional SEM images of the etch profiles of the GaN films after radical exposure and after simultaneous irradiation of photons and radicals. ²⁸	84
Figure 5.5: Substrate current measurements with Pearson current probe for 10 kHz, -60 V DC bias at 10%, 50%, and 90% duty cycle.	87
Figure 5.6: Absolute etching rates of SiO ₂ as a function of E ^{1/2} (E = ion energy) for low flow rate under pulsed negative DC bias at 10 kHz with 50% duty cycle (blue triangles) or RF bias (blue open triangles).	89
Figure 5.7: SEM images of patterned sample after etching with pulsed DC bias at 10 kHz and 50% duty cycle (left) and RF bias (right) -60V at high flow rate.....	90
Figure 5.8: Absolute etching rates of p-Si as a function of E ^{1/2} (E = ion energy) with RF bias (black squares for low flow rate and magenta stars for high flow rate).....	91
Figure 5.9: Ar ⁺ ion energy distribution averaged over the wafer for an ICP power deposition of 500 W, RF bias of 100 V, and -31 V calculated DC bias on the substrate reported by Hoekstra <i>et al.</i> ⁹⁵	92
Figure 5.10: Absolute etching rates of p-Si as a function of E ^{1/2} (E = ion energy) with the application of pulsed negative DC bias at 10 kHz and 50% duty cycle (red dots for low flow rate and green dots for high flow rate).	93
Figure 5.11: Definition of IAE threshold for this work (blue) and the study by Sawin and co-workers (red).	96
Figure 5.12: IAE yield of p-Si as a function of E ^{1/2} (E = ion energy) with the application of pulsed negative DC bias at 10 kHz and 50% duty cycle for high flow rate (derived from green dots in Figure 5.10).	97
Figure 5.13: Total etching rate (both IAE and PAE) of p-Si as a function of duty cycle with -60 V pulsed DC bias at 10 kHz (black squares) for (a) low flow rate and (b) high flow rate. The PAE rate (0% duty cycle) was set as the origin on the left y-axis. The	

corresponding integrated energetic ion current per cycle is also shown (blue line and open circles).....	99
Figure 5.14: Time resolved energetic ion current measured on sample holder for a full period with the application of -60 V pulsed DC bias at 10 kHz (100 μ s per period) for (a) low flow rate and (b) high flow rate for duty cycle 10% - 90%.	101
Figure 5.15: Etching rate vs aspect ratio at 10 mTorr by Lane <i>et al.</i> with Lam Research model 9400SE TCP. ¹⁰²	103
Figure 5.16: Ion (solid symbols) and electron (open symbols) density as a function of position and pressure measured by the Langmuir probe for CW plasma at 300 W and 40 sccm. The plasma potential and the electron temperature measured by the Langmuir probe at Z = 170 mm (location of RFEA) are shown in parentheses next to the corresponding pressure. ⁹⁴	104
Figure 5.17: Etching yields as a function of pulsed DC bias duty cycle, derived from Figure 5.13 (b). The PAE relative yield (red line) was assumed to smoothly transition from 0 in the limit of zero Cl-to-ion flux ratio (f_{Cl}/f_+), to unity at high f_{Cl}/f_+ values. The corrected IAE yields (blue \times 's) account for a declining PAE rate as f_{Cl}/f_+ decreases with increasing bias duty cycle. Estimated f_{Cl}/f_+ values as a function of bias duty cycle are included (green line).	105
Figure 5.18: Uncorrected (black squares) and corrected (red triangles) Si etching yield at high flow rate as a function of Cl-to-Cl ⁺ flux ratio derived from Figure 5.13 (b). .	106
Figure 5.19: Total etching rate (sum of IAE and PAE) as a function of pulsed DC bias period with 50% duty cycle, and for negative bias voltage of 60V (black) and 100V (red), at high flow rate.	109
Figure 5.20: Three types of carrier recombination mechanisms in semiconductors. ¹¹⁰ .	111
Figure 5.21: Electron capture cross sections of the gold donor and acceptor (left) and hole capture cross sections of the gold donor and acceptor (right) as a function of temperature. The symbols represent different samples. ¹¹²	112
Figure 6.1: Simulation of light intensity (W/m ²) for a planewave ($\lambda=106.7$ nm, 1V/m) normally incident onto a 30 nm-thick SiO ₂ mask with L/S=100nm, on top of Si. Strong light intensity is observed at the trench corners. ¹¹⁵	116
Figure B.1: An XPS survey spectrum of p-type Si after etching in pure Cl ₂ plasma for 1 minute at 4 mTorr with RF self-bias voltage -140 V.	136
Figure B.2: High resolution Si(2p) spectra at $\theta = 30^\circ$ of sample in the center of the plasma (black) and downstream of the plasma (red), etched with -70 V self-bias voltage.	137
Figure B.3: SEM image (measured at 45° angle) of p-Si after etching for 1minute in Ar/Cl ₂ plasma at pressure 60 mTorr with -70 V bias applied on sample.....	138
Figure B.4: Sample stage after modifications to eliminate contamination and secondary plasma.	139

Chapter 1 – Introduction

1.1 Plasmas etching in semiconductor processing

Plasma is often thought of as the fourth state of matter besides solid, liquid, and gas, and it is the most common state of matter in the universe.¹ “Our” plasma is a partially ionized gas consisting of electrons, ions (both negatively and positively charged), photons, and mostly neutral species (atoms and molecules) that exhibits collective behavior. Compared with ordinary neutral gases, plasmas can be strongly influenced by electric and magnetic fields due to the presence of charged particles, which forms the foundation of the wide application of plasmas in semiconductor processing. Its non-thermodynamic-equilibrium nature is also critical, where the electron temperature is much higher than the temperature of heavy particles (ions and neutrals). These low-temperature plasma processes have played important roles in the major advances in very large-scale integration (VLSI) devices for both material deposition and etching.

Microelectronics based on semiconductors and integrated circuits continue to be developed for various applications, especially information processing and transmission.² However, further development demanded by the information age is limited by the density of the circuits and the performance of electronic components.³ Etching in particular is a critical step in the fabrication of integrated circuits, allowing fine lithographic patterns to be precisely transferred onto the thin films on a wafer. In addition, etching can also be used for wafer cleaning to remove contaminants and residues from the previous processing steps.

Before 1975, wet-etching, which utilized liquid acid or base solutions to etch material, was used exclusively for pattern transfer in integrated-circuit (IC) manufacturing. Over the past 50 years, however, plasma etching (also called dry etching or ion-assisted etching) has replaced wet etching for most if not all the pattern transfer steps.⁴ Nowadays, in the fabrication of ultra-large-scale ICs with nanoscale and even the atomic scale device dimensions, plasma etching continues to play a major role. To a large extent, this is because directional ions bombarding the substrate give rise to anisotropic etching profiles and high-fidelity pattern transfer. Figure 1.1 shows the comparison between wet etching which relies on chemically reactive species to leave an isotropic etching profile and plasma etching which also employs ion bombardment to give an anisotropic etching profile.⁵ Additional advantages are that plasma etching can remove materials that cannot be easily removed by wet etching, and elimination of chemical waste produced by wet etching.⁶⁻⁸

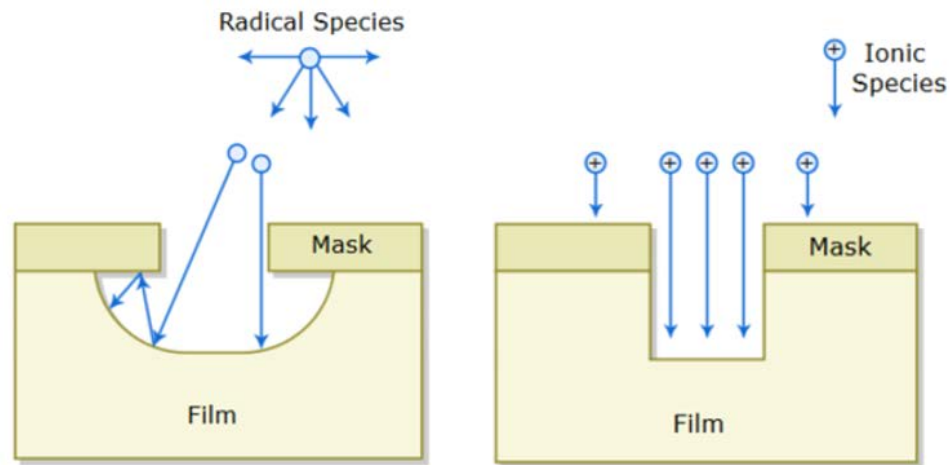


Figure 1.1: Comparison between wet etching which relies on chemically reactive species to leave an isotropic etching profile (left) and plasma etching which also employs ion bombardment to give an anisotropic etching profile (right).⁵

Plasma etching occurs through a synergy between ions and neutrals, as first demonstrated in a seminal paper by Coburn and Winters in 1979.⁹ Ion bombardment promotes reactions of chemisorbed neutrals with the substrate atoms, resulting in formation of products that desorb.⁹ Figure 1.2 shows the ion and neutral synergism for semiconductor etching process. Although great progress has been made through separate control of ion energy and flux, as well as neutral-to-ion flux ratio, great challenges still remain as the critical dimension of devices approaches the atomic scale.¹⁰

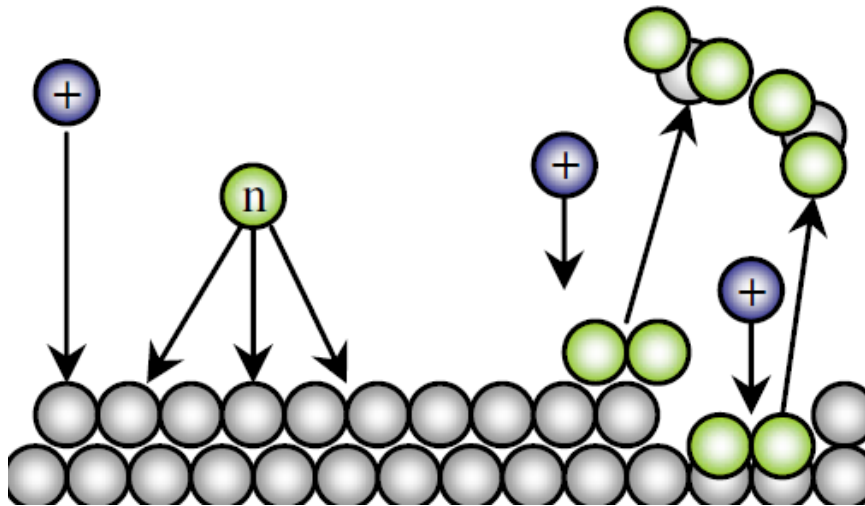


Figure 1.2: Ion and neutral synergism for semiconductor etching process.¹¹

The emerging consensus is that as critical dimensions approach the sub-10 nm scale, the need for atomic layer etching (ALE) will become essential, which allows etching of ultrathin films with monolayer accuracy, high selectivity over other material, low surface roughness, and minimal damage to underlying materials. An ideal ALE process occurs with substrate thickness loss of ~ 1 monolayer per cycle. The quest to replace continuous directional plasma etching methods for critical applications by a sequence of

individual, self-limited surface reaction steps has reached a crucial stage.^{12,13} Over the past 30 years, a variety of materials have been studied to achieve ALE including III-IV material (such as GaAs and InP), Si, SiO₂, Si₃N₄, Al₂O₃, TiO₂, HfO₂, Ge, and graphene.¹³ Figure 1.3 shows a resurgence of ALE activity after a slower pace of publications in the 2000s.¹⁴

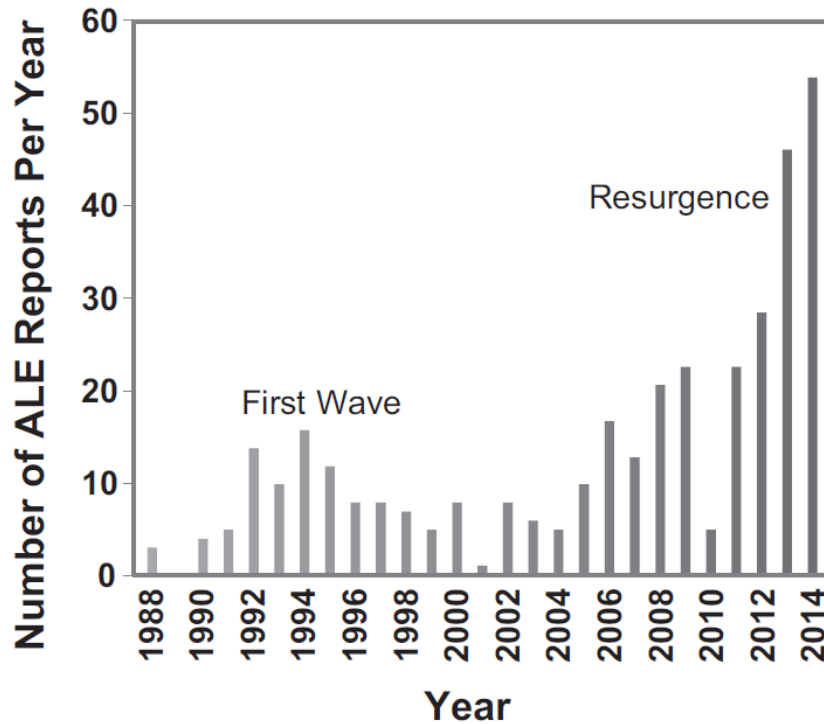


Figure 1.3: Number of ALE publications per year from 1988 to 2014. The first wave of publications occurred in the 1990s.¹⁴

In realizing ALE, delivering ion energy within a very specific range is extremely important. In the meantime, narrow ion energy and angular distributions are also desirable.¹⁴⁻¹⁶ The ion energy must not be high enough to damage the underlying material by physical sputtering nor too low to drive a synergistic etching reaction on the surface. The ion energy must be controlled so that the ALE process is self-limiting, i.e., no etching

occurs in the absence of ion bombardment or when the reactive layer formed on the surface of the material being etched has already been completely removed by ion bombardment.

1.2 Photo-assisted etching

In-plasma photo-assisted etching (PAE) of p-type Si was first reported by Shin *et al.* in 2011. This phenomenon was discovered in mostly Ar plasma with a few percent Cl₂ added.¹⁷ Nearly monoenergetic ion energy distributions (IEDs) were obtained by applying a synchronous DC bias on a “boundary electrode” during the afterglow of a pulsed, inductively coupled, Faraday-shielded plasma.¹⁷ The precisely controlled IEDs was critical to study the silicon etching rate as a function of ion energy, especially at the near-threshold energies. It was found that etching rates increased with the square root of the ion energy above the observed threshold of 16 eV. When the ion energy was below the IAE threshold, an unexpected substantial etching rate was observed, independent of ion energy (shown in Figure 1.4). After a series of experiments ruling out the possibilities of chemical etching by Cl atom, etching assisted by Ar metastables, and etching mediated by holes and/or low energy electrons generated by Auger neutralization of low-energy ions, this sub-threshold etching was shown to be induced mainly by the native vacuum ultraviolet (VUV) photons generated in the plasma. Under these conditions, the PAE rate was equal to the ion-assisted etching (IAE) rate at 36 eV, causing substantial complications for processes that require low ion energies to achieve high selectivity and low damage, such as ALE. PAE was also found to play an important role in profile evolution of features etched in Si with chlorine-containing plasma, contributing to the commonly observed sloped sidewalls and nanotrenches.¹⁷

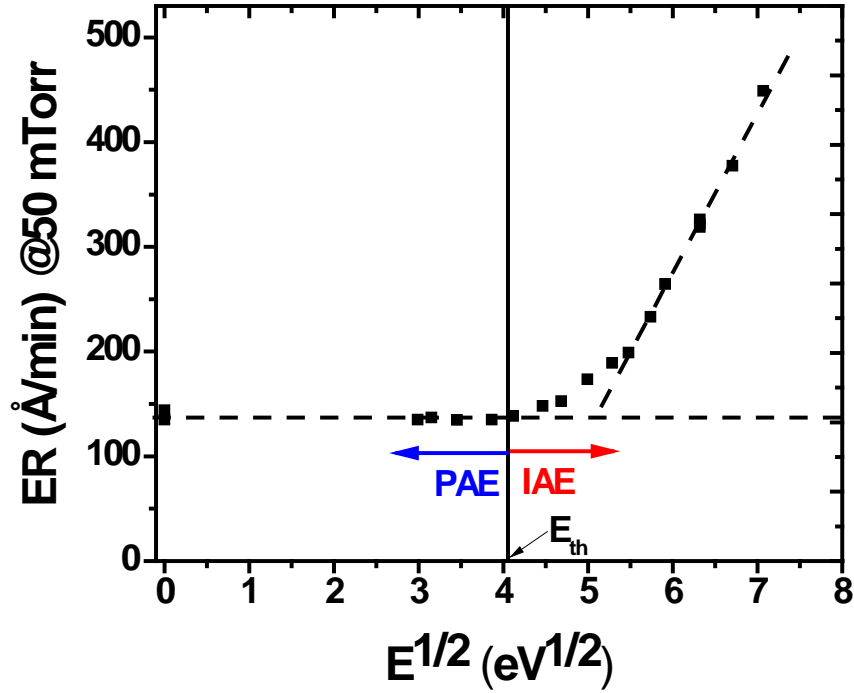


Figure 1.4: Absolute etching rate at 50mTorr as a function of $E^{1/2}$ (E = ion energy) in a 1%Cl₂/99%Ar plasma pulsed at 10kHz with a duty cycle of 20%. The bias was applied 50 μ s into the afterglow (i.e., at $t = 70 \mu$ s) until $t = 98 \mu$ s.¹⁷

In 2014, Zhu *et al.* measured the relative etching rates of silicon in different halogen containing plasmas including Cl₂, Br₂, HBr, Br₂/Cl₂, and HBr/Cl₂ feed gases diluted in Ar (50%-50% by volume), with a focus on the PAE component.¹⁸ In all cases, etching at ion energies below the IAE threshold was observed, and PAE rates were found to be the lowest in 50%Br₂/50%Ar plasma and the highest in 25%HBr/25%Cl₂/50%Ar plasma. The PAE rate scaled with the product of halogen surface coverage, measured by X-ray photoelectron spectroscopy (XPS), and optical emission intensity (Ar 7504 Å, a proxy for VUV emission). The dependence of PAE on wavelength was investigated by measuring the etching rates of silicon placed under windows with different light transmission characteristics. It was found that VUV photons with wavelength < 120 nm were much more

effective in inducing etching than longer wavelength. Atomic force microscopy (AFM) revealed that PAE could be sensitive to crystal orientation with the formation of 4-sided pyramidal features with bases that formed an angle of 45° with respect to $\langle 110 \rangle$ cleavage planes.¹⁸

In 2016, potential mechanisms of PAE were studied by Sridhar *et al.* with optical emission spectroscopy (OES).¹⁹ PAE in the absence of a plasma had previously been attributed to the creation of electron-hole pairs and reactions of these carriers at the surface,^{20,21} the enhancement of photo-desorption,²² and the surface damage induced by VUV photons, facilitating etching.^{22,23} Emissions from Cl, Si, SiCl, and Ar were recorded as a function of power while etching p-Si in Cl₂/Ar Faraday-shielded inductively coupled plasmas (ICPs) at a pressure of 60 mTorr with no substrate bias. Under these conditions, IAE was negligible and PAE was dominant. The Si:Ar optical emission intensity ratio, $I_{\text{Si}}/I_{\text{Ar}}$ (proportional to the etching rate of Si), increased substantially with power. Time resolved emissions were also recorded in a pulsed plasma at a rate that was much faster than that required to remove a silicon monolayer, where power was modulated between 500 and 300 W. $I_{\text{Si}}/I_{\text{Ar}}$ was found to modulate with the instantaneous power. This ruled out the photon-induced damage mechanism since, if this mechanism was dominant, the $I_{\text{Si}}/I_{\text{Ar}}$ signal would not be modulated.¹⁹

Up until recently, besides our group, very few investigators had reported on the possible synergy of radicals, ions, and photons originating from the same plasma. Fukasawa *et al.* demonstrated photo-enhanced etching of hydrogenated silicon nitride (SiN_x:H) films in fluorocarbon plasmas.^{24,25} Modification of surface morphology, attributed to plasma-generated VUV photons, was also reported. Enhanced surface

roughness was observed due to synergy among VUV photons, ion bombardment, and heating of plasma-exposed 193 nm photoresist by Nest *et al.*²⁶ Pargon *et al.* found VUV light (110-210 nm) to be the main contributor to decreased linewidth roughness of 193 nm photoresist after plasma etching.²⁷ Simultaneous irradiation by UV photons resulted in decreased surface roughness of GaN etched in chlorine plasmas.²⁸ Tian *et al.* discussed the control of relative fluxes of ions and VUV photons through pressure, pulsed power, gas mixture, and wall condition in low-pressure ICPs using model predictions.^{29,30}

1.3 Scope of this research

Depending on the application, PAE can be advantageous or an unwanted complication. For example, PAE was used to perform extremely selective etching of nanoholes in silicon using native oxide as a mask.^{31,32} On the other hand, PAE can be a problem for self-limited ALE processes where very low ion energies are used (to promote selectivity), for which the non-self-limiting PAE rate is comparable to the IAE rate.¹² In any case, it is important to understand the nature of plasma-surface interactions, specifically the role played by VUV photons. A mechanistic insight into PAE could provide clues on how to enhance or reduce PAE relative to IAE.

In this work, etching of p-type Si in Cl₂/Ar Faraday-shielded inductively-coupled high density plasmas was investigated under conditions where the ion energy could be precisely controlled resulting in clear transition from IAE to PAE. Vacuum-transfer XPS and laser interferometry were employed to study the near-surface chemical composition and measure *in-situ* and in real-time the etching rate of Si, respectively. The relative importance of IAE compared to PAE was controlled by varying the level and duty cycle of

a pulsed negative DC bias applied on the substrate holder. A major goal of this study was to shed light into any possible synergy during the in-plasma simultaneous bombardment of silicon by energetic (i.e., above threshold-energy) ions and photons, especially those in the VUV wavelengths. The surface chemical composition after etching under PAE condition was also studied and compared with its counterpart under IAE condition.

Chapter 2 – Literature Review

2.1 PAE in the absence of a plasma

Photo-assisted etching of Si with halogens in the absence of a plasma has been studied by various research groups. In 1985, Okano *et al.* found that n^+ poly-Si could be etched spontaneously by chemical reaction with Cl radicals photodissociated in the gas phase, while undoped and p^+ poly-Si could not be etched without direct ultraviolet (UV) irradiation emitted from a Hg-Xe lamp (energy density 275 mW/cm^2 after focus), as shown in Figure 2.1.²⁰

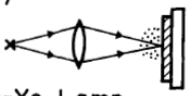

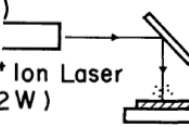
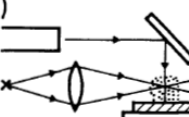

Etching Condition	Etched Depth/3h
(i)  Hg-Xe Lamp	7000 Å
(ii)  Hg-Xe Lamp	No Etching
(iii)  Ar ⁺ Ion Laser (2 W)	No Etching
(iv)  Hg-Xe Lamp	1000 Å
(v)  Ts = 200°C	No Etching

Figure 2.1: Undoped poly-Si etching characteristics under different photoirradiation methods. The Cl_2 pressure was 10 Torr.²⁰

It was also pointed out that the etching rates, etched features, and etching products (determined by quadrupole mass analyzer) depended strongly on the electron concentration in the conduction band, and the primary effect of the photoirradiation was attributed to the increasing electron concentration arising from electron-hole pair generation.²⁰ The observed PAE by UV light was attributed to the penetration of the Cl^- ion, formed in the near surface region, into the Si lattice caused by the induced surface field between the Cl^- ions and positivity charged Si, namely a field-assisted mechanism originally proposed by Mott and Cabrera.^{33,34}

Figure 2.2 showed that the etching rates for the as-implanted poly-Si (without annealing) were close to that for undoped poly-Si. The etching rate of annealed n^+ poly-Si decreased rapidly with decreasing donor concentration and increasing sheet resistance, while p^+ poly-Si showed the opposite trend. The etching rate of p^+ poly-Si after annealing was much lower than (only one-tenth) that of undoped poly-Si.²⁰

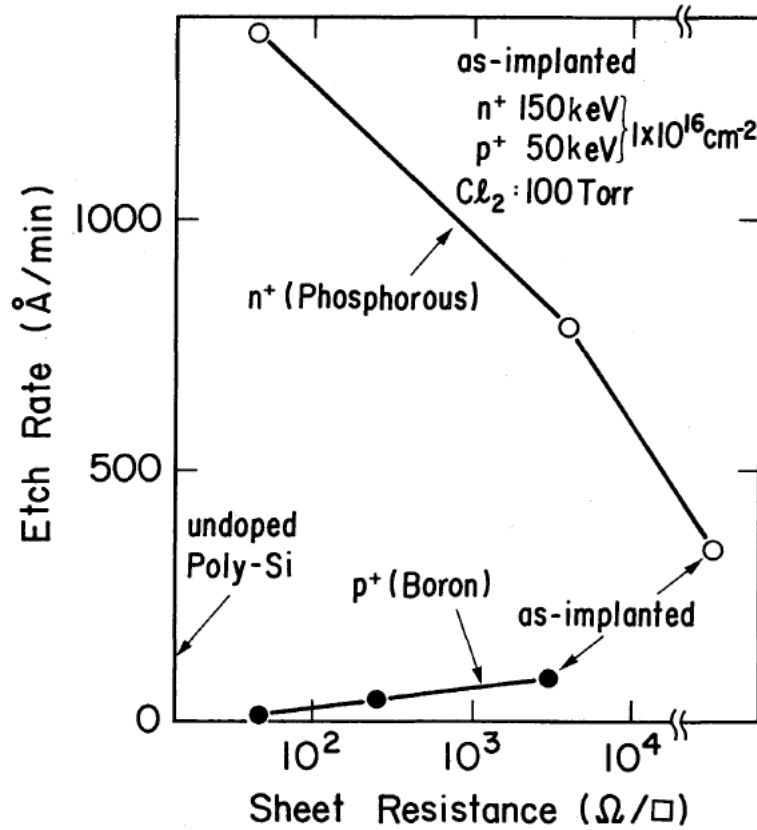


Figure 2.2: Etching rates of n^+ , undoped, and p^+ poly-Si as a function of sheet resistance. The samples were prepared with ion implantation at doses of $1 \times 10^{16} \text{ cm}^{-2}$ (150 keV for phosphorus and 50 keV for boron). The sheet resistance was changed by heat treatment at 550 °C for 40 minutes and 1000 °C for 40 minutes.²⁰

Houle used a low-intensity continuous wave (CW) Ar^+ laser (514.5 nm, up to 6W, unfocussed) and molecular beam mass spectrometry to study the photochemical etching of both n- and p-type Si by XeF_2 .^{21,35} She showed that photo-generated charge carriers enhanced etching by causing desorption of SiF_3 free radical, which was the principal adsorbate on the surface, while SiF_4 formation was largely independent of the light intensity. As showed in Figure 2.3, the increasing reactivity of the fluorosilyl layer led to a net enhancement of the etch rate with the exposure to the light for n-type Si (Figure 2.3 (a)). Two distinct regimes were observed. When laser power was below ~2 W, the etching

rate enhancement was very small. On the other hand, an evident net enhancement of etching rate appeared with a drop in the reflected XeF_2 intensity at laser power above 2 W. The branching ratio between SiF_4 and SiF_3 (Figure 2.3 (b)) showed that the relative amount of SiF_4 steadily declined with an increase of SiF_3 , which accounted for over 60% of the product flux leaving the surface at 6 W.

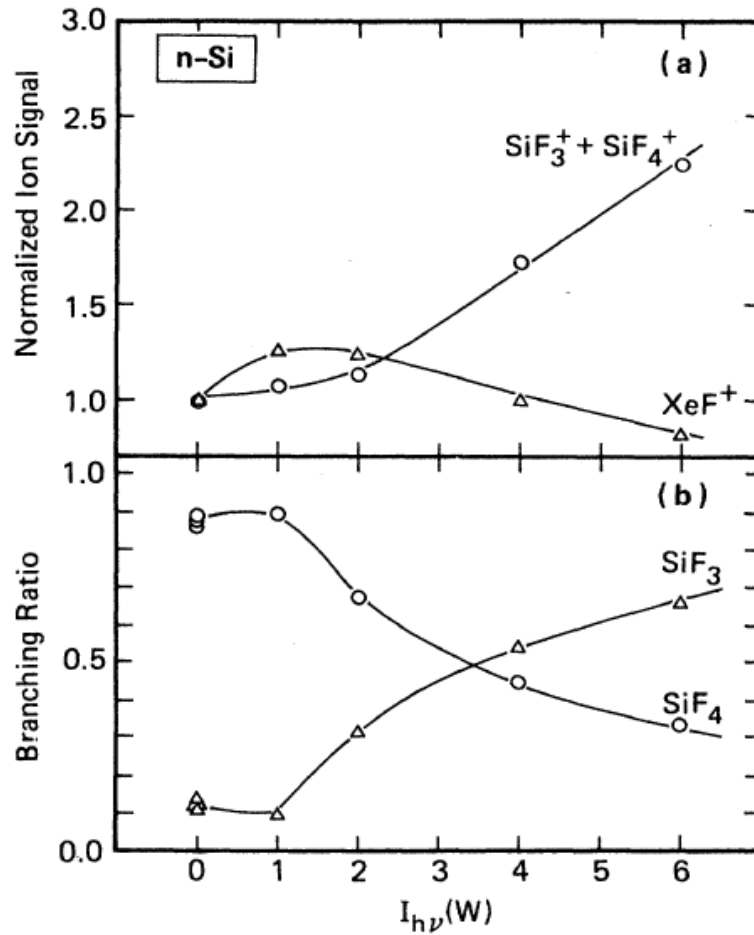


Figure 2.3: Laser power dependence of the product signals during photochemical etching of n-type Si. (a) ion signals for fluorosilyl products and reflected, unreacted XeF_2 normalized to values for spontaneous etching (no laser); (b) branching ratios for the two principal products, SiF_4 and SiF_3 .²¹

The intensity dependences, normalized to the spontaneous etch rate, of SiF_3 and SiF_4 formation for n-type Si showed that the formation of SiF_3 was proportional to $I^{1.60 \pm 0.05}$ and SiF_4 production was independent of light (Figure 2.4), which indicated that SiF_3 was the only photoproduct. The observation of a single photoproduct (SiF_3) and a super linear intensity dependence suggested a mechanism involving two photo-generated charge carriers in the rate-limiting photostimulated desorption step was responsible for the observed photo-enhance etching.^{21,35}

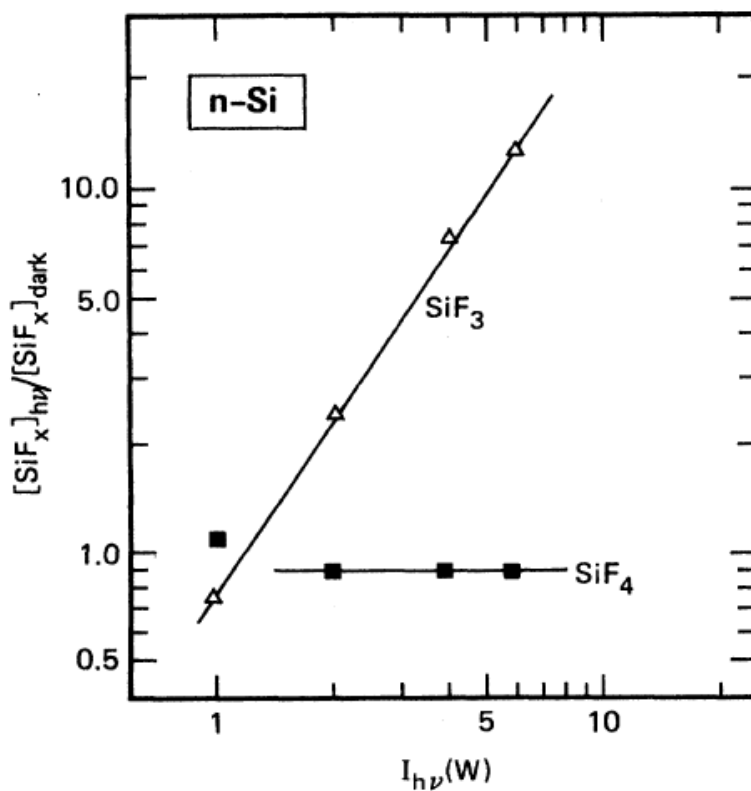


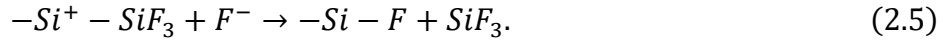
Figure 2.4: Intensity dependence of SiF_3 and SiF_4 formation on n-type Si.²¹

The proposed mechanism included the following sequence of steps:





and



This mechanism accounted for the higher order dependence on light intensity, sufficient energy released to break Si-Si bond, and high selectivity for SiF₃ desorption from the surface of the fluorosilyl layer.^{21,35} Additionally, similar trend and mechanism was also found for p-type Si (data not included).

Similar to Houle's study, Kirimura *et al.* reported the photon-stimulated desorption of chlorinated p-type Si (111) with picosecond-pulsed (2 ps) laser irradiation at the wavelength of 400 nm (3.1 eV) in 2006.³⁶ Desorption of SiCl and SiCl₂ molecules were observed with a quadrupole mass spectrometer and a pulse-counting system. The reason of using the irradiation of femtosecond and picosecond pulse lasers was to study the halogen etching excluding thermal effects. The superlinear dependence of the desorption rates on laser fluence suggested that multiple excitation by substrate hot carriers was critical to the etching.

Bäuerle *et al.* investigated the laser-induced chemical etching of Si in Cl₂ atmosphere under either pulsed (308 nm XeCl excimer laser, 423 nm and 583 nm excimer laser pumped dye laser) or CW irradiation (457.9 nm, 488.0 nm, 514.5 nm Ar⁺ and 351 nm, 647.1 nm Kr⁺ laser) at various wavelengths.^{37,38} Figure 2.5 showed that the etching

rate for 308 nm XeCl excimer laser radiation at perpendicular incidence onto the Si substrate as a function of energy density for three different Cl_2 pressures. Three characteristic regimes were observed. I) For low laser fluence ($\leq 100 \text{ mJ/cm}^2$), etching rate increased linearly with energy density. II) At medium energy densities (between ~ 150 and 440 mJ/cm^2), the etching rate increased nonlinearly with laser fluence. III) Above $\sim 440 \text{ mJ/cm}^2$, the etching rate saturated and less dependent on Cl_2 pressure. It was suggested that with low laser fluence causing only negligible surface heating, etching was non-thermal and based on direct interactions between photo-generated carriers and Cl radicals (regime I). For fluence which induced surface melting, etching was mainly thermally activated (regime III). Both mechanisms were important in the intermediate regime (regime II).³⁷

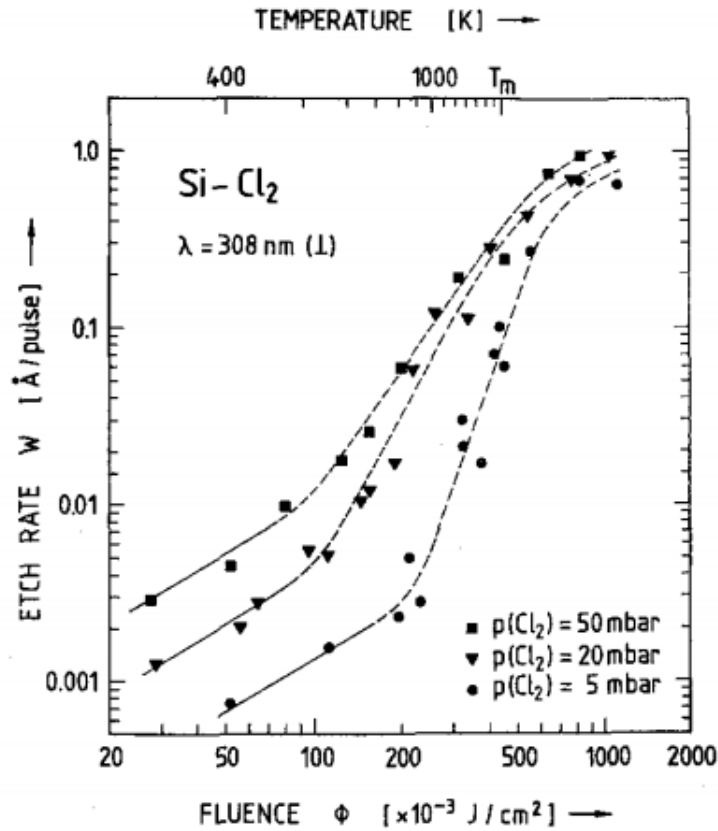


Figure 2.5: Etching rate of Si as a function of 308 nm XeCl-excimer-laser fluence for various Cl_2 pressures. The temperatures indicated on the upper scale were calculated.³⁷

Sesselmann *et al.* studied laser induced chemical etching of Si (100) in Cl₂ by using pulsed excimer lasers at 308 nm and 248 nm. The dependence of the etching rate on laser energy fluence was also classified into three regimes, which was similar to the study of Bäuerle *et al.*²² In the regime at low laser fluence that non-thermal photo desorption dominated, significant differences of the etching rate dependence on laser fluence (Figure 2.6), Cl₂ gas pressure, and Cl₂ gas flow were observed between 308 and 248 nm radiation. This wavelength dependence was attributed to two different excitation mechanisms of the Cl₂ gas and the Si solid at these two laser wavelengths.²²

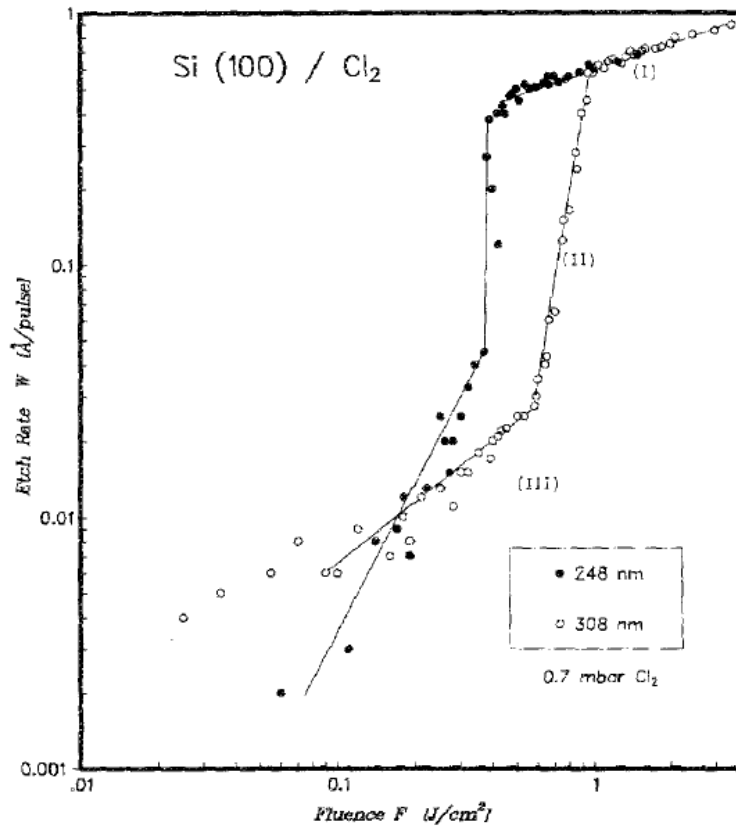


Figure 2.6: Etch rate as a function of laser energy fluence for a Si (100) surface exposed to 0.7 mbar Cl₂ at a gas flow rate of 20 sccm. Excimer laser radiation of 248 and 308 nm was used at 20 pulses per second (pps) pulse repetition rate. The etch rate curves consisted of three energy fluence ranges (I), (II), and (III) characterized by the straight lines.²²

It was pointed out that the non-thermal laser induced chemical etching consisted of two steps: surface reaction and photoinduced desorption of the reaction products. Compared with 248 nm radiation, 308 nm radiation could be absorbed much more strongly by gaseous Cl_2 leading to photodissociation and generation of Cl radicals close to the Si surface. The Cl atoms generated by the gas phase photodissociation could locally enhance the surface chlorination and the etching rate.²²

Jackman *et al.* studied the interaction of chlorine with p-type Si (100) utilizing quadrupole mass spectrometer both in the absence and presence of UV radiation from a 100 W low pressure mercury lamp. Two desorption states denoted α and β were found with thermal desorption peak temperatures of 450 and 900 K, and corresponding desorption activation energies of 115 and 235 kJ/mol. The α state exclusively resulted in the evolution of SiCl_4 , while both SiCl_4 and SiCl_2 were evolved from the β state.³⁹ Figure 2.7 showed that UV irradiation of Si in Cl_2 caused a surface interconversion of strongly adsorbed forms into more weakly bound species and enhanced population of the α state relative to β state, leading to considerably enhanced desorption rate and overall etching rate.³⁹

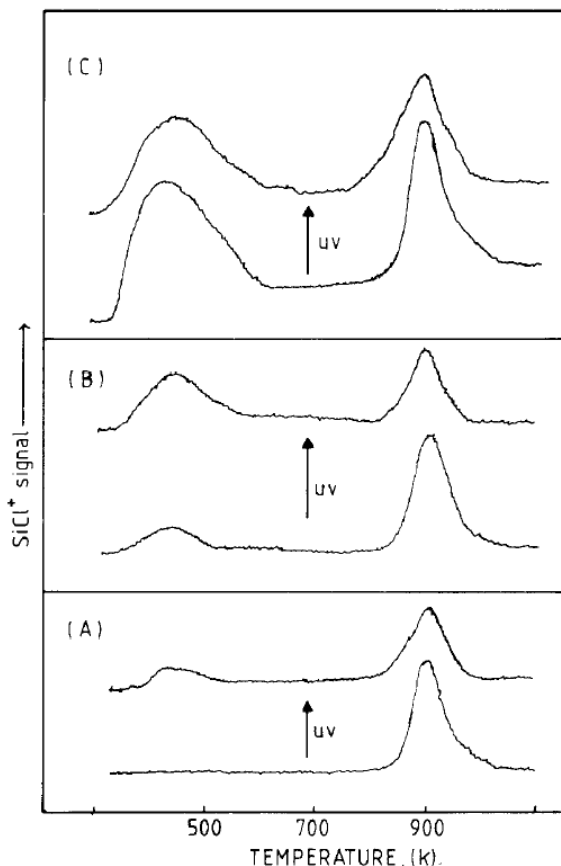


Figure 2.7: Thermal desorption spectra monitored prior and subsequent to exposure to UV radiation for increasing (A)-(C) chlorine coverage.³⁹

In 2007, Samukawa *et al.* quantitatively investigated the dependence of the etching rate with irradiation of photons with a UV lamp (short-arc Xe flash lamp, pulse discharge) and high-density Cl atom beam to understand the influence of UV photon irradiation in the plasma etching process. It was shown that 220-380 nm radiation drastically enhanced the etching rate of Si in a Cl atom beam (shown in Figure 2.8) at UV lamp power densities $> 20 \text{ mW/cm}^2$ (shown in Figure 2.9). They speculated that the increased surface chemical reactions and etching rate were caused by the crystal defects on the Si surface, created by the UV light, which were more susceptible to reaction with etchants.²³

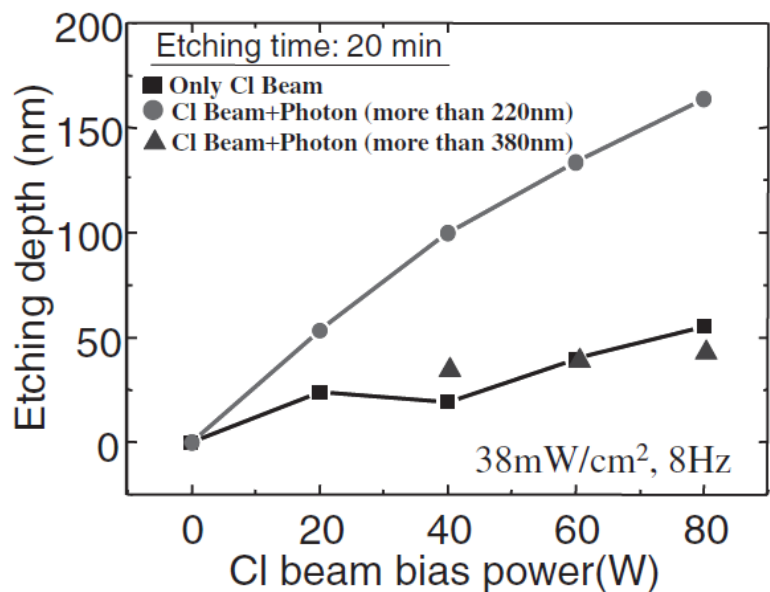


Figure 2.8: Effects of photon irradiation (power: 38 mW/cm², frequency: 8 Hz) on etching depth as a function of RF bias power during Cl neutral beam etching. The Si etching depth was measured using AFM. The irradiated photon wavelength was controlled by UV photon filter.²³

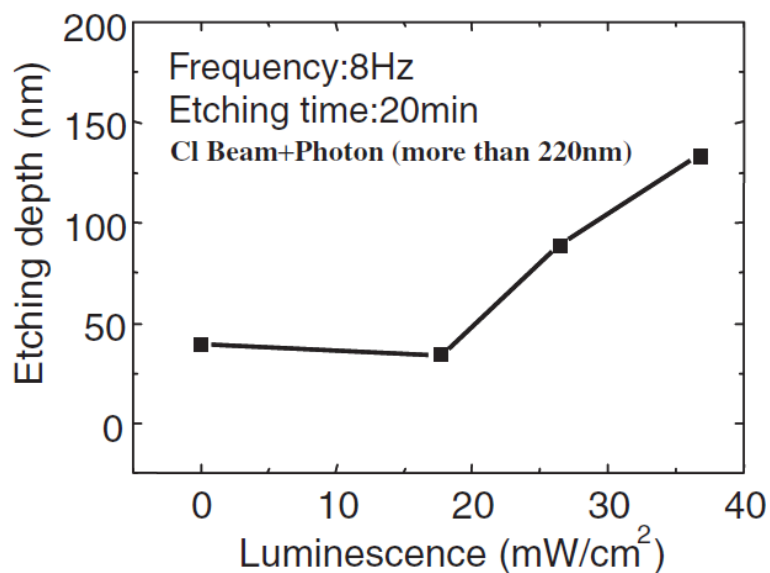


Figure 2.9: Dependence of etching depth on photon irradiation power at the same neutral beam energy and flux.²³

Schwentner *et al.* investigated photo-induced etching of n-type Si (100) with XeF₂ using synchrotron radiation in the VUV range (50 to 200 nm). Replicas of a mask (Ni mesh, width of wires: 10 μm) were etched into Si wafers with filtered radiation (LiF: $\lambda \geq 105$ nm, CaF₂: $\lambda \geq 122$ nm, quartz: $\lambda \geq 150$ nm). They found that photo-induced etching was strongly wavelength-dependent, with the maximum yield exhibited in the range from 112 nm to 120 nm (Figure 2.10). The overall quantum efficiency of etching was above unity for wavelengths shorter than ~ 120 nm, which exceeded that in the visible spectral range by more than four orders of magnitude. Below 120 nm, a further increase of the quantum efficiency was observed (up to 100) for Si. They attributed such high-yields to the photo-excitation of a thin reactive surface layer on top of the Si wafer followed by an effective chain reaction with an amplification of the order 10^5 .⁴⁰⁻⁴⁴

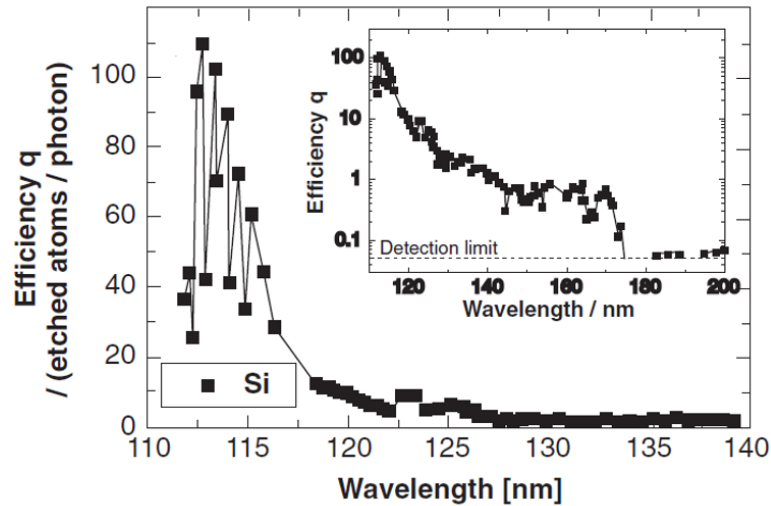


Figure 2.10: Selective etching efficiency of Si/XeF₂ on both linear scale and logarithmic scale.⁴¹

2.2 In-plasma PAE

2.2.1 Discovery of in-plasma PAE

In 2012, Shin *et al.* first reported in-plasma PAE of p-type Si in chlorine-containing plasma.¹⁷ This phenomenon was discovered in Ar plasmas with a few percent of Cl₂ added. A nearly monoenergetic IED was obtained by applying a synchronous DC bias during the afterglow of a pulsed, inductively coupled, Faraday-shielded plasma (Figure 2.11). The broad lower energy peaks originated from the active glow, and it could be controlled by the gas pressure to ensure ion energy was below the IAE threshold. The sharp higher energy peaks (FWHM < 2eV) were due to the extremely low electron temperature in the afterglow, and its energy could be controlled by varying the DC bias voltage on the boundary electrode or the sample.

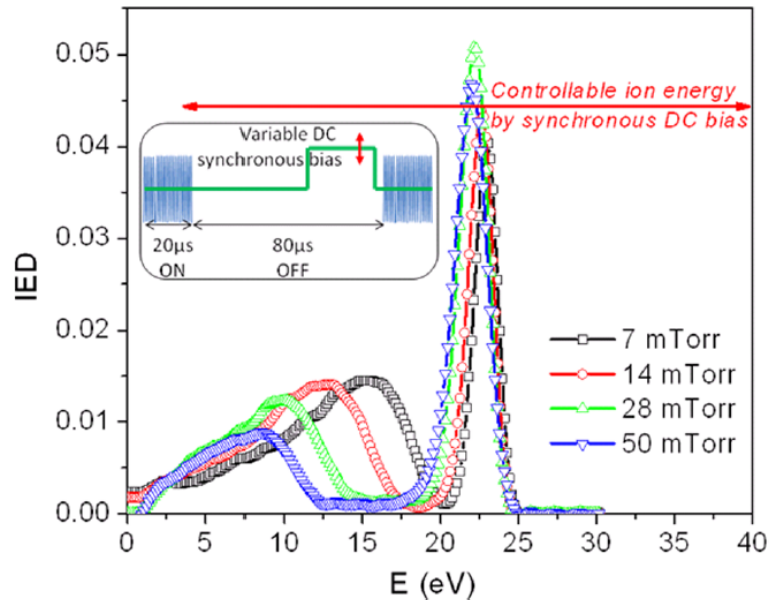


Figure 2.11: IEDs generated by applying a synchronous DC bias on a boundary electrode for a specified time window during the afterglow of a pulsed Ar plasma.¹⁷

It was found that Si etching rates increased with the square root of the ion energy above the observed threshold of 16 eV. On the other hand, a substantial etching rate independent of ion energy was observed, when the ion energy was below the IAE threshold (Figure 2.12). After ruling out the possibilities of chemical etching by Cl atoms, etching assisted by Ar metastables, etching mediated by holes and/or low energy electrons generated by Auger neutralization of low-energy ions, Shin *et al.* finally concluded that PAE was the only likely explanation. Specifically, the VUV photons generated in the plasma played a major role in the subthreshold etching of silicon.

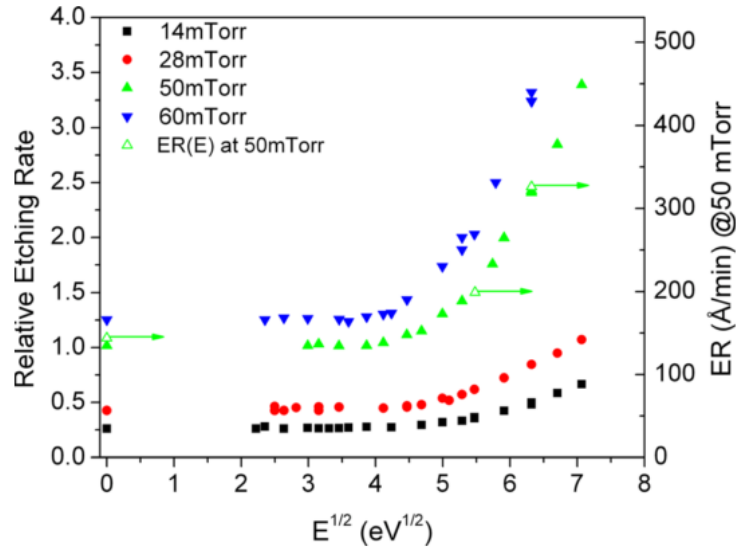


Figure 2.12: Relative Si etching rates (intensity of Si 2882 Å emission) at different pressures, and absolute etching rate at 50 mTorr (hollow triangles) as a function of $E^{1/2}$ in 1%Cl₂/99% Ar plasma pulsed at 10 kHz with a duty cycle of 20%. The bias was applied 50 μs into the afterglow (from 70 μs to 98 μs).¹⁷

More recently, Zhu *et al.* measured the relative PAE rates of Si in different halogen containing plasmas by varying the ion bombardment energy (Figure 2.13).¹⁸ The ‘true’ PAE etching rates, shown as double headed arrows in Figure 2.13, were obtained by

subtracting the isotropic chemical etching component from the total sub-threshold etching. PAE rates were found to be lowest in 50%Br₂/50%Ar plasma. On the other hand, the highest PAE rates were observed in 25%HBr/25%Cl₂/50%Ar plasma. The measured PAE rates matched quite well with the product of the observed Ar emission intensity (750.4 nm) and the total halogen surface coverage measured by XPS (Figure 2.14).

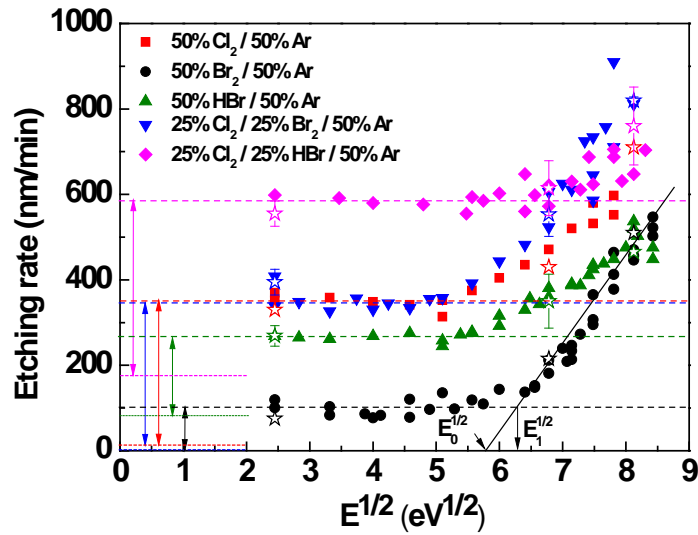


Figure 2.13: Si etching rates as a function of the square root of ion energy with pulsed DC bias at 10 kHz and 50% duty cycle on the sample stage. Absolute etching rates of blanket p-type Si were obtained by calibration of the relative intensity of Si 2882 Å emission with the measured absolute etching rates (hollow stars).¹⁸

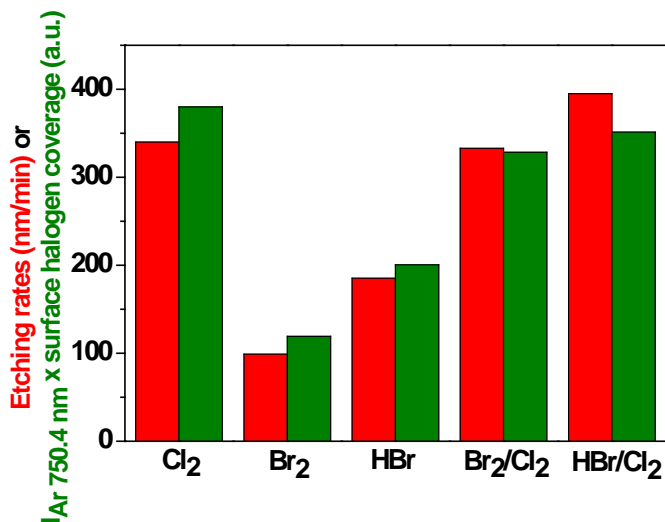


Figure 2.14: PAE rates of blanket p-type Si measured by stylus profilometer in different halogen plasmas (red) and the product of the total surface halogen coverage (Cl + Br) and Ar emission (750.4 nm) intensity (green).¹⁸

In 2016, Sridhar *et al.* investigated the potential mechanisms of PAE.¹⁹ Multiple research groups have studied the role of UV/VUV photons in Si etching in the absence of plasma (more details in section 2.1). PAE of silicon in a halogen environment has been studied extensively using UV lasers/lamps as the light source. Most of these studies attributed PAE to the creation of electron-hole pairs and reactions of these carriers at the near surface region.^{20,21} Other researchers proposed that UV irradiation could induce crystal defects to promote Si etching in the damaged layer.²³ These two mechanisms should behave differently in that carrier-mediated etching should cease rapidly after the plasma is extinguished due to the rapid decay of the photo-generated carriers, while etching caused by defects should continue until the damaged layer etches away completely even after the plasma is extinguished. This can be verified by modulating the plasma power between two different values at a rate that is much faster than that required to remove a monolayer.

As shown in Figure 2.15, I_{Cl}/I_{Ar} exhibited small spikes when power changed, and then settled to nearly equal values that suggested only a slight decrease in Cl atom number density at low vs. high power. On the other hand, when power dropped from 500 W to 300 W, I_{Si}/I_{Ar} spiked but finally settled to a quasi-steady value that was $\sim 25\%$ of that at 500W. I_{SiCl}/I_{Ar} exhibited similar but less pronounced trends, settling to a value at the end of the 300W period that was about 60% of that at 500 W. The modulation in I_{Si}/I_{Ar} and I_{SiCl}/I_{Ar} suggested that the Si etching rate was also modulated.

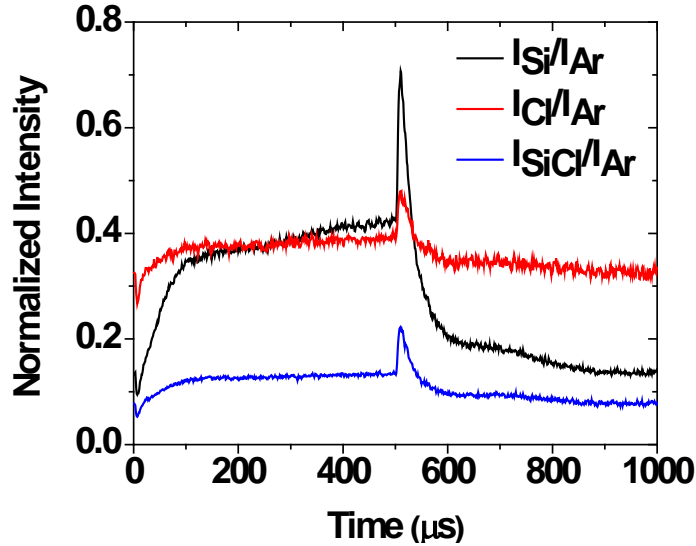


Figure 2.15: Time resolved normalized emission intensities recorded during Si etching in a 50%Cl₂/50%Ar plasma where power was modulated between 500 and 300 W at a frequency of 1 kHz and 50% duty cycle.¹⁹

After verifying the contribution to the signal due to back diffusion of the etching products was minimal, the authors concluded that the modulation of the signal was mainly due to the modulation of the PAE rate with power. The observation of a substantially modulated I_{Si}/I_{Ar} signal ruled out the damage-induced mechanism of in-plasma PAE.

2.2.2 Wavelength dependence of PAE

The wavelength dependence of PAE was investigated by measuring the etching rates of Si placed under windows with different light transmission characteristics.¹⁸ For example, a magnesium fluoride (MgF_2) window transmits 50% at 125 nm and transmission rapidly falls to 0% at 110 nm. UV grade fused silica windows do not transmit wavelengths < 170 nm. All these window materials are opaque to the Ar VUV emissions at 104.8 nm and 106.6 nm, which are likely the major contributors to the total VUV radiation and etching rate of silicon.

PAE rates were obtained by measuring the etching depth of masked samples using a stylus profilometer after etching (Figure 2.16). These etching rates were compared with those measured without any window (all wavelengths). The presence of the window above the Si substrate also lowered the plasma density in the region between the Si substrate and the window. Based on the transmission characteristics of the windows used, etching rates (ER) were ordered as follows: $\text{ER}_{\text{windowless}} \gg \text{ER}_{\text{MgF}_2} > \text{ER}_{\text{quartz}} \sim \text{ER}_{\text{opaque}}$. The etching rate was not zero beneath the opaque window because light scattered off the bottom of the window, and also because low intensity plasma was generated between the sample and the window. It may also be noted that the etching rates under the opaque and quartz windows were about 20 times lower than that without any window, suggesting that photons with wavelength > 170 nm were not effective in inducing etching. The etching rate under the MgF_2 window was ~ 10 times lower than the etching rate without any window. Although quantitative estimation of the reduction in VUV transmission by MgF_2 window was

complicated, it appeared that VUV radiation played a critical role in etching, specifically at lower wavelength.¹⁸

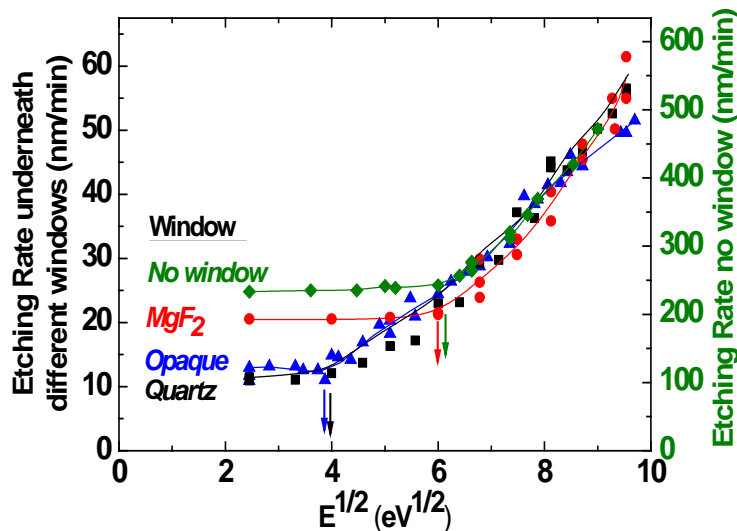


Figure 2.16: Absolute etching rates (calibrated based on the Si emission) under different window materials as a function of $E^{1/2}$ in 50% Cl_2 /50% Ar plasmas.¹⁸

2.2.3 Surface morphology of PAE

AFM was used to examine the surface morphology of Si etched in different plasmas. The RMS roughness (R) for substrates etched in different plasmas followed the order: $R(50\% \text{Br}_2/50\% \text{Ar}) > R(50\% \text{HBr}/50\% \text{Ar}) > R(25\% \text{HBr}/25\% \text{Cl}_2/50\% \text{Ar}) > R(50\% \text{Cl}_2/50\% \text{Ar})$. Silicon wafers etched in 50% Cl_2 /50% Ar plasma without applied bias were found to be relatively smooth, except for a few pyramid-shaped hillocks on the surface (Figure 2.17). The formation of these well-defined pyramidal structures suggested that PAE had a dependence on the orientation of crystallographic planes. Analysis of the AFM images showed that the base of the pyramidal features was oriented at 45° to the

(110) cleavage planes and hence lied on the $\langle 100 \rangle$ direction, and (100) planes etched faster compared to the (110) planes leading to micro-masked features with (110) facets. This could be due to steric hindrance on a closely packed Si surface that reduced the number of favorable adsorption sites and penetration of the relatively large Cl atoms into the Si lattice, leading to faster etching of Si (100), relative to Si (110).⁴⁵

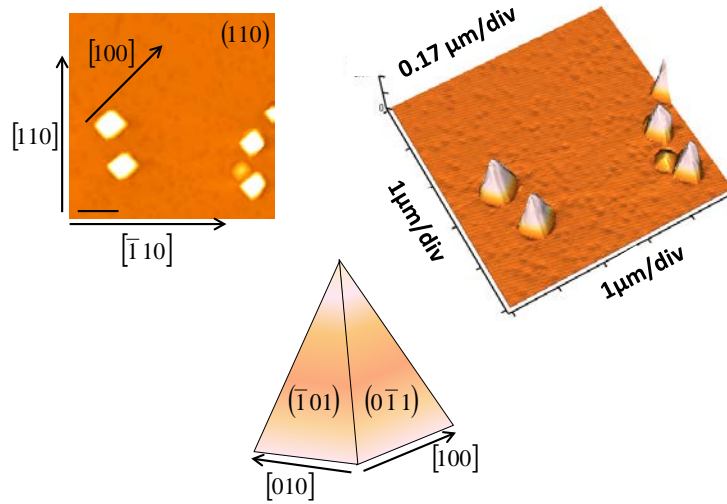


Figure 2.17: (a) 25 μm^2 AFM image of p-Si etched in 50%Cl₂/50%Ar plasma at 0V bias for 2 minutes. (b) 3D view showing the pyramidal features. (c) (110) planes that formed the faces of the pyramidal feature.¹⁸

PAE was also found to have unwanted effects on etching profiles. When PAE dominated, nanotrenches were observed at the bottoms of the sidewalls of the etched features (Figure 2.18), which could be caused by the concentrated electric field at the bottom corners.¹⁷

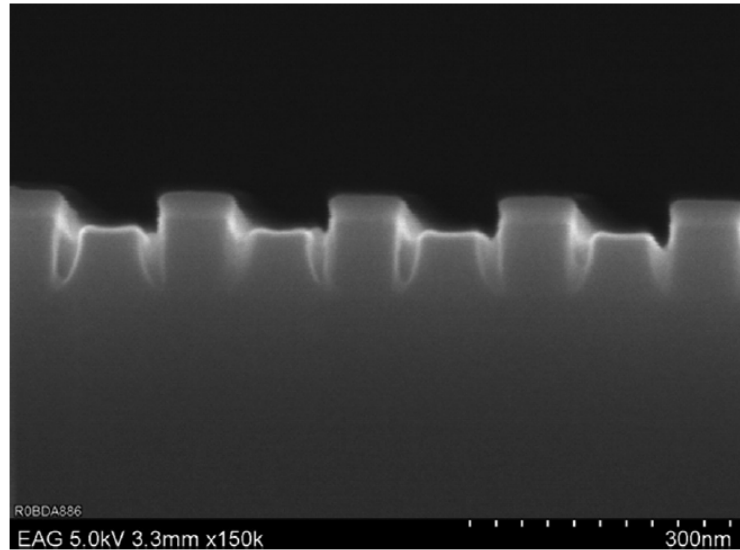


Figure 2.18: Cross sectional scanning electron microscope (SEM) image of a patterned (100 nm lines and 100 nm spaces with 30 nm oxide mask on top) p-type Si sample after 10 min. etching in 1%Cl₂/99%Ar pulsed plasma at 50 mTorr under PAE condition.¹⁷

2.2.4 Pros and cons of in-plasma PAE

Depending on the application, PAE can be advantageous or an unwanted complication for microelectronics fabrication. For example, PAE was used to perform extremely selective etching of nanoholes in silicon using an ultrathin native oxide as a mask to transfer a nanopantography-defined pattern deep into the Si substrate with minimal or no mask undercut.^{31,32} On the other hand, PAE can be detrimental for processes that require monolayer accuracy, where very low ion energies are necessary to promote selectivity. If spontaneous or PAE occurs, the process is not self-limiting, thereby compromising atomic layer resolution.¹²

2.3 IAE yield and threshold

Chang and Sawin studied the surface kinetics of ion-enhanced chlorine plasma etching by utilizing a collimated Ar^+ beam for ion bombardment and a high flux Cl and Cl_2 beam as reactants.⁴⁶ In their work, the Ar^+ and atomic or molecular chlorine fluxes were controlled independently over a wide range and at the flux level typically used in high density plasma processing. Ion flux (as high as 2 mA/cm^2 , $6.2 \times 10^{14} - 1.2 \times 10^{16} \text{ cm}^{-2}\text{s}^{-1}$) was generated with a modified ASTeX compact electron-cyclotron-resonance plasma source. An atomic chlorine beam ($\sim 90\%$ dissociation of Cl_2) was obtained with a high density plasma generated by a tuned coaxial microwave cavity source with the flux of $1.4 \times 10^{16} - 2.8 \times 10^{17} \text{ cm}^{-2}\text{s}^{-1}$. *In-situ* interferometric measurement with a He-Ne polarized laser was used to obtain the undoped polysilicon thin film etching rates.

They found that the etching yield was independent of the individual beam flux, but it had a strong correlation with the atom-to-ion flux ratio. The etching yield first increased sharply with the increase of neutral-to-ion flux ratio at low flux ratios, when the reaction was limited by the availability of chlorination on the surface. Then it gradually saturated at higher flux ratios as the ion flux limited the etching yield, when the surface was highly chlorinated (Figure 2.19). The transition between the neutral-flux-limited and ion-flux-limited regimes was a function of ion energy. In addition, the ion energy dependence was found to scale linearly with $(E_{\text{ion}}^{1/2} - E_{\text{th}}^{1/2})$, where the threshold energy E_{th} was found to be 16 eV (Figure 2.20).

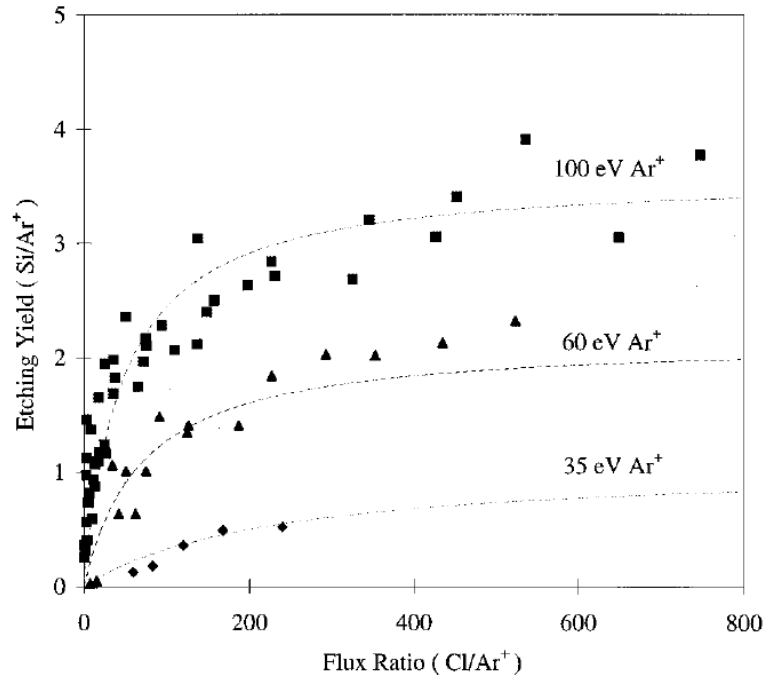


Figure 2.19: Ion-enhanced polysilicon etching yield vs. Cl atom to Ar⁺ ion flux ratio. An initial sharp rise in the etching yield was observed at low flux ratios where reaction was limited by the supply of reactive neutrals. The etching yield then gradually saturated as the reaction became ion-flux limited at higher flux ratios. Dotted lines were fits of a surface kinetic model.⁴⁶

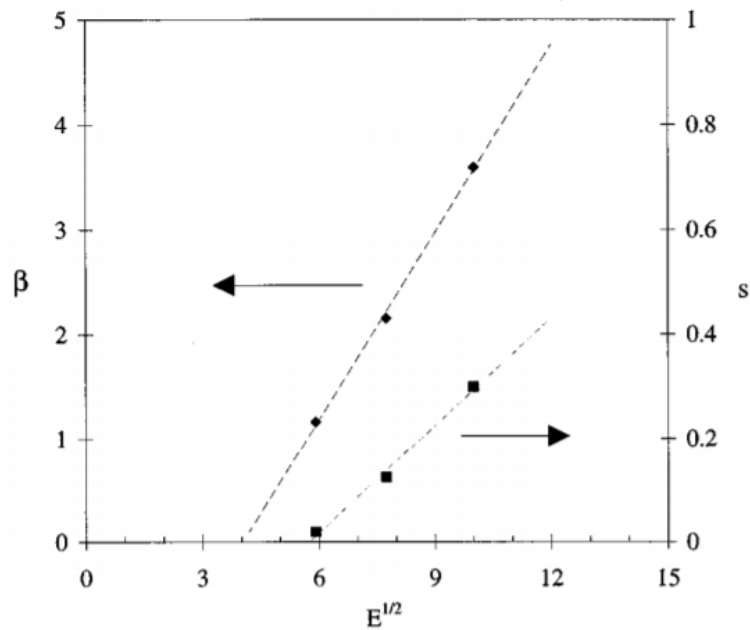


Figure 2.20: Model fitted parameters of etching yield (β) and Cl sticking coefficient (s) as a function of square root of ion energy for Ar⁺/Cl etching of polysilicon. The extrapolated threshold energy was 16 eV.⁴⁶

Chang and Sawin subsequently reported that the IAE threshold energy was ~ 10 eV for Cl^+ ion ($6.2 \times 10^{14} - 1.2 \times 10^{16} \text{ cm}^{-2} \text{ s}^{-1}$) and Cl/Cl_2 (90% dissociation, $1.4 \times 10^{16} - 2.8 \times 10^{17} \text{ cm}^{-2} \text{ s}^{-1}$) neutral beams (Figure 2.21). The etching yield showed similar dependence on Cl/Cl^+ flux ratio with a much higher yield (at least a factor of 2) compared with Cl/Ar^+ system due to the greater chemical reactivity of Cl^+ (Figure 2.22).⁴⁷

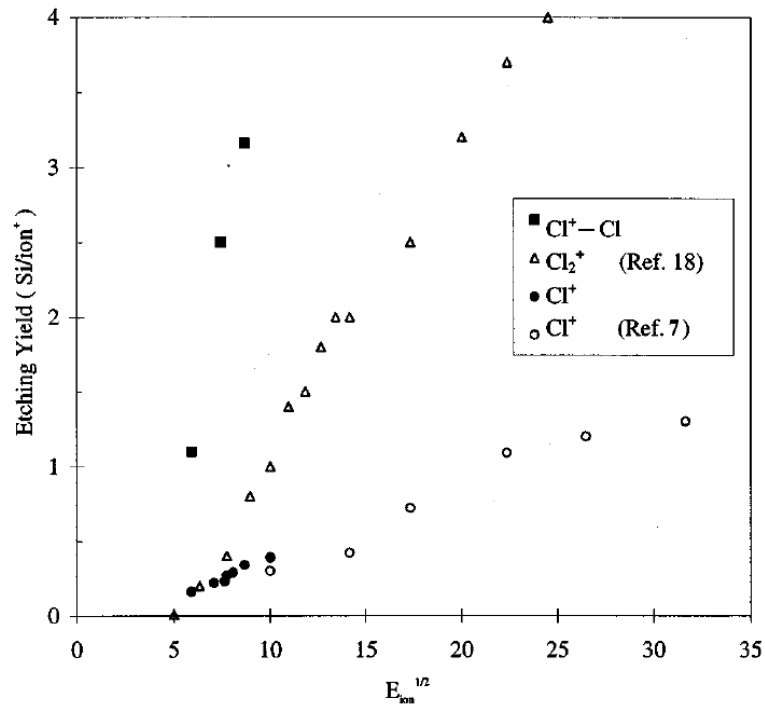


Figure 2.21: Etching yield of polysilicon by Cl^+-Cl , Cl_2^+ , and Cl^+ as a function of the square root of ion energy. The etching yields of polysilicon by utilizing Cl^+ and Cl beams were taken in the saturation regime with flux ratio ≥ 300 .⁴⁷

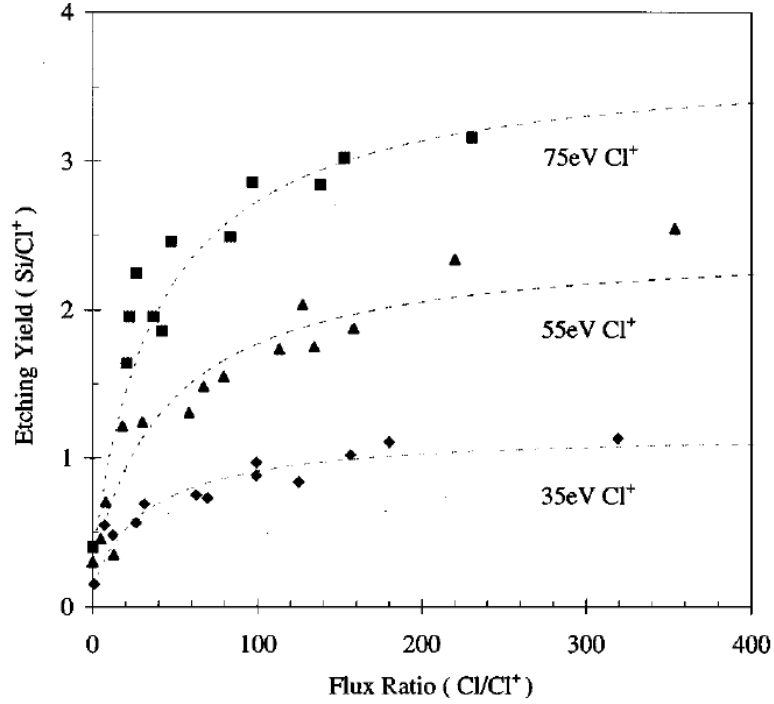


Figure 2.22: Ion-enhanced polysilicon etching yield vs. Cl atom to Ar⁺ ion flux ratio at three different ion energy levels.⁴⁷

Balooch and Hamza reported the IAE yield of polycrystalline Si measured with Cl₂⁺ or Ar⁺ beams (intensity up to 30 μA/cm²) of energy 40-900 eV in the presence of molecular chlorine.⁴⁸ The *in-situ* Si etching rates were determined by a quartz crystal microbalance. With sufficient chlorine flux to saturate the surface, the yield measured with Cl₂⁺ exhibited a linear relationship with the square root of ion energy, and it was higher than that measured with Ar⁺ at the same ion energy by a factor of 20% (Figure 2.23). The IAE threshold was found to be higher with molecular chlorine (45 eV for Ar⁺/Cl₂ and 25 eV for Cl₂⁺/Cl₂, Figure 2.23), compared to that found by Chang and Sawin, using atomic chlorine. The reported etching yield was much lower (4-5 times) than that of Chang and Sawin, which can be attributed to the larger saturation coverage of atomic chlorine compared with molecular chlorine.

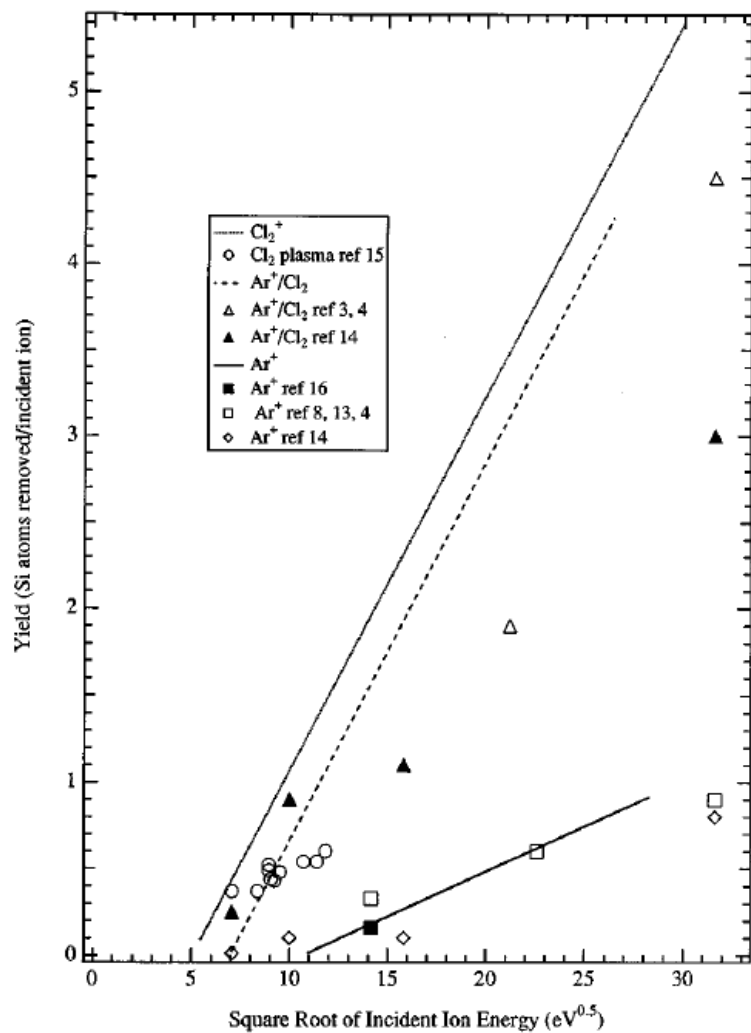


Figure 2.23: Etching yield as a function of the square root of incident ion energy.⁴⁸

Chapter 3 – Apparatus and Methods

3.1 Experimental setup

The overall experimental setup is shown in Figure 3.1. A sample was first introduced into the load-lock chamber at atmospheric pressure, then transferred in vacuum to the plasma chamber, where it was etched. After etching, the sample could be subsequently transferred in vacuum, through the transfer chamber into an XPS chamber for surface analysis. In addition to XPS analysis, Scanning Electron Microscope (SEM) was also used to determine the etching profile. Laser interferometry and spectroscopic ellipsometry were employed to measure etching rates. A detailed description of the experimental apparatus and methods used in this study is given below.

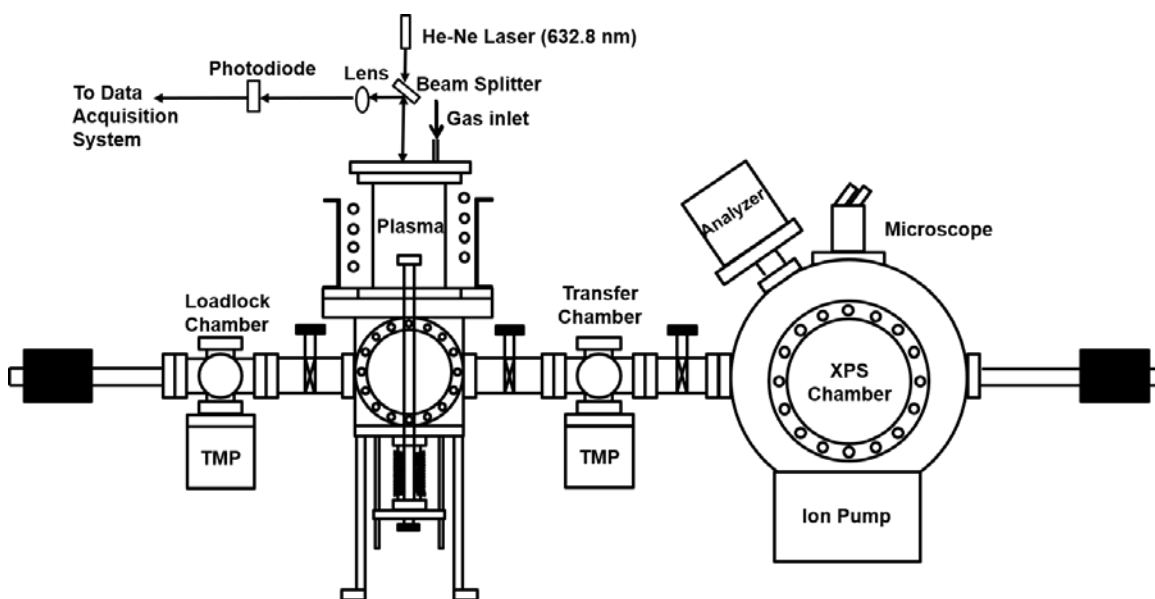


Figure 3.1: Experimental apparatus.

3.1.1 Inductively coupled plasma (ICP) source

High density ICP etching tools meet the needs for large area and high etching rate required in the manufacturing of integrated circuits. For an ICP source, radio frequency (RF) voltage applied on the coil induces an axial RF magnetic field, which in turn induces an azimuthal RF electric field inside the reactor. Electrons inside the reactor are accelerated by the electric field and some of them gain enough energy to drive ionization of the gas atoms or molecules resulting in the production of a plasma.

High plasma densities (10^{12} cm^{-3}) can be achieved in an ICP at low pressures (1-10 mTorr) enabling higher etching rates and faster processing. In addition, the use of a separate power source, either DC or RF, on the substrate stage, allows the quasi-independent control of ion energy and plasma density.^{4,49}

In this study, the Faraday-shielded ICP source was powered by an air cooled 4-turn copper coil, wound around the alumina reactor (13 inches long and 3.125 inches inside diameter). Figure 3.2 shows details of the plasma etching reactor. The discharge tube was connected to a 6-inch cubical stainless steel (SS) chamber through an adaptor flange, in which water flowed through channels in order to cool the Faraday shield and discharge tube during experiments.

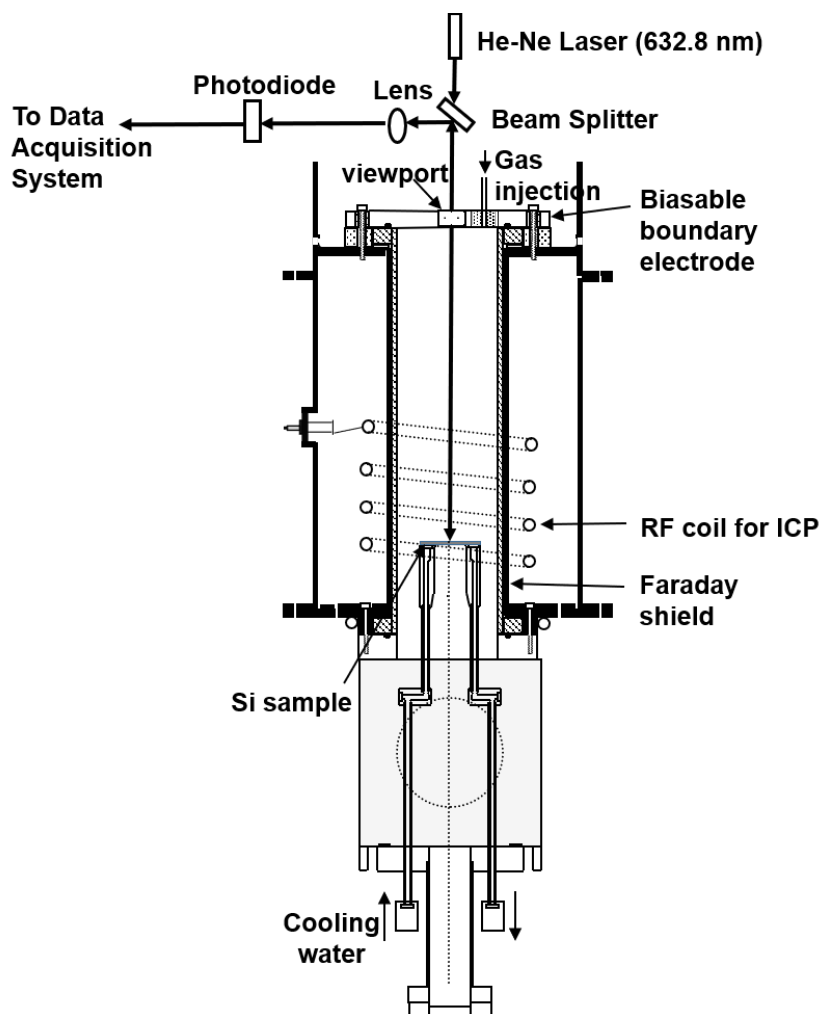


Figure 3.2: Schematic of the plasma source. The Faraday-shielded ICP reactor was equipped with a He-Ne laser interferometry setup for real time etching rate measurements.

RF power at 13.56 MHz was delivered to the plasma by a RF amplifier (Electronic Navigation Industries Model A-500) that was driven by a function generator (Keysight 33600A). The Π matching network was manually tuned to match the impedance of the plasma in series (load impedance) to the $50\ \Omega$ output impedance (source impedance) of the RF power supply to maximize power transfer efficiency. A constant nominal net power of 350W (with a reflected power of ~ 4 W) was delivered to the system and measured with in-

line Bird (model 43) wattmeters (net power = forward power – reflected power). The actual power dissipated in the plasma should be somewhat lower than the nominal power due to power losses in the matching network and the coil. The RF tap point was at $\sim 3/4$ turn of the coil from the grounded end. The plasma was ignited with a Tesla coil in proximity to the boundary electrode. Figure 3.3 shows the circuit of the Π -matching network used in this study.

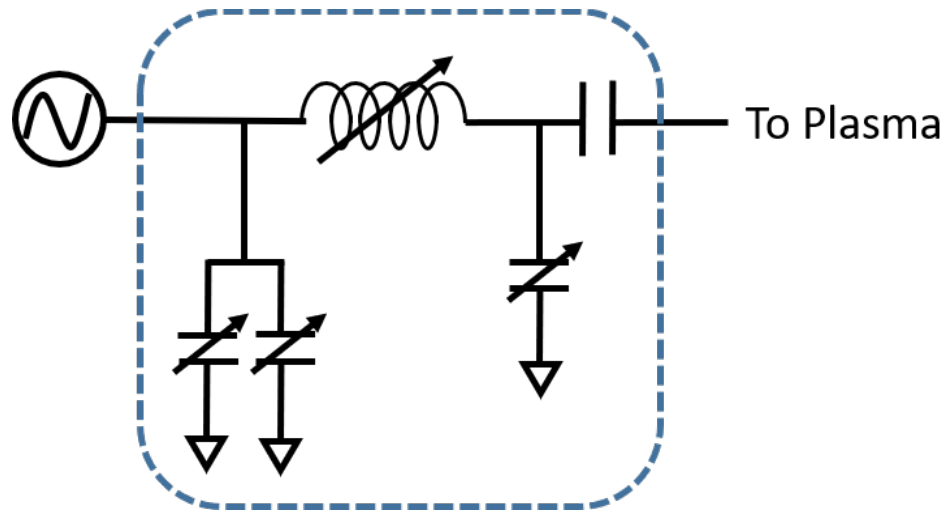


Figure 3.3: Schematic of the Π -matching network circuit used in this work. The variable capacitors and the inductor could be tuned to minimize the reflected power.

An electrically grounded Faraday shield, installed between the coil and the alumina tube, prevented capacitive coupling between the high voltage end of the coil and the plasma, as verified by a very small measured peak-to-peak voltage of ~ 1.5 V (shown in Figure 3.4) on an electrically floating stage immersed in the plasma, indicating a negligible RF component of the plasma potential.

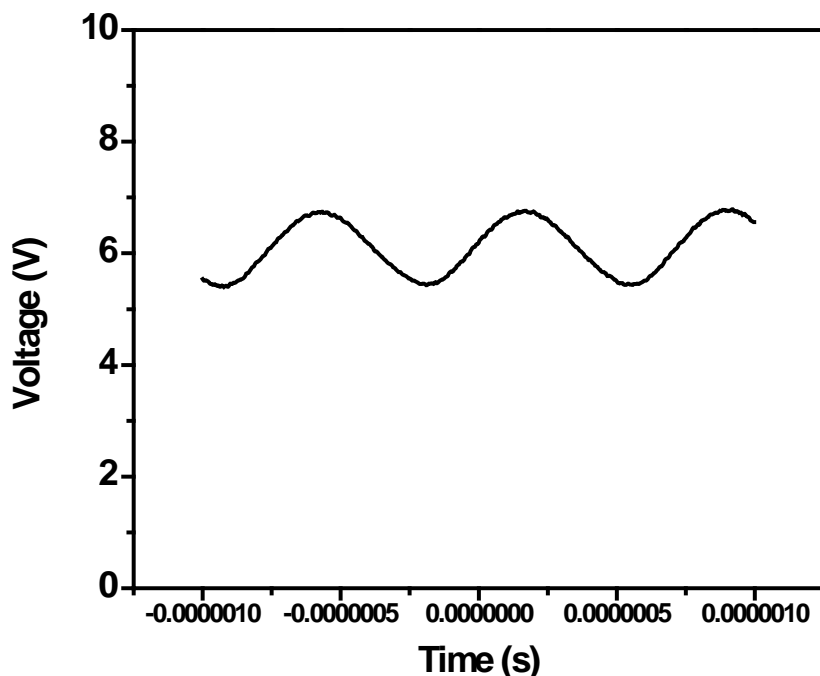


Figure 3.4: Voltage waveform measured on the floating SS sample stage at pressure 60 mTorr while plasma was on.

The chamber was evacuated by a turbomolecular pump (Ebara ET300WS) with pumping speed of 300 l/s backed by an oil pump (Leybold Model D40BCS). The base pressure in the plasma reactor was $\sim 4 \times 10^{-7}$ Torr measured by an ion gauge. A Cl_2/Ar (molar ratio 1:9) gas mixture was fed through a nozzle on the electrically grounded top flange. A total flow of 50 sccm (henceforth called “low flow rate”) or 250 sccm (henceforth called “high flow rate”) was used and controlled by mass flow controllers (SEC-7330 and Tylan 2979M). The operating pressure, at the downstream of the ICP source and above the pumping port, was monitored with an MKS 629 capacitance manometer (0.1 Torr full scale). Pressure above the sample (corrected for the pressure drop between the sample location and the point where the pressure measurement was made) was maintained at 60 mTorr during etching using a throttle valve. At this pressure, with no bias applied to the

sample, it is expected that very few ions will have energy above the IAE threshold of silicon.

A calibration experiment, without plasma, showed that the pressure at the discharge region was about 30-40% higher than that measured at the position of the capacitance manometer. Figure 3.5 shows the pressure calibration curve. Pressures reported below are those in the plasma region.

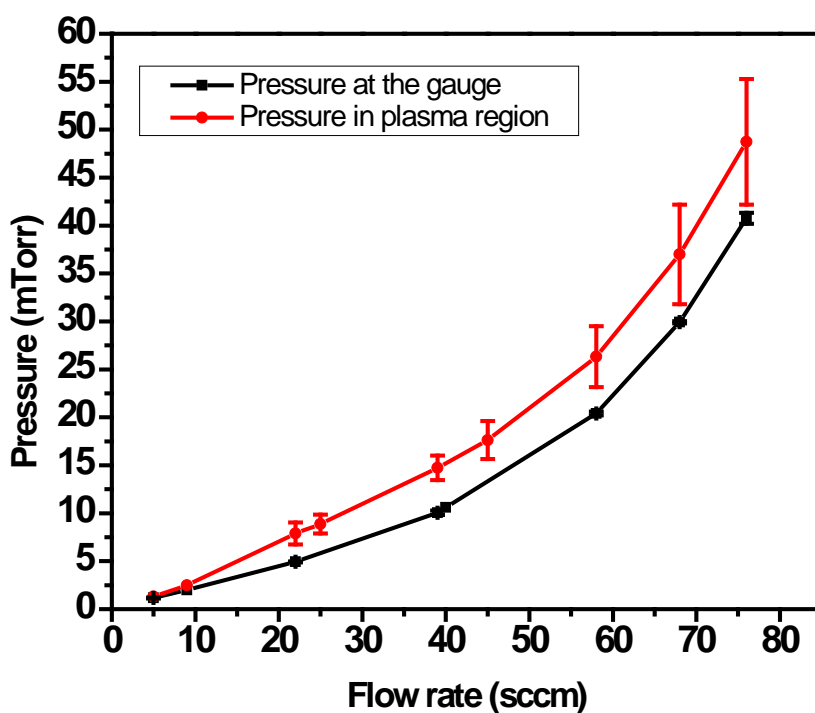


Figure 3.5: Pressure at the measurement (gauge) location (black), and pressure in the plasma region (red) vs. gas flow rate.

3.1.2 Sample bias setup

A water-cooled doughnut shaped sample stage (2 inches diameter) was mounted from the bottom flange of the cubic chamber. The “doughnut hole” (1 inch diameter) on

the stage allowed a rod, on which the sample holder was mounted, to move the sample up to the stage that was located in the middle of the plasma discharge region. The sample holder was cooled with a flow of water through the rod in contact with the bottom of the holder. A sapphire disk was glued with ceramic adhesive (Ted Pella Inc. 16026) on top of the rod to facilitate heat transfer between the sample holder and the rod.

The water-cooled (20 °C) SS sample stage was grounded (PAE condition) or powered by either a CW RF bias or a pulsed negative DC bias (IAE condition). For RF bias, a function generator (SRS D345) and an amplifier (Electronic Navigation Industries Model A-150) were employed to deliver 14.5 MHz power through a Π matching network of the same circuit design as that shown in Figure 3.3. The self-bias voltage was -70V or -140V with 8W or 20W, respectively, of RF net power applied to the sample stage with negligible reflected power. Pulsed negative DC bias was applied by amplifying (Avtech AVR-3-PS-UHF) a negative voltage square wave pulse (Berkeley Nucleonics Corporation, model 645) with a frequency of 10 kHz and peak-to-peak voltage of 5V. The ion energy with bias ON was assumed to be the difference between the plasma potential and the bias voltage, with $V_p = 5V$ at 60 mTorr.¹⁸ The ion energy with bias OFF (grounded stage, PAE condition) was ~ 5 eV, commensurate to the plasma potential. A four-channel oscilloscope (Agilent DSO 7034B) was used to monitor the signal waveforms.

3.1.3 Sample preparation

The etching rate experiments were performed using SiO₂ (1 μ m thick) masked p-type Si (100) substrates with resistivity 5-100 Ω -cm (Novati Technologies, Inc.). XPS surface characterization was performed using p-type Si (100) substrates with resistivity 10-

20 Ω -cm. Si wafers were cleaved into $\sim 1.1 \times 1.1$ cm² square pieces, cleaned with acetone and methanol to remove carbon contaminants, and blown dry with nitrogen. Before the actual etching experiment, the native oxide was removed by applying a high bias to the substrate stage etching for a few seconds.

The face of the 2.54 cm-diameter SS sample holder was covered with a 1.95 cm diameter highly doped p-type Si disk (resistivity 0.001-0.005 Ω -cm), soldered with indium foil, to prevent metal contamination due to SS sputtering. Low Si disk resistivity and indium soldering under a dry N₂ purge were found to be essential to minimize the voltage drop between the DC power supply and the surface of the Si disk. Samples were bonded to the Si disk using either silver paste (Mung II) for XPS measurements, or indium foil for etching rate measurements, to ensure good thermal and electrical contact. In addition, both the back side of the sample and the Si disk were scribed by a diamond tip to break the native oxide, helping to make good electrical contact.

For indium soldering, the Si disk was first placed in the middle of the sample holder with a 1 cm² indium foil in between. A heavy metal weight was placed on top of a piece of glass then on top of the Si disk to ensure good thermal contact and not drain the heat to the metal weight directly. Then N₂ purge gas started to flow to remove the air inside the housing to avoid oxidation of the indium foil while being heated up. After 5 minutes of N₂ purge, the sample was heated up to 200 °C by a hot plate for another 5 minutes. Then the heat was turned off, and the sample was cooled down with N₂ purge gas constantly flowing over the sample. Note that the temperature was measured on the hot plate, and the melting point of indium is 156.6 °C. Compared to the silver paste, indium foil soldering provided a more horizontal and flatter surface, which made the collection of the reflected laser beam

through the viewport relatively easier. Figure 3.6 shows the final arrangement of sample after indium soldering.

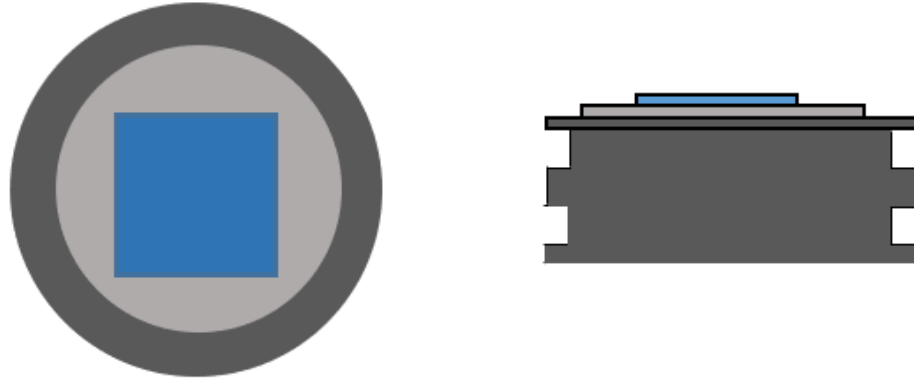


Figure 3.6: Top view (left) and side view (right) of sample (blue) on top of Si disk (grey) and sample holder (black).

To make sure there was minimum corrosion of the indium (and loss of electrical contact) during etching, the voltage difference between the sample surface and the applied negative DC bias was measured before and after etching in 7 separate cases at atmospheric pressure and was found to be 7 ± 3 V (one set of data is shown in Figure 3.7). This voltage difference was accounted for in obtaining the actual DC bias seen by the sample.

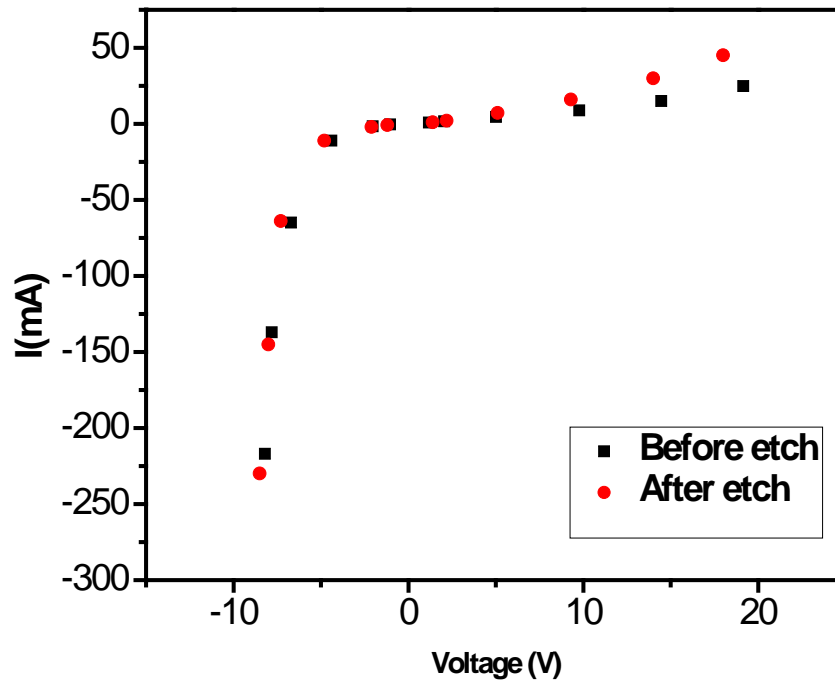


Figure 3.7: I-V curve measured at atmospheric pressure for sample + Si disk + sample holder both before etching (black squares) and after etching (red dots).

Previously, a temperature rise of ~ 200 °C was observed after a few minutes of etching Si with -50 V DC sample bias, when samples were not thermally bonded to the water-cooled stage.¹⁷ The temperature of the substrate was not measured in the present study, however, with much better thermal contact between the sample and the water-cooled stage, the temperature rise is expected to be much less. In addition, data were collected in a random order to minimize systematic errors due to any temperature dependences, which are expected to be small, as well as any other adverse effects.

3.2 Etching rate measurements

3.2.1 Laser interferometry

Real time etching rates were measured by laser interferometry.⁵⁰⁻⁵² A 632.8 nm He-Ne laser beam (Lumentum Model 1103 2mW) at normal incidence was reflected off the sample, focused by a lens of 10-inch focal length, and detected with a photodiode (Figure 3.2). An iris was used to restrict the field of view allowing only 0th order beam (reflected beam) to be collected. The signal was digitized and recorded with a Labview program. The pitch width (line + space) of the SiO₂ mask pattern was 100 μm at 50% density. Interference between reflections off the top of the oxide mask and the silicon substrate caused the intensity of the reflected beam to oscillate as a function of time with a period corresponding to an etched depth $\Delta d = \lambda/2$ at normal incidence, where λ is the laser wavelength. Interference persisted until the SiO₂ mask was slowly etched away or increased surface roughness led to significantly low reflected beam intensity. To evaluate the possible errors introduced by etching of the SiO₂ mask, the etching rate of blanket SiO₂ using either RF bias or pulsed negative DC bias was also obtained by either laser interferometry or spectroscopic ellipsometry (see next section).

In a more general case, one period of the interferogram (between two maxima or two minima) corresponds to a change in film thickness

$$\Delta d = \frac{\lambda}{2\sqrt{n^2 - \sin^2\theta}}, \quad (3.1)$$

where n is the index of refraction at this wavelength, and θ is the incident angle between the laser beam and the normal to the surface. In our case, n equals 1 for vacuum, and θ is 0.

A sample interferogram is shown in Figure 3.8. Light intensity increased once plasma was ignited. The sample immediately started to etch, when -67 V DC bias was applied. The signal was manually blocked from the detector to mark the change of experiment conditions (from IAE to PAE condition) resulting in a vertical line on the interferogram. Then light intensity decreased roughly to the original level, when the plasma was turned off.

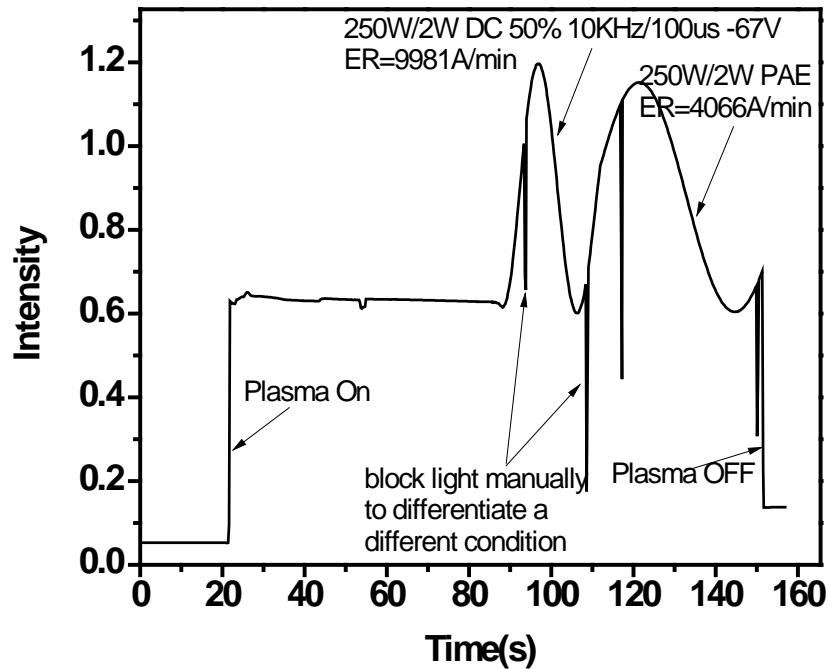


Figure 3.8: A sample interferogram.

3.2.2 Spectroscopic ellipsometry

Spectroscopic ellipsometry (SE) is a nondestructive diagnostic method that uses polarized light to characterize thin films, surfaces, and material microstructure by measuring the change of polarization state of a light beam upon reflection or transmission through the surface of a sample. The polarization state of a light beam refers to the path its electric field traces as it propagates through space and time. The most common application of SE are measurements of thin film thickness (single or multiple layers) and optical constants. For many samples, SE is sensitive to film thickness on a sub-monolayer level. It has been proven to be the primary technique for determining the optical constants in UV, visible, and IR wavelength ranges as well. It can also be used to investigate surface and interfacial roughness, doping concentration, crystallinity, and optical anisotropy.⁵³⁻⁵⁶ Figure 3.9 is a schematic of an ellipsometer. Polarized light from a Xenon arc lamp, in the 250-850 nm wavelength range, was directed onto the film surface with incidence angle Φ . A rotating analyzer followed by a detector was used to analyze the reflected beam. The compensator, an optical component used to induce a phase change in the p- or s-component of a light beam, was used to improve the measurement accuracy over the full range of amplitude ratio Ψ (0-90°) and phase shift Δ (0-360°) (defined below).

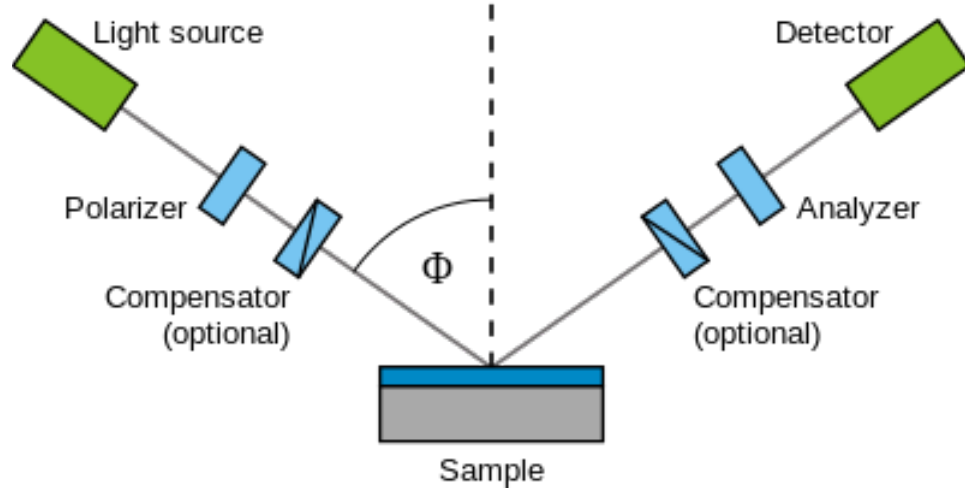


Figure 3.9: Schematic setup of an ellipsometry experiment (from wikipedia.org).

In SE, the measured signal is the change in polarization as the incident radiation interacts with the material structure of interest. The polarization change is quantified by the amplitude ratio Ψ and phase shift Δ , which are defined by

$$\tan(\Psi) e^{i\Delta} = \rho = r^p / r^s, \quad (3.2)$$

where ρ is the Fresnel reflection coefficient ratio (a complex number), and r^p and r^s are the Fresnel reflection coefficient for light polarized parallel (p-polarized) and perpendicular (s-polarized) to the incidence plane, respectively. The incidence angle Φ is usually chosen to be close to the Brewster angle of the sample to ensure a maximum difference between r^p and r^s to achieve maximum sensitivity. Because the measured signal depends on the material properties as well as film thickness, SE can be a universal tool for contact free determination of thickness and optical constants of films.⁵⁷

SE does not measure the sample parameters of interest directly, rather it measures some quantity that is a function of the sample parameters, so it is necessary to fit the sample

parameters to the measured data with a model to ensure the predicted quantity by the model best matches the data. The measured sample usually consists of several layers of films. A structural model must be built first to simulate the stacking layer structure of the sample, then the calculated Ψ and Δ based on the model structure are compared with the experimental measurements. The difference between these two is quantified with a mean square error (MSE). By fitting or minimizing the MSE between the model and experimental data, the film thickness can be determined from the best-fit model.^{56,58,59}

In this study, SE (J. A. Woollam Co., Inc. M-2000) was used to measure *ex-situ* film thickness change or etching rates for SiO₂ under certain conditions, when the etching rates were too slow to be measured by laser interferometry.

3.3 Surface characterization

3.3.1 X-ray photoelectron spectroscopy

XPS, also known as Electron Spectroscopy for Chemical Analysis (ESCA), is a widely used analytical technique for obtaining quantitative chemical composition within the top 3-5 nm of solid surfaces. XPS is accomplished by irradiating a sample with monoenergetic soft X-rays and analyzing the energy of the electrons emitted. Both Mg K α (1253.6 eV) or Al K α (1486.6 eV) are ordinarily used as X-ray sources. These photons penetrate on the order of 1-10 micrometers into the solid and interact with atoms in this surface region leading to ejection of core level electrons through photoelectric effect.

The kinetic energy (KE) of the emitted photoelectrons is given by

$$KE = h\nu - BE - \phi_s, \quad (3.3)$$

where $h\nu$ is the characteristic energy of the incident X-ray photon, BE is the electron binding energy of the atomic orbital from which the electron originates, and ϕ_s is the spectrometer work function. The energy distribution of electrons ejected from the near-surface region of the sample, while being irradiated by X-rays, contains information regarding the chemical state, electronic structure, and elemental composition of the sample being studied. XPS detects all elements except H and He, and it provides quantitative and qualitative elemental analysis within $\pm 5\%$ error.⁶⁰ Figure 3.10 is a schematic of XPS measurements.⁶⁰

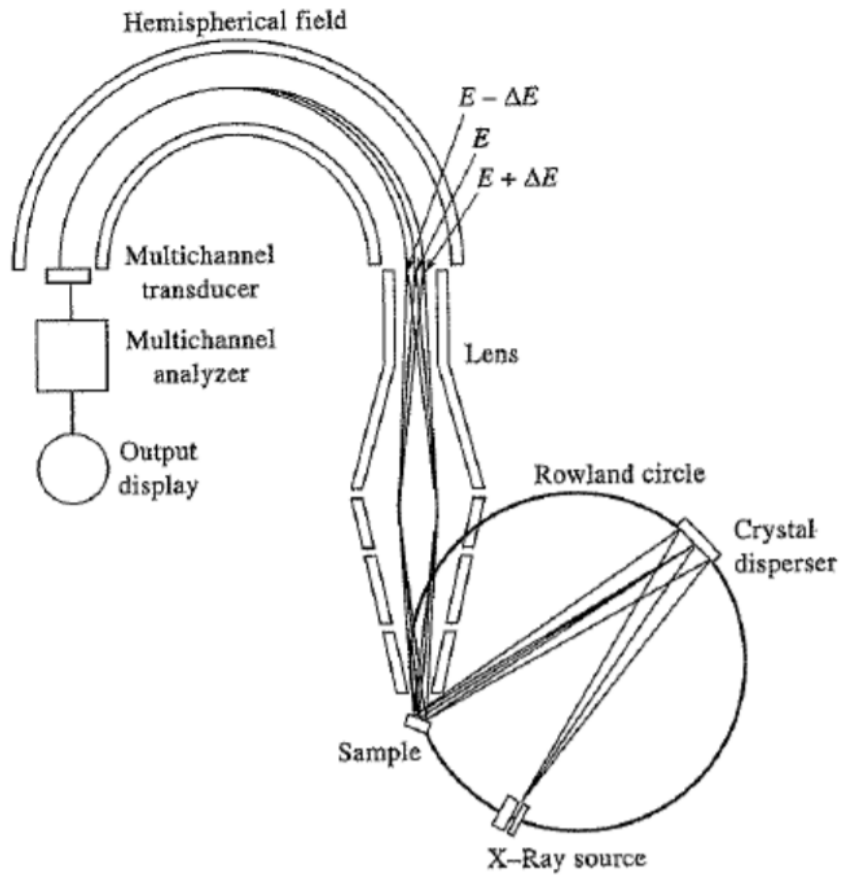


Figure 3.10: Schematic setup of XPS measurements.⁶⁰

The probability of interactions between electrons and the matter far exceeds that of the photons, so the path length of the electrons is only of the order of nanometers, while that of the photons is of the order of micrometers. The intensity of the electrons emitted from the surface decays exponentially as the depth increases, which is given by the Beer-Lambert law

$$I(d) = I_0 e^{-d/(\lambda(E)\sin\theta)}, \quad (3.4)$$

where $\lambda(E)$ is the inelastic mean free path (IMFP) described by a universal curve,^{61,62} I_0 is the intensity of the electrons ejected from an atom at depth d , and $I(d)$ is the intensity at the surface after the electrons have traveled a distance of d through the solid. The angle θ is usually defined as the angle between the photoelectron vector and the sample surface plane, often called the take-off angle. Thus, only those electrons that originate within a few nanometers below the solid surface can leave the surface without losing energy. It is these electrons which produce the peaks in XPS spectra, carry the information of the elemental composition, and therefore are the most useful. On the other hand, those that undergo energy loss processes before leaving the solid surface form the background signal in spectra. The electrons leaving the sample are detected and analyzed by an electron spectrometer according to their kinetic energy. By scanning the potential applied, the energy distribution of electrons passing through the analyzer can be obtained.⁶⁰

Angle-resolved XPS is a technique to determine the depth profile of a sample non-destructively by simply varying the take-off angles of the measurements, which can

effectively change the detection depth. As the take-off angle decreases, the detection depth decreases due to a shorter vertical distance the photoelectrons can travel with constant escape depth of the photoelectrons. Therefore, the resulting data is more surface sensitive.

Figure 3.11 demonstrates the principle of angle-resolved XPS.

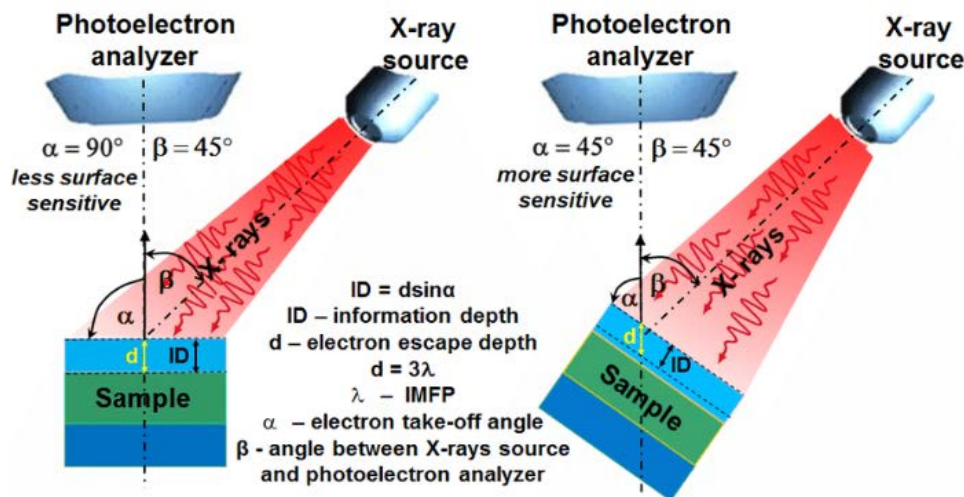


Figure 3.11: Principle of angle-resolved XPS.⁶³ Detection depth decreases as take-off angle decreases, resulting in a more surface sensitive analysis.

In addition to the photoelectrons emitted in the photoelectric process, Auger electrons are emitted, roughly 10^{-14} seconds after the photoelectric event. In the Auger process, an outer electron falls into the inner orbital vacancy created by photoemission, and a second electron (“Auger electron”) is emitted, carrying off the excess energy. Figure 3.12 shows the diagram of photoelectric process and Auger process.⁶⁴

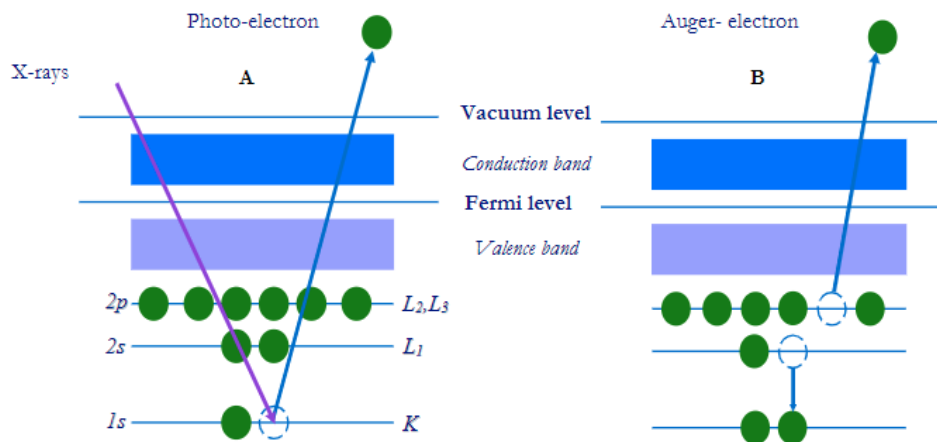


Figure 3.12: Diagram of photoelectric process (left) and Auger process (right).⁶⁴

After etching, the sample was transferred under vacuum to an ultrahigh vacuum (UHV) ($\sim 6 \times 10^{-10}$ Torr base pressure) analysis chamber equipped with XPS (Surface Science Instruments M-Probe). A monochromatic Al K α X-ray beam ($\lambda = 0.83$ nm, with a photon energy of 1486.6 eV) was obtained by diffracting and focusing the beam onto the sample utilizing a quartz crystal. The sample, sitting on the stage, could be manipulated in x-, y-, and z- directions to perform surface analysis over different spots. It could also be tilted with respect to the incident beam for angle-resolved XPS to obtain the depth profile of chemical species. Measurements were carried out at take-off angles of 30° and 85° with probing depths of 11 and 22 Å for Si, respectively.⁶⁵ Photoelectrons ejected from the sample were collected with a hemispherical kinetic energy analyzer having a $\pm 15^\circ$ acceptance cone. The system is also equipped with an electron flood gun that can be used to neutralize the charge developed on an insulating sample during analysis.

Low resolution (1 eV/step) XPS spectra were recorded over 0-1000 eV using an 800 μm diameter X-ray beam and resolution 4 with 5 scans. The integrated intensities along

with the corresponding sensitivity factors of the core-level peaks were used to determine the elemental composition and total chlorine content of the surface. High resolution (0.065 eV/step) spectra of the Si(2p) region from 95 to 105 eV were also recorded to determine the stoichiometry of the chlorinated surface using a 250 μm diameter X-ray beam and resolution 1 with 500 scans. Samples were etched for ~ 1000 Å based on the etching rates measured before XPS analysis. The simultaneous cessation of both source and bias power defined the end of the etching period⁶⁶ and established the conditions of the film that was subsequently analyzed by XPS.

3.3.2 Scanning electron microscopy (SEM)

A SEM utilizes a focused high-energy electron beam to scan across the surface of the sample systematically and detects scattered secondary electrons. The impinging electrons are accelerated towards the sample having substantial quantities of kinetic energy, then lose their energy by generating multiple signals from the interactions with the sample, such as secondary electrons, backscattered electrons, X-rays photons, and visible light from cathodoluminescence.⁶⁷⁻⁷² Secondary electrons, possessing very low energies on the order of 50 eV, can accurately mark the position of the beam (highly localized) and provide morphology and topography information with good resolution.⁷²

In this study, SEM (FEI Model XL-30S FEG, Nanofabrication Facility of University of Houston) was used to obtain images of samples with SiO₂ masked features. The e-beam energy was 10 to 15 keV. Samples were uncoated.

Chapter 4 – Comparison of Silicon Surface Chemical Composition between IAE and PAE

4.1 Introduction

Chlorine plasmas are widely used to etch silicon and other materials used in the semiconductor industry. The exposure of silicon to a chlorine plasma leads to chemical and structural modifications of the near-surface region and formation of a chlorinated layer, which is subsequently removed by ion bombardment in the Si etching process.⁷³⁻⁷⁵ The nature of this chlorinated surface layer including its thickness, stoichiometry, and structure was systematically studied by Donnelly *et al.* around 20 years ago.^{65,76,77}

4.1.1 Nature of the chlorinated surface layer of Si (100) after etching under IAE condition

In 1997, Layadi, Donnelly, and Lee studied the silicon-chloride layer formed during IAE in a Cl₂ plasma as a function of ion energy and density with angle-resolved XPS.⁶⁵ The experimental apparatus is shown in Figure 4.1. A 16-turn quarter wave helical coil (4 inches diameter) with a ground shield (8 inches diameter) surrounded a vertical glass tube (2 inches diameter) forming the helical resonator source. Two 100 G solenoid magnets were used to confine the plasma. Polished p-type Si (100) sample was sitting in the downstream region of the discharge tube. Two different etching modes were used. In the reactive ion etching (RIE) mode, 14.5 MHz power was applied to the sample stage, and the helical resonator source was not powered. The electromagnets were off as well. In the

helical resonator (HR) etching mode, the HR source was powered with 300 W at a frequency of 11.26 MHz, and the sample stage was powered to induce DC bias voltages.

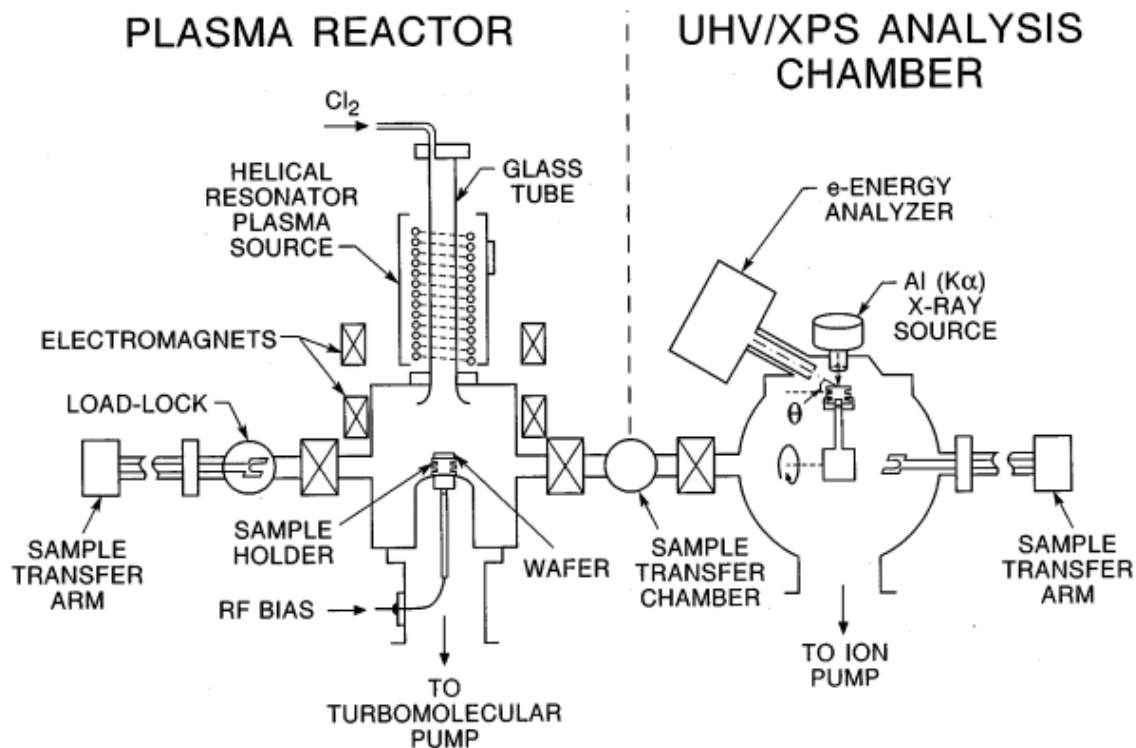


Figure 4.1: Schematic of the helical resonator plasma reactor and attached UHV/XPS chamber.⁶⁵

By measuring the integrated areas of the Cl and Si peaks from survey spectra as a function of take-off angle (θ) for different processing conditions (Figure 4.2), the authors showed that the relative Cl signal decreased with increasing θ . The highest ion energy (RIE, -240 V self-bias) led to the highest relative Cl signal (0.58 at $\theta=20^\circ$). On the other hand, low ion energy (HR, 0 V bias) produced the lowest relative Cl signal (0.39 at $\theta=20^\circ$). RIE and HR etching modes at the same ion energy (-75 V self-bias) produced surface layers with nearly identical Cl content, indicating that the degree of dissociation and ionization of Cl₂ (much higher for the HR etching) was relatively unimportant. In addition, XPS spectra

of Si samples etched for 30 and 300 s were almost identical (e.g., HR, 0 V bias in the inset of Figure 4.2), indicating the rapid formation of a saturated surface layer.

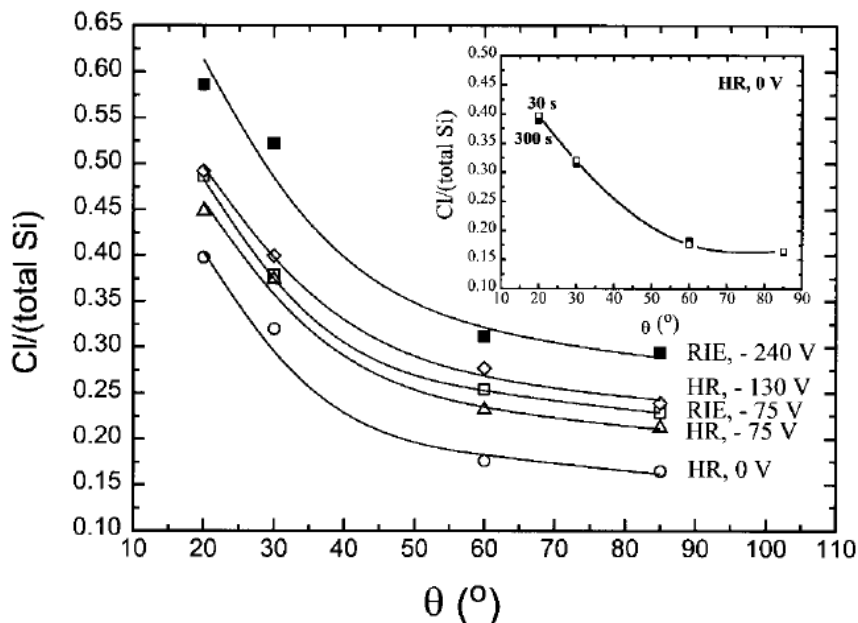


Figure 4.2: Cl(2p)/total Si(2p) signals (corrected with sensitivity factors) vs. θ in the near-surface region of Si (100) samples after etching for 30 s in Cl_2 plasmas under different processing conditions. The points are experimental data, and the curves are fits. The inset shows data (for 0 V bias) after etching for an additional 270 s for a total 300 s.⁶⁵

To determine the nature of the SiCl_x layer, the authors also recorded high resolution Si(2p) spectra. Figure 4.3 (a) shows that the spectrum of HF-cleaned, unetched Si consisted of an asymmetric peak at a binding energy of 99.4 eV due to the partially resolved $2p_{3/2}$ and $2p_{1/2}$ components of bulk Si. The Si(2p) peak broadened and its binding energy shifted to lower energy due to the creation of dangling bonds in the near-surface region after Ar^+ bombardment (4 keV). Its integrated intensity was roughly the same as that measured for HF-cleaned, unetched Si. After etching in a chlorine plasma under RIE conditions (-240 V self-bias), the integrated intensity of the Si peak at 99.4 eV decreased due to inelastic

scattering of electrons by chlorine on the surface. Additionally, a broad tail between 100 eV and 104 eV was attributed to SiCl , SiCl_2 , and SiCl_3 by peak fitting (Figure 4.3 (b)). A weak peak on the low binding energy side of the Si peak was attributed to Si^\bullet . The binding energies and widths were 98.8 (0.60), 99.30 (0.76), 100.21 (0.76), 101.16 (0.90), and 102.16 (0.73) eV for Si^\bullet , Si (bulk), SiCl , SiCl_2 , and SiCl_3 , respectively.

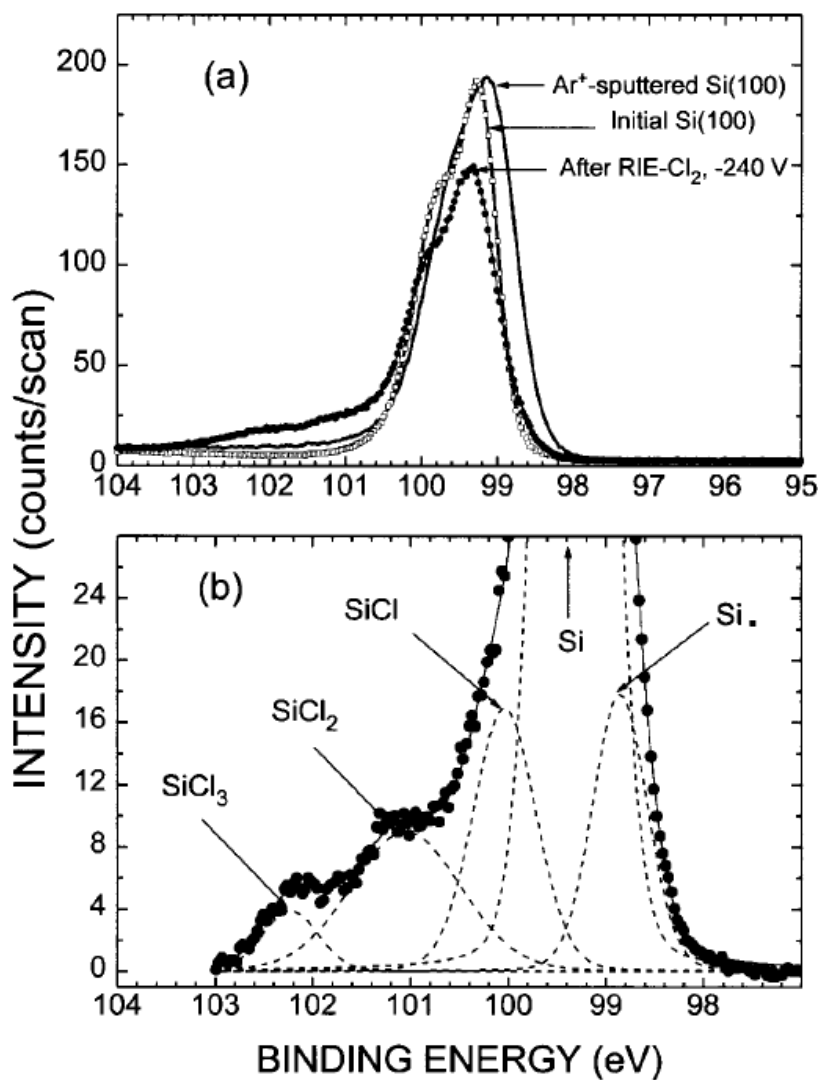


Figure 4.3: High resolution Si(2p) spectra at $\theta=30^\circ$ of: (a) HF-cleaned Si, Ar^+ -sputtered-cleaned Si, and plasma etched (RIE, -240 V self-bias) Si, (b) plasma etched Si with a Shirley-shaped background subtraction and $2p_{1/2}$ components removed. The fit (solid line) of the XPS spectrum (dots) included five peaks (dashed lines) with 85% Gaussian and 15% Lorentzian line shapes.⁶⁵

Depth profile was determined with maximum entropy approach⁷⁸ from take-off angle-dependent XPS data as well (Figure 4.4). These profiles showed that Si (bulk) was the predominant species throughout most of the layer, and Cl concentration peaked at the surface and fell off in a graded fashion. SiCl₂ and SiCl₃ were largely confined to the top 6 Å of the surface, and SiCl and Si• concentrations peaked below the surface and persisted to a depth of ~ 25 Å.

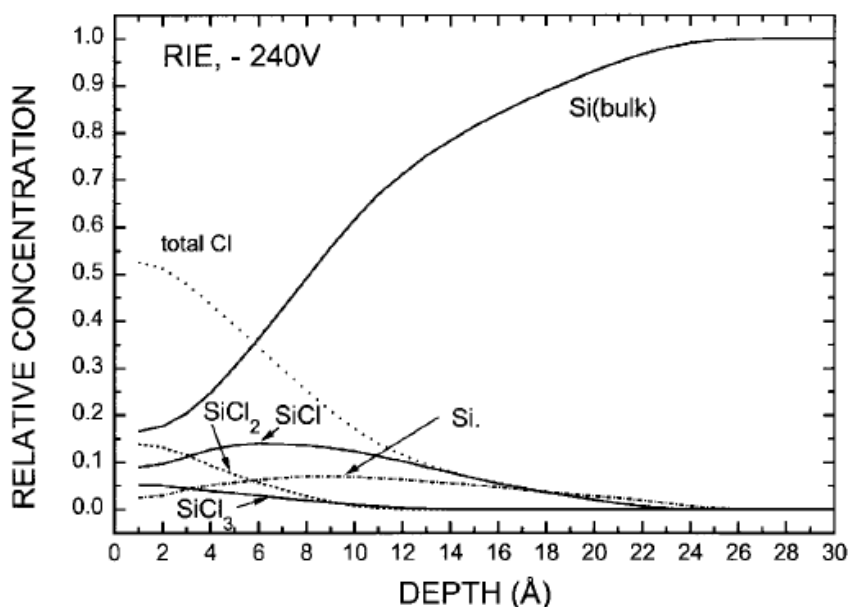


Figure 4.4: Depth profiles for bulk Si, Si•, SiCl, SiCl₂, and SiCl₃, determined from an inversion of take-off angle dependent XPS data for plasma etched Si (100) under RIE conditions at -240 V self-bias.⁶⁵

Finally, the authors concluded that the near-surface region of Si (100) during and after exposure to a chlorine plasma consisted of one monolayer or two where [SiCl₂] ~ [SiCl] > [SiCl₃], and a subsurface region of comparable or greater thickness where [SiCl] > [SiCl₂] and [SiCl] >> [SiCl₃]. Varying amounts of disordered Si including Si• were also

present. Higher ion energies increased the thickness of the layer and the total amount of Cl but had only a small effect on the Cl coverage at the surface, or the relative amounts of the SiCl_x species. Cl was detected to depths of ~ 13 to ~ 25 Å at mean ion energies of 40 and 280 eV, respectively (show in Figure 4.5 schematically). The increase in Cl with increasing ion energy was due to the creation of subsurface binding sites by chlorine ions.

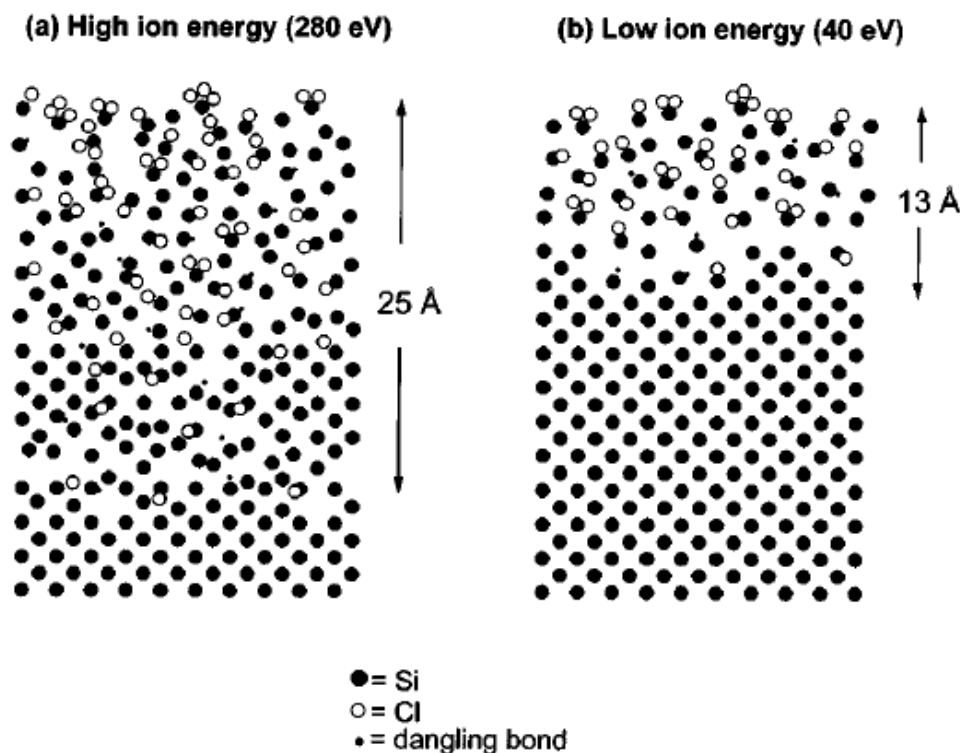
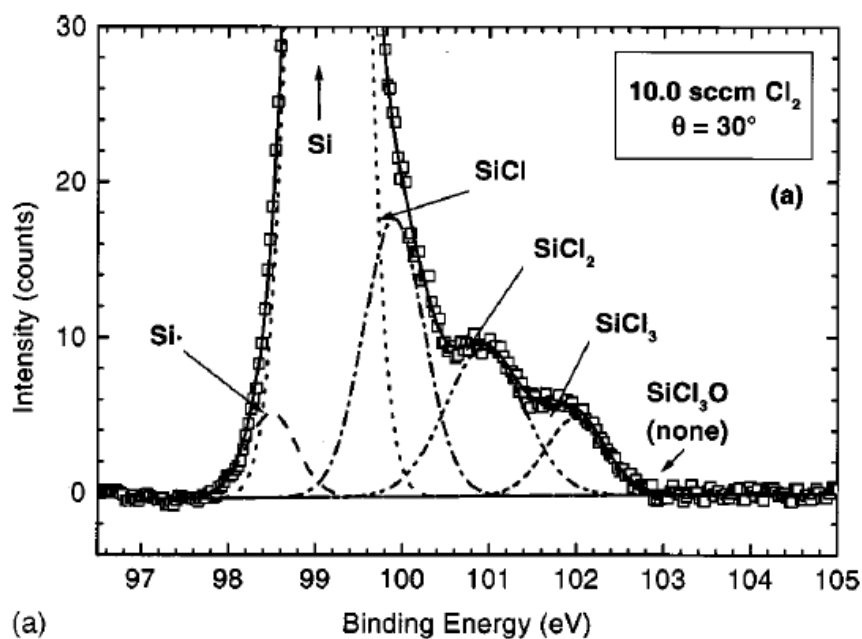


Figure 4.5: Schematic depiction of Si (100) surfaces after etching in a Cl_2 plasma for (a) RIE, -240 V self-bias (280 eV mean ion energy) and (b) HR, 0 V bias (40 eV mean ion energy).⁶⁵

In 1999, Bogart and Donnelly studied the effects of etching product concentration on the surface layer formed during Cl_2 plasma etching of unmasked crystalline p-type Si (100) in the same experimental setup.⁷⁶ By decreasing the Cl_2 flow rate from 10.0 to 0.4 sccm at a constant pressure 4 mTorr, the gas residence time was increased and the SiCl_y etching product density in the reactor was increased. This study showed that, in addition to

Si•, Si, SiCl, SiCl₂, and SiCl₃, a sixth peak at 103.3 eV was found at only low flow rates and was ascribed to a silicon oxy-chloride species (Figure 4.6). Its stoichiometry was likely SiCl₃O due to a 4 eV binding energy shift relative to bulk Si. Although the peak ascribed to SiCl₃O is at a binding energy expected for highly volatile SiCl₄, the Cl and O content measured by XPS ruled out this unlikely possibility. Overall, little difference was found in the SiCl_x composition of the chlorinated layer etched with Cl₂ flow rates of 10.0 and 0.4 sccm. The amounts of the three silicon chlorides and the total Cl were nearly independent of the product-to-etchant flux ratio.



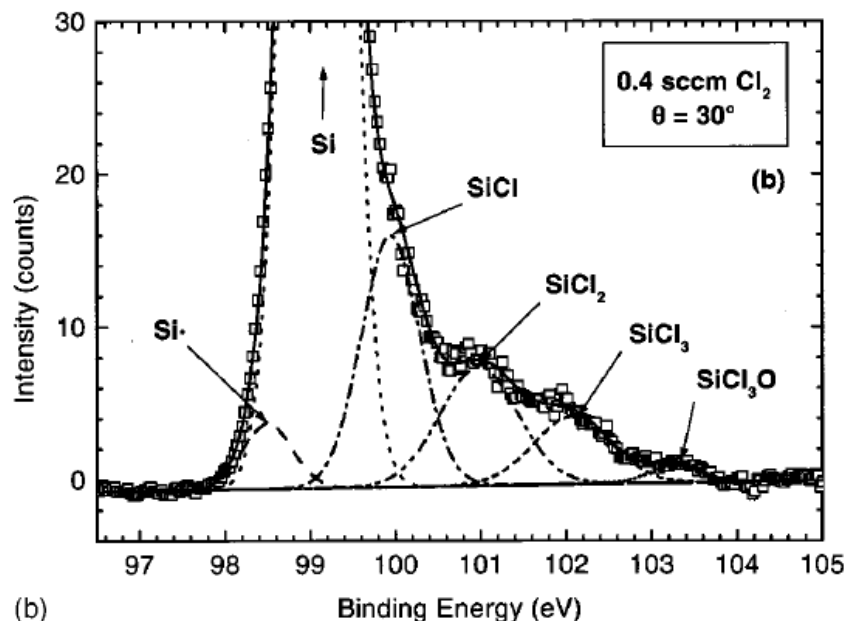


Figure 4.6: High resolution Si(2p_{3/2}) XPS spectrum acquired at $\theta = 30^\circ$ for Si etched in (a) 10.0 and (b) 0.4 sccm Cl₂ plasma. Empty squares are experimental. Broken lines are fits.⁷⁶

4.1.2 Surface chemistry composition of trench sidewalls for SiO₂-masked Si (100) after etching under IAE condition

Bogart and Donnelly also investigated the role of redeposition of silicon-chloride etching products, formed during Cl₂ plasma etching of SiO₂-masked p-type Si (100), on the trench sidewalls. In high-density plasmas with substrate bias power applied, the positive ion flux to the trench sidewall is significantly less than the flux to the horizontal trench bottom. Additionally, the ion energy transferred to the sidewalls by glancing-angle impact is much less than that occurring at near-normal incidence at the trench bottoms. On the other hand, the Cl neutral flux at trench sidewall and at the trench bottom is similar, as are the fluxes of secondary SiCl_y products formed by plasma-induced dissociation and/or heterogeneous recombination of primary etching products.⁷⁷

Figure 4.7 are the high resolution Si(2p) spectra taken at the appropriate θ (30° for $1.0\ \mu\text{m}$ features, and 45° for $0.5\ \mu\text{m}$ features) for probing the trench sidewalls and bottoms of the features in a $1.4\ \text{sccm Cl}_2$ plasma. Spectra from the Si unmasked area were also shown for comparison. The unmasked spectrum at $\theta = 60^\circ$ was used for comparison to the sidewall spectrum recorded at a take-off angle of 30° , since the effective take-off angle θ_{eff} on the sidewall was equal to $90^\circ - \theta$ (60°).⁷⁷

This study showed that the chlorine coverage and the silicon chloride stoichiometry were identical for the unmasked Si areas and the bottoms of the trenches with significant intensity between 100 and 102.5 eV, indicating that SiCl , SiCl_2 , and SiCl_3 were present in the chlorinated surface layer on the trench bottom. The trench sidewalls, however, contained roughly 50% less Cl than the unmasked areas, all in the form of SiCl .⁷⁷ In addition, it was found that the composition of the trench sidewalls and bottoms did not change with higher etchant and lower etching product concentration as the Cl_2 flow rate was increased from 1.4 to 10.0 sccm Cl_2 , and it was independent of line and space width as well.

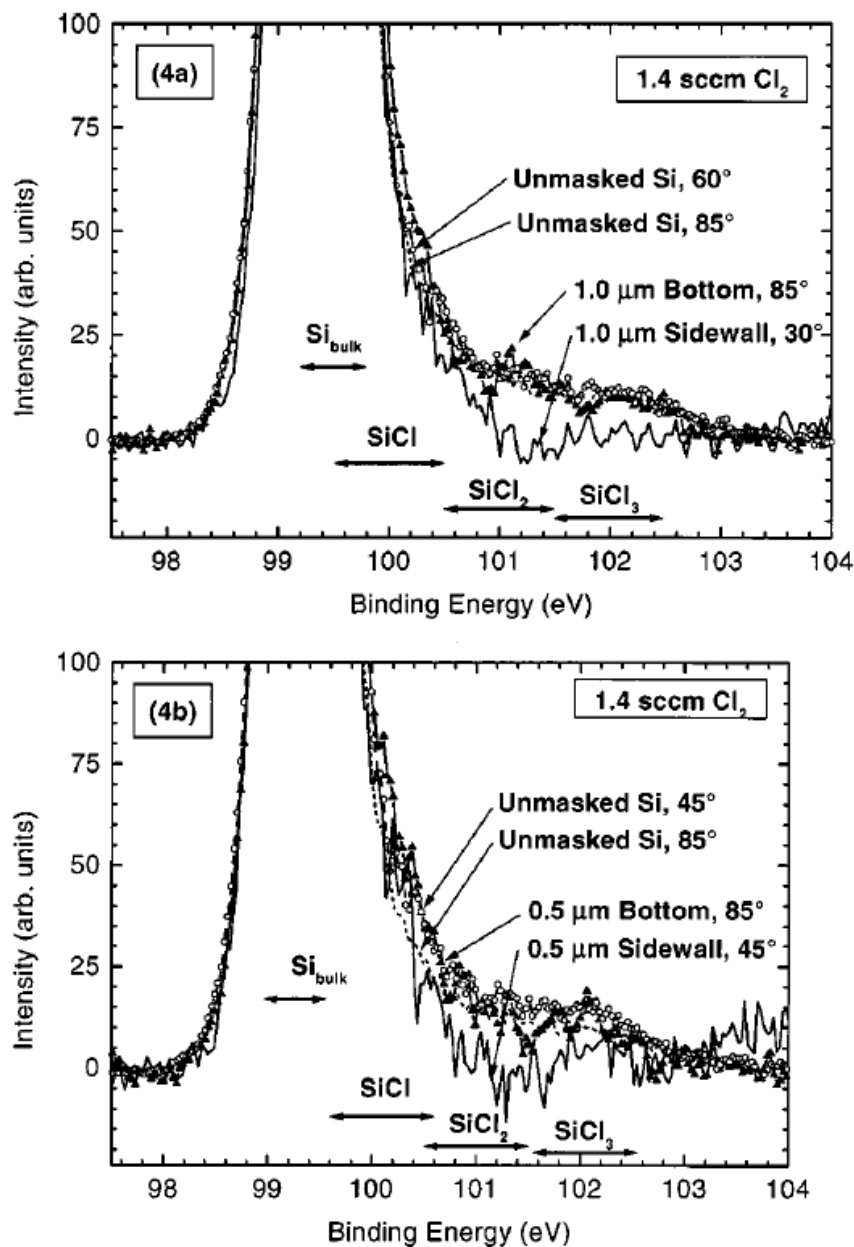


Figure 4.7: (a) Overlay of Si(2p) spectra from the 1.0 μm region, etched in a 1.4 sccm Cl₂ plasma, acquired at $\theta=30^\circ$ (sidewall, solid line) and 85° (trench bottom, solid triangles-line). Also shown are corresponding spectra from the unmasked Si (100) area obtained at $\theta_{\text{eff}}=60^\circ$ (open circles-line) and $\theta=85^\circ$ (dotted line). (b) same for 0.5 μm region.⁷⁷

4.2 Experimental details – high resolution spectra fitting procedure

First, a nonlinear Shirley-shaped background was subtracted from the raw XPS spectrum. Second, assuming a spin-orbit splitting of 0.61 eV and an intensity ratio ($2p_{3/2}/2p_{1/2}$) of 1.92 for Si(2p),^{79,80} the corresponding constraints were applied for each component with 95% Gaussian and 5% Lorentzian line shapes. Then, all peak widths were fixed to 0.7 in the first few iterations of the fitting procedure. In the end, all the parameters including binding energies, peak-center intensities, and peak widths were allowed to vary during subsequent iterations to obtain the integrated intensities for the Si-containing components. Minimal χ^2 values between the fitted spectra and the experimental data were used as the criterion for a good fit.

To determine the Gaussian percentage of the line shape, a sample coupon (~1.5 cm²) cut from a p-type Si (100) wafer (resistivity 10-20 Ω -cm) was cleaned with acetone and methanol, and then dipped into 48% HF solution to remove the oxide layer. This sample was quickly mounted on a 1-inch diameter SS sample holder and transferred into the XPS chamber for analysis without being etched. Takahagi *et al.* reported that HF treated Si surface has a hydrogen monoatomic layer terminating the dangling bonds of silicon and this hydrogen termination was found to have remarkable passivation effect against surface oxidation.⁸¹ A surface structure model was also presented (Figure 4.8) in the same study.⁸¹ In the present work, the collected high resolution Si(2p) spectrum after HF dip was fitted with bulk Si and SiH peaks (Figure 4.9) using the procedure mentioned above. The Gaussian component of the line shape was varied to obtain a good fit. At minimal χ^2 value, the Gaussian percentage of the line shape was determined to be 95%, then the corresponding Lorentzian percentage was 5%.



Figure 4.8: Surface chemical structure model of silicon single crystal after UV/HF cleaning with 1% HF solution.⁸¹

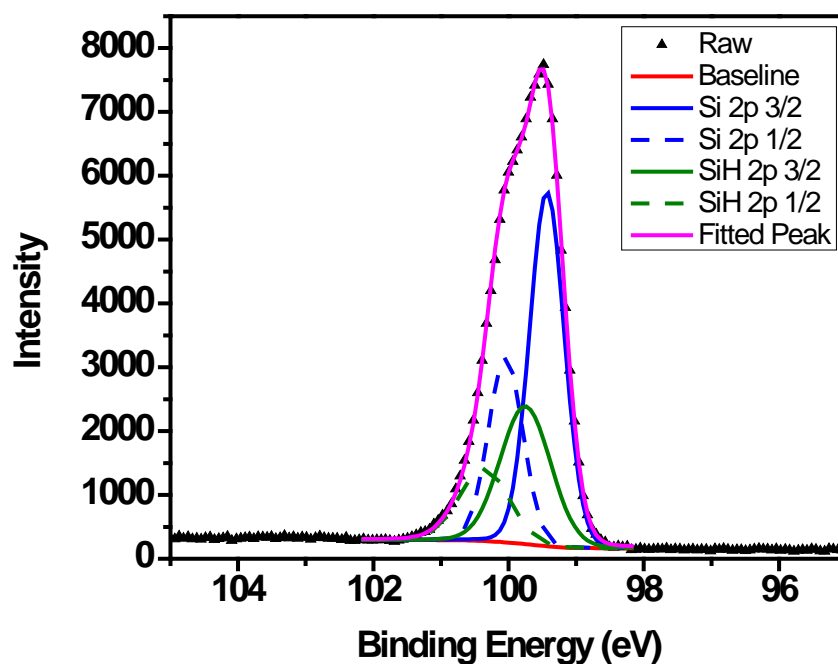


Figure 4.9: Peak fitting of high resolution Si(2p) spectrum at take-off angle 30° for p-Si after HF treatment.

4.3 Results and discussion

4.3.1 Low resolution survey spectra

In this study, we investigated the chemical composition of the chlorinated silicon surface under PAE condition as well as that under IAE condition. Table 4.1 displays the normalized elemental chemical composition of p-Si (100) derived from XPS low resolution survey spectra at take-off angles of 30° and 85° after etching in a 60 mTorr Cl₂/Ar plasma with the sample stage grounded (PAE condition) or RF powered with -70 V and -140 V self-bias voltage at low flow rate.

Table 4.1: Normalized elemental composition and relative chlorine concentration measured by XPS low resolution survey spectra at take-off angles of 30° and 85° for blanket p-Si after etching in 60 mTorr Cl₂/Ar plasma at low flow rate with the sample stage powered by RF (-70V and -140V self-bias) or without any bias (0 V, grounded).

	0V/30°	0V/85°	70V/30°	70V/85°	140V/30°
Si	84	90	70	81	66
Cl	16	10	29	18	34
O	--	--	1.0	1.6	0.8
[Cl]/[Si]	0.19	0.11	0.41	0.22	0.52

Figure 4.10 shows the corresponding survey spectra. Besides Si2p (99.6 eV), Si2s (150.9 eV), Cl2p (200.4 eV), and Cl2s (271.8 eV) core-level photoelectron peaks, trace amounts (<1% of the total Cl concentration) of O1s (533.9 eV) was also detected when RF bias was applied. No other species (e.g., C or metal) were detected. The source of the trace O contamination could be from sputtering of the alumina cap that covered the sample stage to prevent metal contamination.

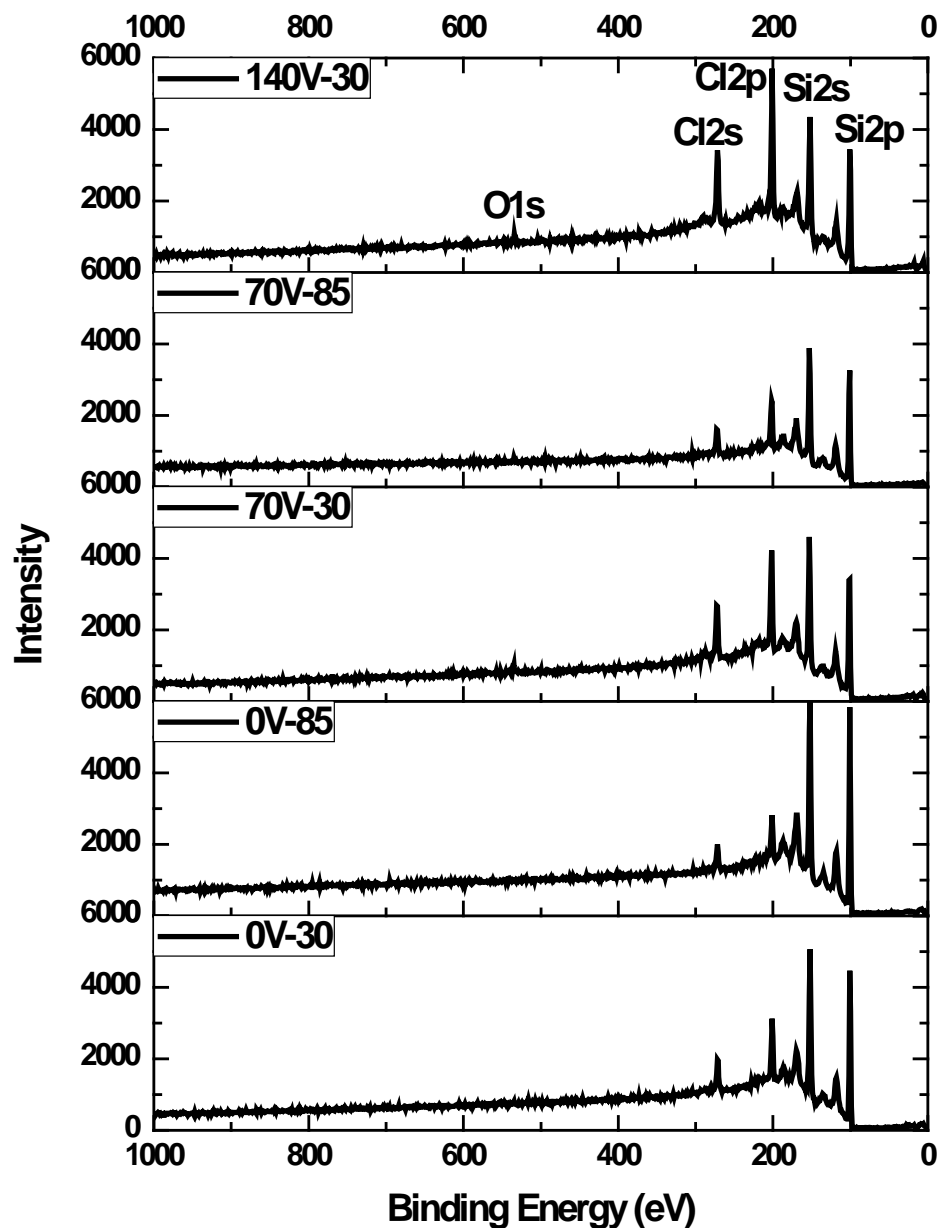


Figure 4.10: XPS low resolution survey spectra at take-off angle of 30° and 85° for Si after etching at low flow rate.

Si plasmon loss features were also observed at binding energies $\Delta BE = 17$ eV from the Si(2p) and Si(2s) peaks,⁶⁵ resulting from excitation of a collective oscillation of the bulk Si valence electrons.⁶⁰ Similar features at $\Delta BE = 34$ eV correspond to photoelectrons that have excited two bulk plasmon resonances. Resonant loss features were also observed

for Cl(2p) and Cl(2s) at RF -140 V self-bias voltage indicating that some Cl had penetrated deep into the underlying Si most likely due to high energy ions.

The relative chlorine concentration ($[Cl]/[Si]$) was calculated using

$$[Cl]/[Si] = \frac{A[Cl(2p)]/S[Cl(2p)]}{A[Si(2p)]/S[Si(2p)]}, \quad (4.1)$$

where $A[Cl(2p)]$ and $A[Si(2p)]$ are the integrated intensities of Cl(2p) and Si(2p) peaks of low resolution survey spectra, and $S[Cl(2p)]$ and $S[Si(2p)]$ are the corresponding sensitivity factors (2.285 and 0.817, respectively).⁶⁵ Both 2p spin-orbit components were included in the integration. The relative chlorine concentration is plotted as a function of the ion energy (V_p - bias voltage) in Figure 4.11. When the take-off angle (with respect to the sample surface) increases (red circle for 85°), the relative chlorine signal decreases, indicating that the chlorinated layer is mostly located at the upper most surface and its thickness is comparable to the electron inelastic mean free path.⁶⁵

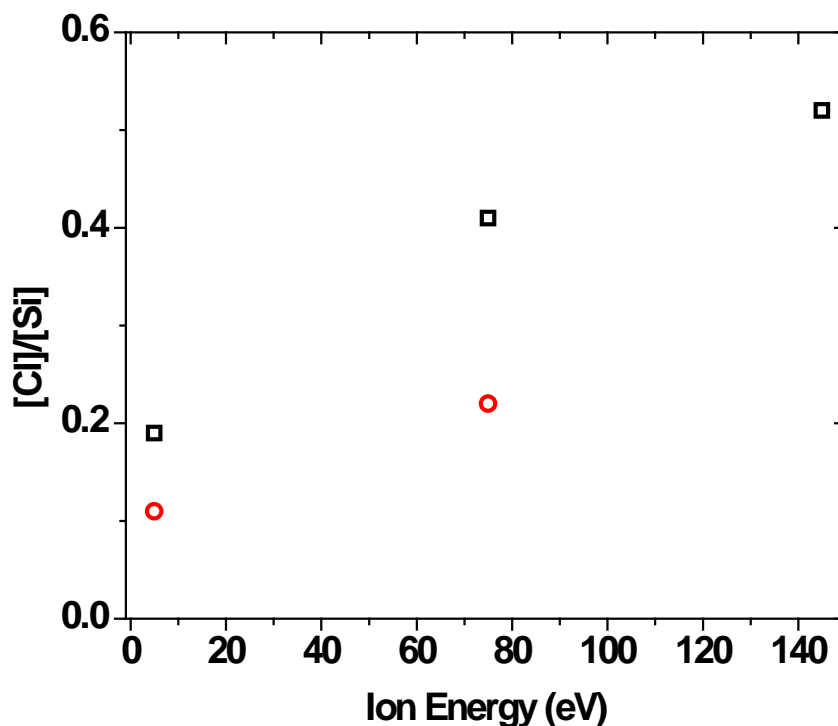


Figure 4.11: Relative chlorine concentration after etching in 60 mTorr Cl₂/Ar plasma obtained from XPS survey spectra at take-off angles of 30° (black squares) and 85° (red circles) at low flow rate.

The relative chlorine concentration increases with increasing bias voltage, as reported previously by Layadi *et al.*⁶⁵ The highest ion energy (145 eV for -140 V self-bias) leads to the highest relative Cl concentration (0.52 at 30°) compared to 0.41 at 30° with ion energy of 75 eV. On the other hand, the lowest Cl content was observed under PAE conditions (ion energy ~5V), resulting in a relative concentration of 0.19 at 30° and 0.11 at 85°. Consequently, the nature of the chlorinated layer under PAE without any energetic (above threshold-energy) ion bombardment appears to be very different from that of IAE.

4.3.2 High resolution spectra

High resolution Si(2p) spectra were also recorded to determine the nature of the chlorinated layer after etching. Figure 4.12 shows the spectra of the Si(2p) peak with the sample stage grounded (PAE), or RF biased (-70V or -140V self-bias) at take-off angles of either 30° or 85° at low flow rate. All spectra have been shifted to a common binding energy and normalized to the peak intensity of the -70V spectrum at 30°. At 85° take-off angle, the chloride tails are less intense on the high binding energy side (101 eV to 104 eV) for both -70V (red) and 0V (blue) as compared with those at 30° (black and green) indicating that most Cl bonded to Si is confined to the surface. Higher ion energy (larger bias) enhances the signals at high binding energy, which is consistent with the higher chlorine content derived from the low resolution survey spectra (Table 4.1 and Figure 4.11). Most importantly, a significant difference of the Si(2p) peak on the high energy side (101 eV to 104 eV) was observed between etching under PAE condition without bias (green) and IAE condition under RF bias (black for -70V self-bias, magenta for -140V self-bias), which is discussed below. In addition, the Si(2p) peak increasingly broadens on the lower energy side with increasing ion energy, showing a weak shoulder. This is due to the creation of Si dangling bonds by ion bombardment when the ion energy is above threshold.⁶⁵

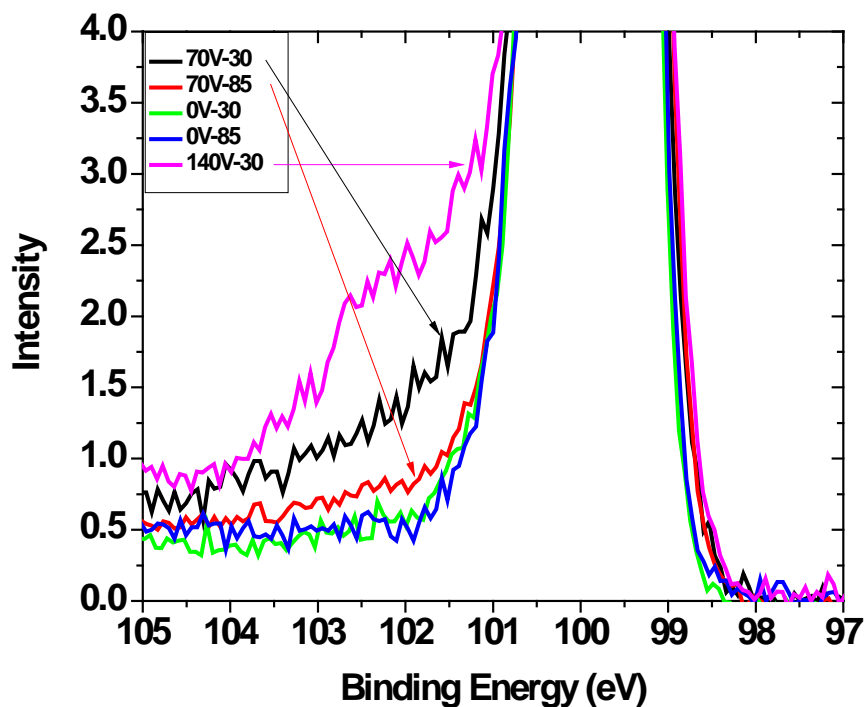
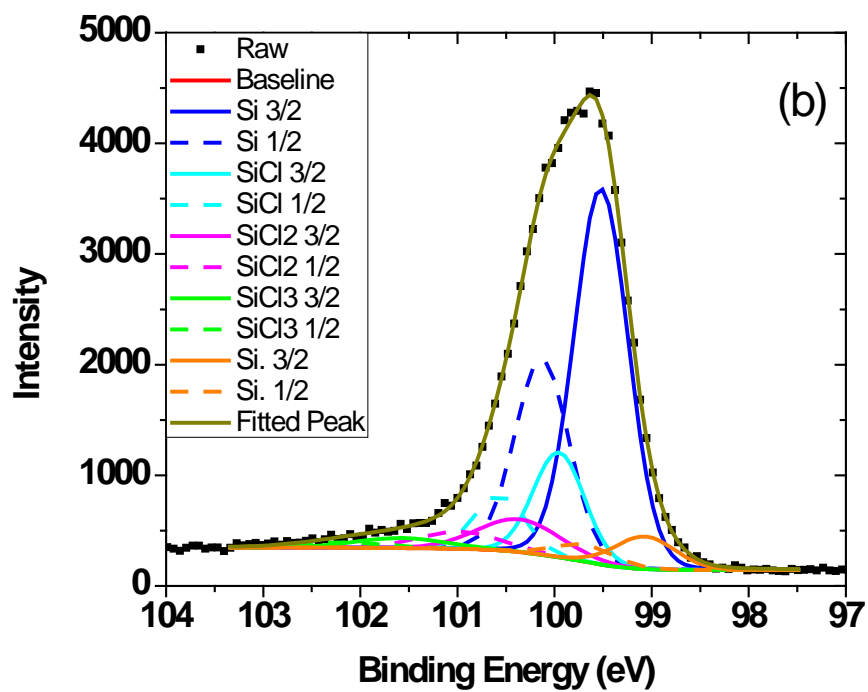
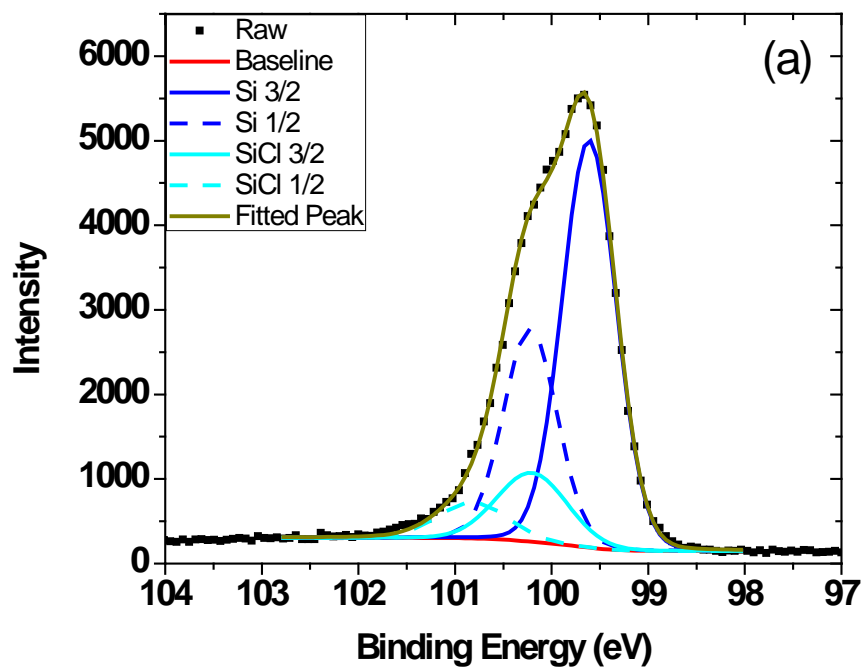


Figure 4.12: High resolution Si(2p) spectra at take-off angles of 30° or 85°. Etching conditions were 0V (PAE), RF at -70V self-bias, and RF at -140V self-bias, all at low flow rate. Intensities were normalized at the maximum near 100 eV.

4.3.3 High resolution peak fitting

The deconvoluted high resolution Si(2p) spectra (Figure 4.13) were obtained by peak fitting for various bias voltages (0V, -70V, and -140V). Excellent fits of Si(2p) spectra were obtained for all three cases with minimal χ^2 values between the fitted spectra (dark yellow line) and the experimental data (black squares).



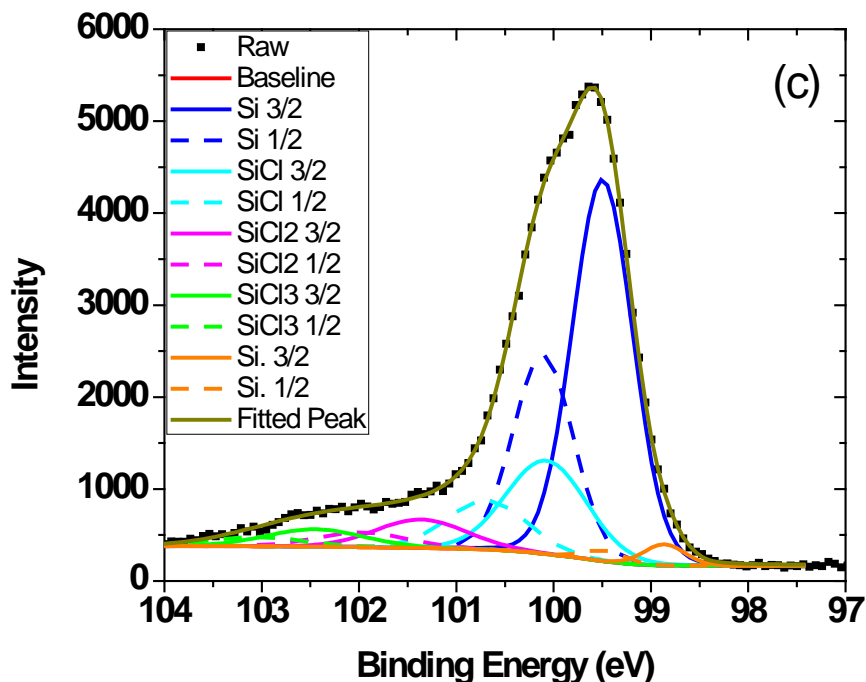


Figure 4.13: Peak fitting of high resolution Si(2p) spectra at take-off angle of 30°. Etching conditions were (a) 0V (PAE), (b) RF, -70V self-bias, and (c) RF -140V self-bias, all at low flow rate.

After etching under IAE condition with RF power on the sample stage (-70V self-bias: Figure 4.13 (b), -140V self-bias: Figure 4.13 (c)), much broader chloride tails appear from 101 eV to 104 eV, and the high resolution Si(2p) peak can be deconvoluted into 5 individual peaks. These peaks are attributed to Si with a dangling bond (Si•), Si(bulk), SiCl, SiCl₂, and SiCl₃, respectively, in agreement with the earlier studies by Layadi *et al.* and Bogart *et al.*^{65,76} The corresponding binding energies of the 2p_{3/2} component with -140V self-bias (Figure 4.13 (c)) are 98.8 eV (Si•), 99.5 eV (bulk Si), 100.1 eV (SiCl), 101.4 eV (SiCl₂), and 102.5 eV (SiCl₃), respectively. On the other hand, after etching under PAE condition, only 2 individual peaks can be identified by fitting the high resolution Si(2p) peak (Figure 4.13 (a)): one corresponding to the two spin-orbit components of Si(bulk) at 99.6 eV, and the other ascribed to SiCl at 100.2 eV. This dramatic difference of missing

higher chlorides (SiCl_2 and SiCl_3) and Si with a dangling bond ($\text{Si}\cdot$) under PAE condition is a clear indication that VUV photons and energetic ions are interacting with the Si surface very differently. The most likely explanation is that energetic ion bombardment disrupts the surface and sub-surface, leading to the formation of higher chlorides, while VUV light does not.

The relative chlorine concentration was also calculated based on the integrated area of individual deconvoluted SiCl_x peaks of the high resolution Si(2p) peak⁶⁵ given by

$$[\text{Cl}]/[\text{Si}] = \frac{(A[\text{SiCl}] + 2A[\text{SiCl}_2] + 3A[\text{SiCl}_3])}{(A[\text{Si}] + A[\text{Si}\cdot] + A[\text{SiCl}] + A[\text{SiCl}_2] + A[\text{SiCl}_3])}, \quad (4.2)$$

The calculated relative chlorine concentrations are 0.18, 0.43, and 0.50 for 0V, -70V, and -140V (solid black stars in Figure 4.14), respectively. The detailed calculations for each condition are listed as follows:

$$\text{at } 0\text{V} \quad \frac{[\text{Cl}]}{[\text{Si}]} = \frac{11626}{11626 + 53042} = 0.18, \quad (4.3)$$

$$\text{at } 70\text{V} \quad \frac{[\text{Cl}]}{[\text{Si}]} = \frac{3 \times 1650 + 2 \times 4929 + 9811}{9811 + 4929 + 1650 + 37193 + 3595} = 0.43, \quad (4.4)$$

and

$$\text{at } 140\text{V} \quad \frac{[\text{Cl}]}{[\text{Si}]} = \frac{3 \times 3720 + 2 \times 5646 + 16482}{16482 + 5646 + 3720 + 50472 + 1901} = 0.50. \quad (4.5)$$

There is a good agreement between the values of $[\text{Cl}]/[\text{Si}]$ derived from the low resolution survey spectra (black hollow squares in Figure 4.14) and the high resolution spectra. This also justifies the overall validity of the peak fitting procedure.

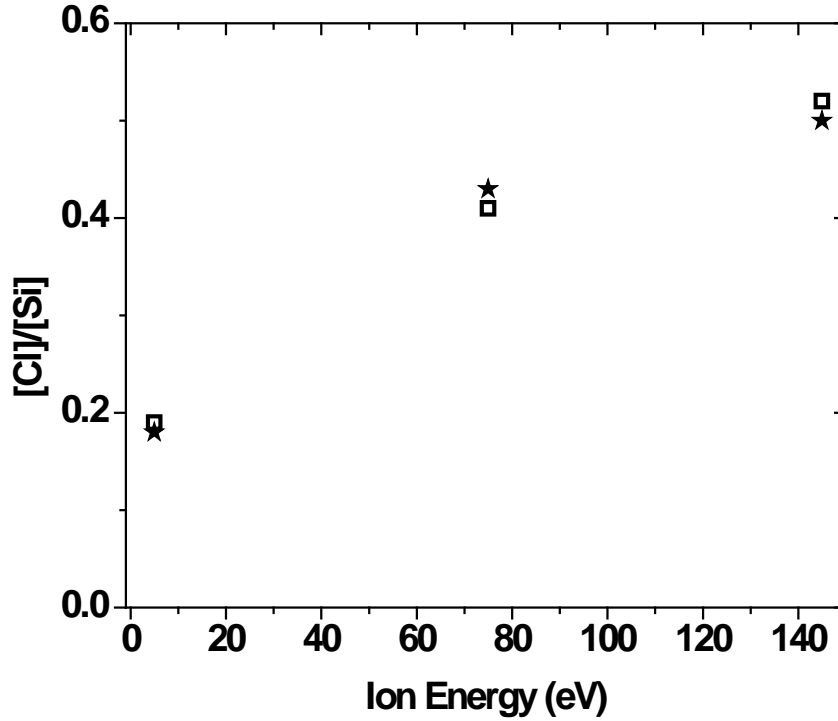


Figure 4.14: Relative chlorine concentration after etching in 60 mTorr Cl_2/Ar plasma obtained from XPS survey spectra at take-off angles of 30° (black squares) at low flow rate. Black stars were calculated based on the integrated areas of deconvoluted SiCl_x peaks obtained by high resolution XPS at 30° .

After etching under PAE condition, the near-surface region of Si (100) that consists of a chlorinated SiCl layer with higher chlorides absent is similar to the surface of trench sidewalls after etching, observed by Bogart *et al.*⁷⁷ This is reasonable because (energetic) ion bombardment is absent for both the sample surface under PAE condition, and the trench sidewalls during reactive ion etching. In contrast, with bias voltage applied, the chlorinated layer contains additional components including Si dangling bonds, SiCl_2 , and SiCl_3 . The integrated area of these SiCl_x ($x=1-3$) components shows that the ordering of their relative abundance is $\text{SiCl} > \text{SiCl}_2 > \text{SiCl}_3$, and the corresponding ratios are 1:0.50:0.17 at -70V and 1:0.34:0.23 at -140V self-bias, under RF biasing of the sample stage.

4.3.4 Duty cycle dependence of the Cl coverage

We also investigated the surface chemistry after etching with alternating IAE and PAE by varying the duty cycle of the pulsed DC bias. As shown in Figure 4.15, the chlorine coverage rises quickly with very little ion bombardment (less than 10% duty cycle) added for both high and low flow rate, then turns over and rises slowly. The slightly higher Cl coverage at low flow rate is just within the uncertainty of the measurement. Etching under a pulsed -70 V DC bias at 10 kHz gave a relative Cl concentration of 0.28 at 50% duty cycle at low flow rate, which is ~30% lower than the value (0.41) obtained under RF power (-70 V self-bias) applied continuously on the sample stage.

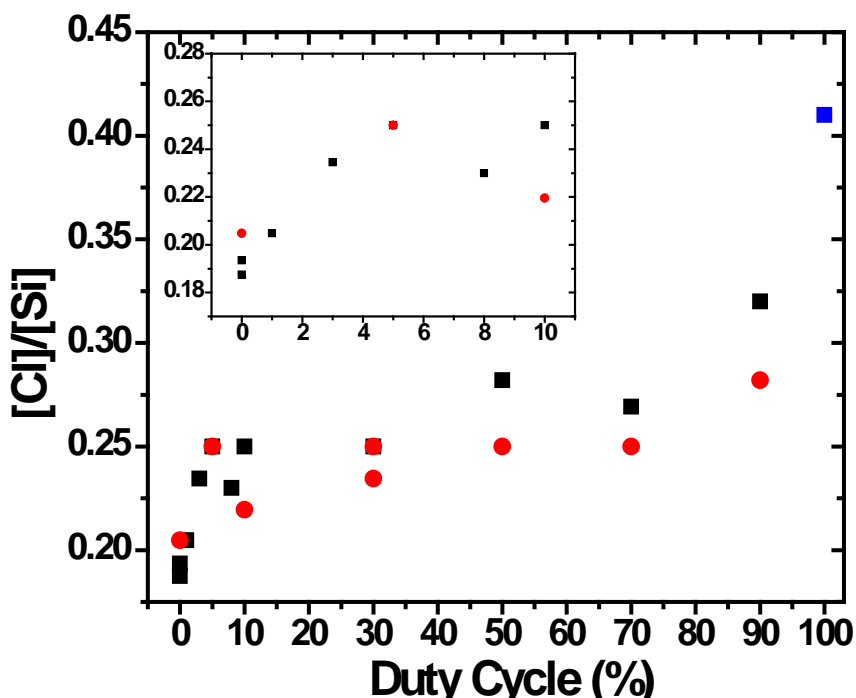


Figure 4.15: Relative chlorine concentration obtained from XPS survey spectra at take-off angle 30°. Etching conditions were RF -70 V self-bias (blue solid square) and pulsed -70 V DC bias at 10 kHz for low flow rate (black solid squares) and high flow rate (red solid dots). The inset is an enlargement of the region with duty cycle less than 10%.

The corresponding chloride tail with pulsed DC bias at 50% duty cycle between 101 eV and 104 eV of the high resolution Si(2p) peak in Figure 4.16 (black dash line) is also substantially smaller than that with RF bias at the same bias voltage (black solid line) and much larger than that after etching under PAE condition (red line). This is reasonable, since a bimodal energy distribution is obtained with RF bias, and higher energy ions are more efficient in creating chlorination sites.

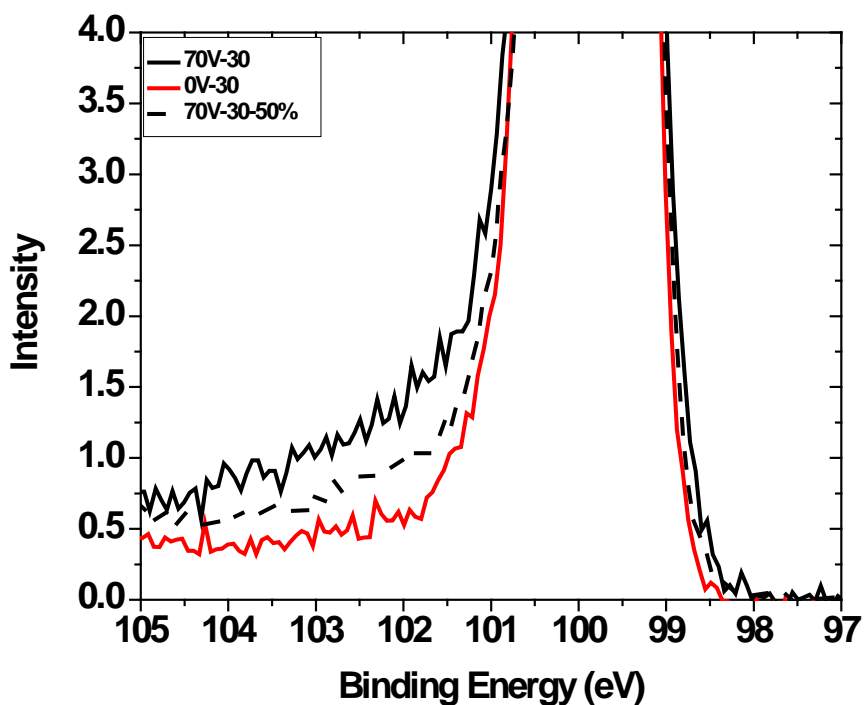


Figure 4.16: High resolution Si(2p) spectra at take-off angle 30°. Etching conditions were 0V (PAE) and RF at -70V self-bias at low flow rate. Intensities were normalized at the maximum near 100 eV. The black dashed line is from a sample etched under pulsed -70V DC bias with 50% duty cycle at 10 kHz, also at low flow rate.

Chapter 5 – Anti-synergism Between IAE and In-Plasma PAE of Silicon in a High-Density Chlorine Plasma

5.1 Introduction

Synergy between reactive neutral and energetic ion bombardment was first proposed in studies by Coburn and Winters in 1979⁹ that revealed one of the fundamental mechanisms of anisotropic plasma etching for the pattern transfer applications in microelectronics. The synergy in this case is due to the fact that the magnitude of the etch rate is greater than the sum of the ion bombardment physical sputtering rate and a chemical etching rate by the fluorine source (XeF_2).

The experiments were conducted by directing an ion beam onto a sample coincidentally or separately with the flux of reactive gas, and etching rates were measured using quartz crystal microbalance.⁹ The Si sample was first exposed to the XeF_2 gas, then to an Ar^+ beam and the XeF_2 gas together, and finally to the Ar^+ beam alone. The authors demonstrated that the etching rate of Si obtained with both the Ar^+ beam and the neutral XeF_2 gas simultaneously incident on the surface to simulate a real plasma was much higher (~ 8 times) than the sum of the etching rates of each species measured separately (Figure 5.1).

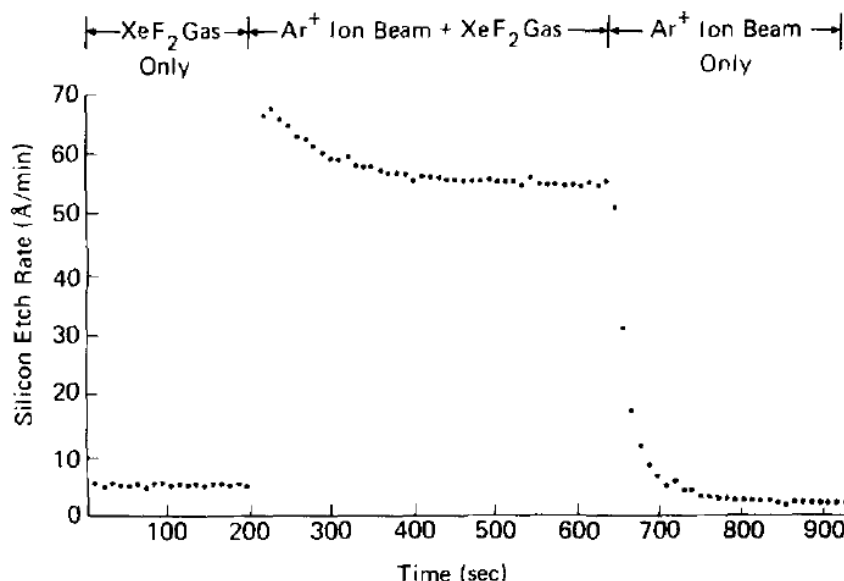


Figure 5.1: Synergistic etching of Si by Ar⁺ ion beam sputtering and XeF₂ chemical etching. Ar⁺ energy = 450 eV, Ar⁺ current = 0 (t < 200 sec), Ar⁺ current = 2.5 μ A (t > 200 sec), XeF₂ flow = 2×10^{15} mol/sec (t < 660 sec), and XeF₂ flow = 0 (t > 660 sec).⁹

The synergistic effects of VUV radiation, ion bombardment, and heating on 193 nm photoresist roughening and degradation was reported by Nest *et al.*²⁶ In their study, AFM measurements showed that limited surface roughness after UV/VUV only or ion only exposures at any temperature. However, simultaneous UV/VUV, ion bombardment, and heating to surface temperatures of 60-100 °C led to increased surface roughness, which was comparable to Ar plasma-exposed samples. As shown in Figure 5.2, ion bombardment resulted in pebbling of the surface and its roughness was only weakly dependent on temperature. Simultaneous ion + UV/VUV exposure was highly dependent on substrate temperature resulting in a very rough surface at 100 °C.²⁶

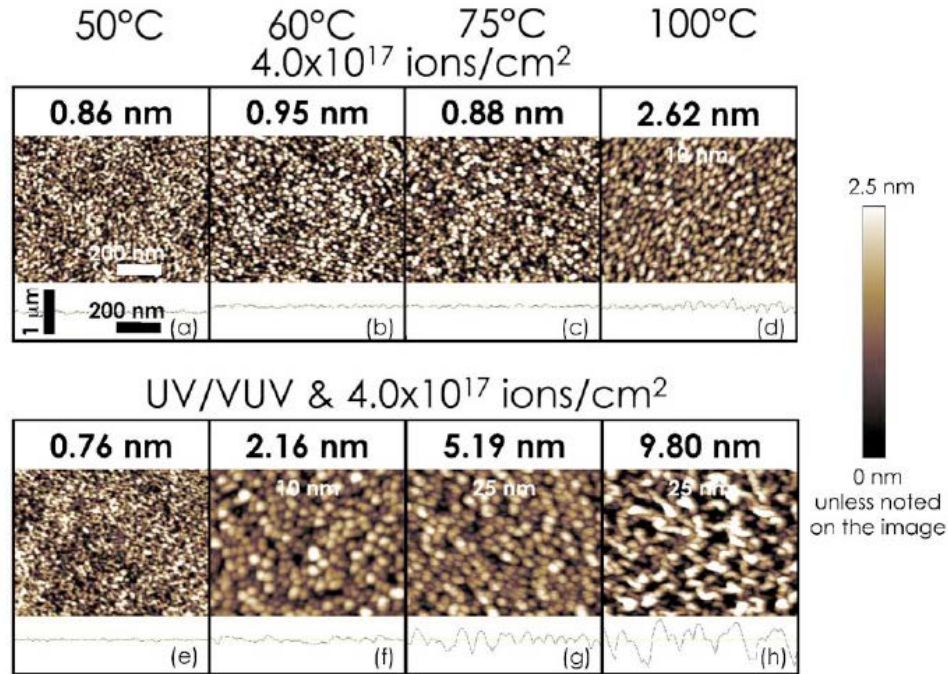


Figure 5.2: Surface roughness of the 193 nm photoresist after ion-only [(a)-(d)] and simultaneous ion + UV/VUV exposure [(e)-(h)] from 50 to 100 °C as observed with $1 \times 1 \mu\text{m}^2$ AFM images. Color scale is 2.5 nm. All line plots are on the same scale with a $5 \times$ exaggerated vertical axis.²⁶

Fukasawa *et al.* reported that the etching rate of $\text{SiN}_x\text{:H}$ film was enhanced by the simultaneous irradiation of radicals and UV photons, as shown in Figure 5.3.²⁴ In particular, higher energy photons with a wavelength above 115 nm (< 10.8 eV) caused a higher etching rate of $\text{SiN}_x\text{:H}$. In their study, it was also pointed out that irradiated radicals generated a reactive layer on the surface, which had a higher absorption coefficient in the UV region. The absorbed UV radiation in the reactive layer could enhance the surface reaction probability through the dissociation and/or rearrangement of chemical bonds.²⁴

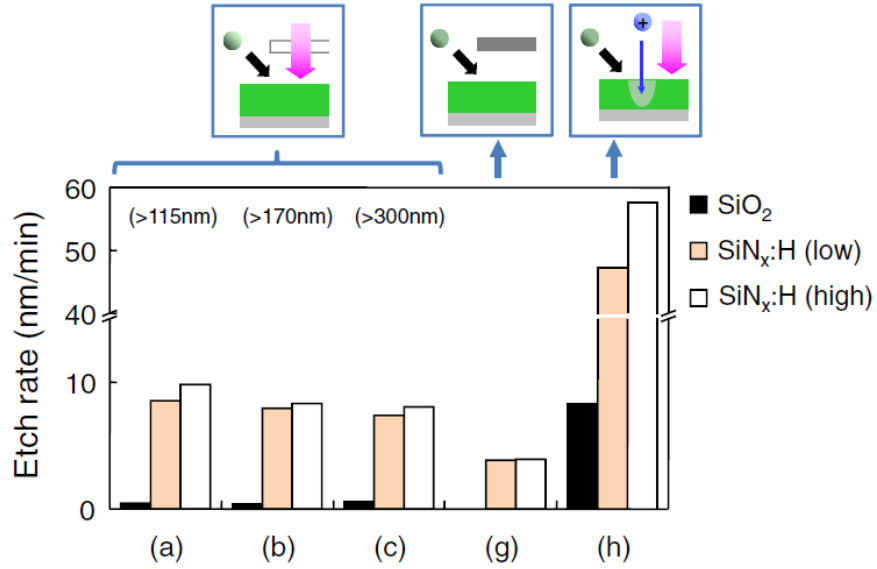


Figure 5.3: SiN_x:H and SiO₂ etch rates caused by the interaction between VUV/UV radiation and radicals under various pallet for plasma evaluation (PAPE) conditions: (a) VUV/UV radiation (> 115 nm) and radicals, (b) UV radiation (> 170 nm) and radicals, (c) UV radiation (> 300 nm) and radicals, (g) radicals, and (h) plasma exposure.²⁴

On the other hand, in 2017, Zecheng *et al.* reported that simultaneous irradiation of UV photons with wavelengths of 258 and 306 nm in Cl₂ plasma emissions resulted in suppression of surface roughness of GaN. This was ascribed to the reduction of the surface chemical reactions due to the synergetic effect between photons and radicals, which could otherwise lead to the rapid formation of etch pits or a rough surface.²⁸ Figure 5.4 shows the AFM images and line profiles of the GaN surfaces under different conditions.

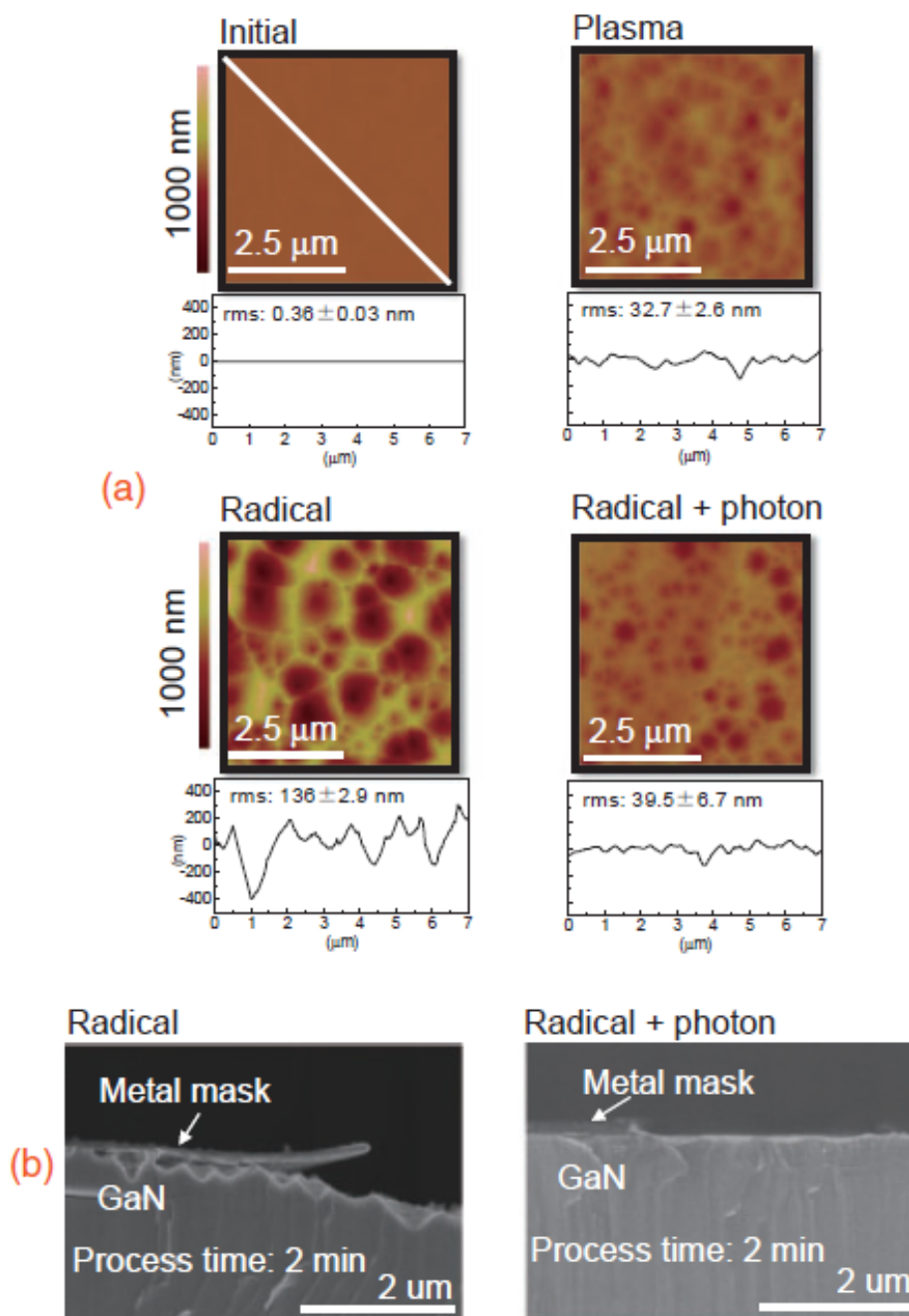


Figure 5.4: (a) AFM images and line profiles of the GaN surfaces in the initial state, after plasma etching, after radical exposure, and after simultaneous irradiation of photons and radicals. (b) Cross-sectional SEM images of the etch profiles of the GaN films after radical exposure and after simultaneous irradiation of photons and radicals.²⁸

A comprehensive and fundamental understanding on the reactions between species occurring at the atomic level is required to precisely control plasma etching.¹¹ Despite much progress, relatively little is known about the fundamental details of plasma-surface interactions due to the multitude and diversity of species in plasma as well as their deeply interconnected nature. One of the goals of this study is to explore possible synergistic effects (either positive or negative) between VUV photons and energetic ions for etching of Si in high-density, chlorine-containing plasmas.

5.2 Experimental details

Cl atoms etch undoped, p-type, moderately doped n-type Si (100), and polycrystalline Si (poly-Si) very slowly at room temperature ($< 10 \text{ \AA}/\text{min}$ at 10 mTorr) in the absence of ion bombardment.^{76,82-84} Heavily doped n-type Si (100) and poly-Si ($> 5 \times 10^{18} \text{ cm}^{-3}$) are etched spontaneously by Cl atoms at a much higher rate of up to $500 \text{ \AA}/\text{min}$ at a Cl pressure of 10 mTorr.^{76,82-84} The Cl_2 etching rate of Si (100) is very low at room temperature regardless of crystal structure and dopant level.⁸² Thus, in this study p-type Si samples or substrates were used to eliminate the spontaneous etching focusing on IAE and PAE.

Fast etching rates can deplete reactant concentration and produce a buildup of etching products in the plasma, even when high pumping speeds, low operating pressures, and high gas flow rates are employed.^{85,86} This is known as “loading effect”.⁸⁷ Etching products can decrease etchant species coverage on the etching surface, alter the gas-phase composition of ions, electrons and neutrals, and affect (usually lower) the electron temperature.^{86,88-90} Redeposition of etching products onto both the sample and the chamber

wall may also affect plasma species concentrations, and hence etching rates, uniformity, aspect ratio dependent etching, and etching profile.^{86,88,91-93} In this study, two different flow rates (total flow of 50 sccm for low flow rate and 250 sccm for high flow rate) were used to examine the flow rate dependence of the etching rate, and also to ensure that the experiments were done under conditions without serious loading effects. This 5X increase in the total flow rate at constant pressure led to a small increase in Cl neutral number density ($\text{Cl} + \text{Cl}_2$) and a large decrease in the SiCl_x etching product number density.

It should also be noted that laser interferometry measures the etching rate difference between the substrate and the mask material, when patterned sample are used. If their etching rates were the same, no interferogram would be observed. Therefore, etching rates of SiO_2 were also measured to evaluate the potential error of the etching rate measurements with laser interferometry.

The current through the substrate holder, resulting from positive ion impingement on the substrate, was obtained by monitoring the voltage drop across a $200\ \Omega$ resistor using a four-channel oscilloscope (Agilent DSO 7034B). The voltage on each side of the resistor was measured with respect to ground potential. Initially, a Pearson current probe was used to measure the current to the substrate holder, but the measured values showed an offset (Figure 5.5), so the Pearson probe method was abandoned. It is worth noting that the difference between the current with bias on and off is still meaningful, which equals to that measured by the voltage drop with the resistors.

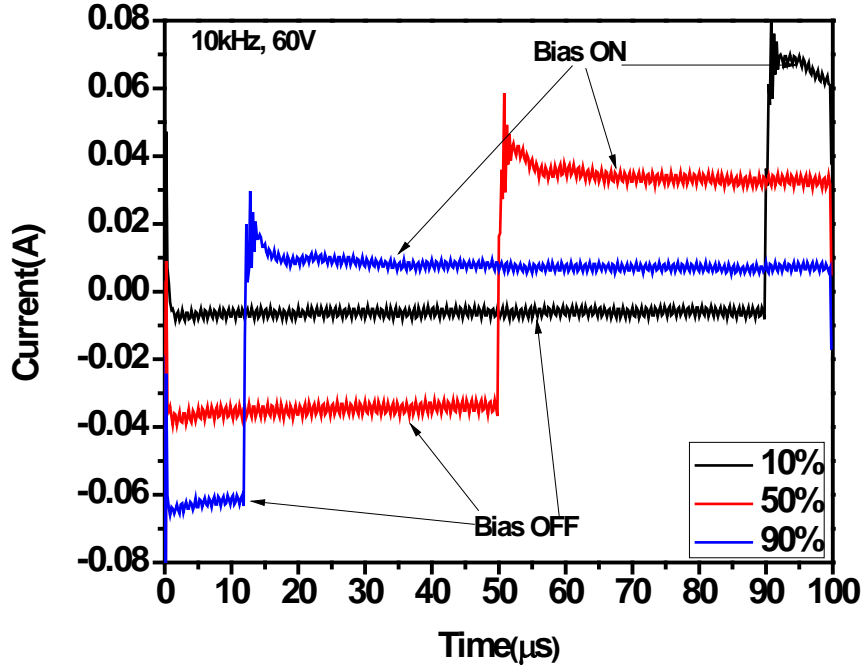


Figure 5.5: Substrate current measurements with Pearson current probe for 10 kHz, -60 V DC bias at 10%, 50%, and 90% duty cycle.

5.3 Results and discussion

5.3.1 Etching rate – ion energy dependence

Real time etching rates measured in 60 mTorr Cl_2/Ar plasmas are plotted as a function of the square root of ion energy. Either RF bias or pulsed negative DC bias with 50% duty cycle at a frequency of 10 kHz was applied to the sample stage during etching. Ion energy was taken as the difference between the plasma potential ($V_p \sim 5\text{V}$) and the applied negative DC bias or the self-bias when the stage was powered with RF. Etching rates under pure PAE conditions were measured with the sample stage grounded, so the ion energy was equal to V_p .

In the case of applying DC bias on the sample, at 60 mTorr, ions would suffer collision with probability, $P=1-\exp(-s/\lambda)$, of 7% and 17% while traversing the sheath at -30 V and -100 V bias, respectively, with corresponding sheath thickness (s) of $\sim 62\ \mu\text{m}$ and $\sim 154\ \mu\text{m}$ estimated based on the Child Law sheath model, and a mean free path (λ) of $\sim 830\ \mu\text{m}$ (more details in section A.1). Therefore, ion collisions in the sheath produced only a small broadening of the IED, preserving an essentially mono-energetic IED.

Etching rates of blanket SiO_2 films were also obtained by either laser interferometry (ion energy of $\sim 60\ \text{V}$ or $\sim 85\ \text{V}$) or spectroscopic ellipsometry (ion energy of $\sim 30\ \text{V}$ or $\sim 40\ \text{V}$) by measuring the film thickness change after five minutes of etching under pulsed negative DC bias at 10 kHz and 50% duty cycle (blue triangles) or RF bias (blue open triangles in Figure 5.6). Under pulsed DC bias, SiO_2 starts to etch slowly when the ion energy is $\sim 60\ \text{eV}$. The etching rate is $\sim 25\ \text{nm/min}$ at 60 eV and $\sim 40\ \text{nm/min}$ at 85 eV. The etching rate of SiO_2 under RF bias is much higher $\sim 650\ \text{nm/min}$ at 60 eV and $\sim 810\ \text{nm/min}$ at 85 eV. The significantly lower etching rate of SiO_2 under pulsed DC bias compared to that under RF bias is likely due to charging of the insulating SiO_2 mask. Since SiO_2 etching rates with pulsed DC bias are much lower than the Si etching rates (Figure 5.8 and Figure 5.10), SiO_2 etching has likely no contribution to the laser interferometry signal used to determine the silicon etching rates with DC bias. Under RF bias, however, the fast etching of SiO_2 is likely due to the very wide ion energy distribution caused by the thin sheath at this high plasma density. This SiO_2 etching would lead to a moderate underestimation of the Si etching rates, especially for higher ion energies.

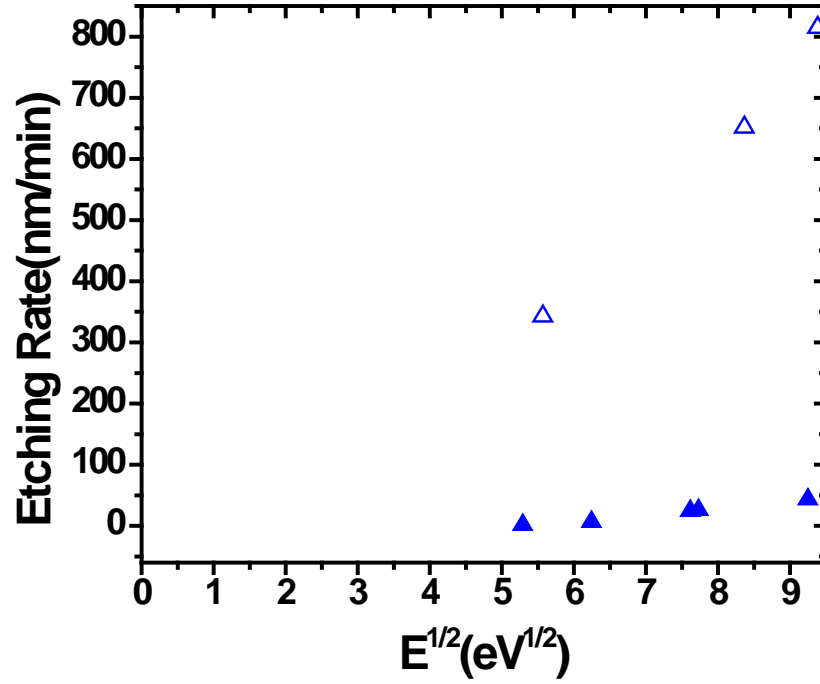


Figure 5.6: Absolute etching rates of SiO₂ as a function of $E^{1/2}$ (E = ion energy) for low flow rate under pulsed negative DC bias at 10 kHz with 50% duty cycle (blue triangles) or RF bias (blue open triangles).

Estimating an ion flux of $\sim 1.4 \times 10^{17} \text{ cm}^{-2} \cdot \text{s}^{-1}$ from the measured ion current density at the substrate (see below), the SiO₂ mask will charge up to $\sim 0 \text{ V}$ potential above $\sim 10\%$ duty cycle for -60 V pulsed DC bias (more details in section A.2). Ions may be deflected near the mask edge resulting in non-uniform etching across the bottom of the trench. Most of the trench bottoms were found to be flat after etching (left image in Figure 5.7), hence mask charging did not affect the measured Si etching rates. Etching under RF bias yielded vertical sidewalls (no taper), implying as expected, that charging was also not an issue under RF bias (right image in Figure 5.7).

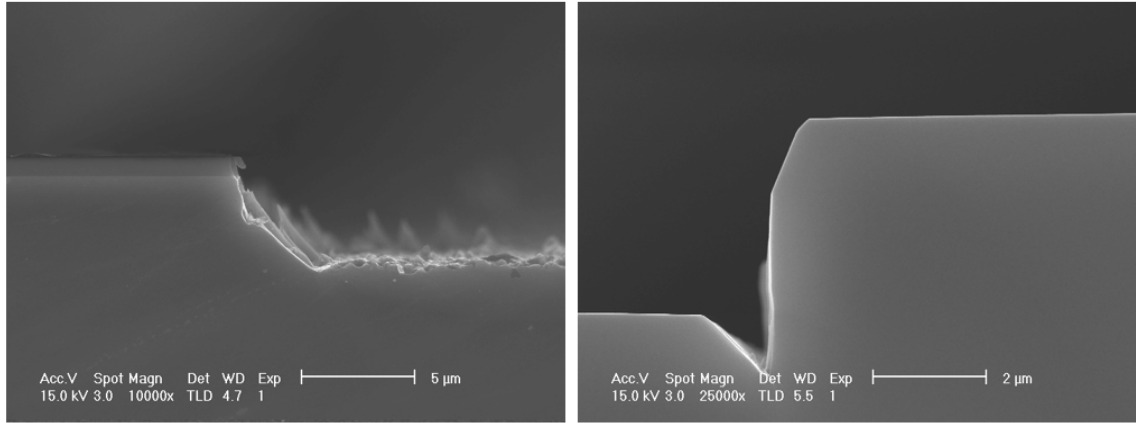


Figure 5.7: SEM images of patterned sample after etching with pulsed DC bias at 10 kHz and 50% duty cycle (left) and RF bias (right) -60V at high flow rate.

Real time etching rates measured by laser interferometry for p-Si in 60 mTorr Cl_2/Ar plasmas with SiO_2 masked patterned samples are plotted as a function of the square root of ion energy. The Si etching rates measured with RF bias (black squares for low flow rate and magenta stars for high flow rate in Figure 5.8) scale roughly with the square root of ion energy without showing a threshold. This is due to the bimodal ion energy distribution (IED) that occurs when the period of the applied RF bias is longer than the ion transit time through the sheath, resulting in ions responding to the changing sheath voltage.⁹⁴

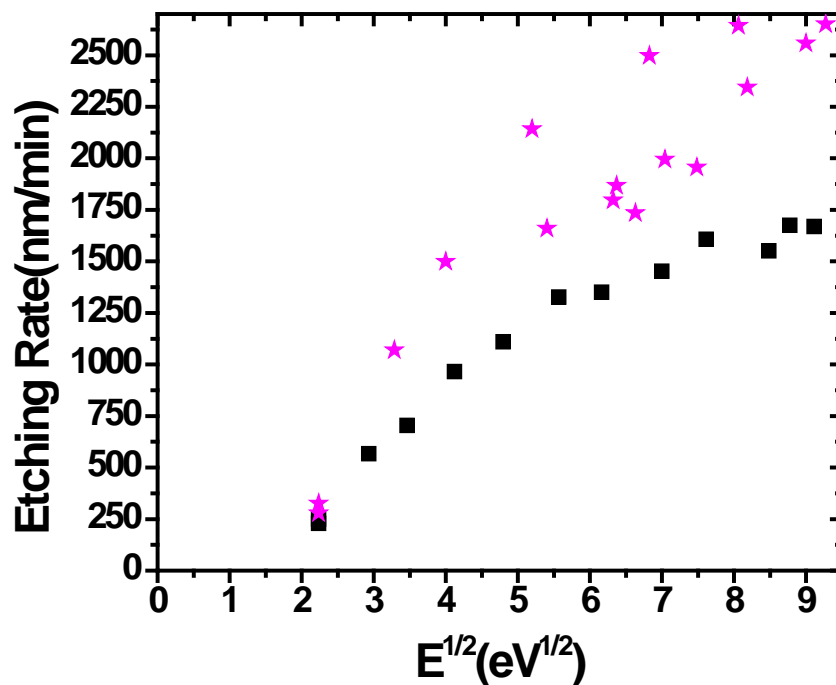


Figure 5.8: Absolute etching rates of p-Si as a function of $E^{1/2}$ (E = ion energy) with RF bias (black squares for low flow rate and magenta stars for high flow rate).

The peak separation of the Ar^+ bimodal IED reported by Hoekstra *et al.* in a low pressure (10 mtorr) Ar/Cl_2 ICP was ~ 50 eV, for a self-bias voltage of -31 V on the substrate under 13.56 MHz RF bias (shown in Figure 5.9).⁹⁵ The high energy ions in this broad IED would smear out the threshold that otherwise would appear at the low ion energy end. This shows a clear advantage offered by pulsed DC bias, which provides a better control of IED, and thereby a clearer separation between PAE and IAE. Of course, DC bias can be applied only when both the substrate holder and the sample are conductive.

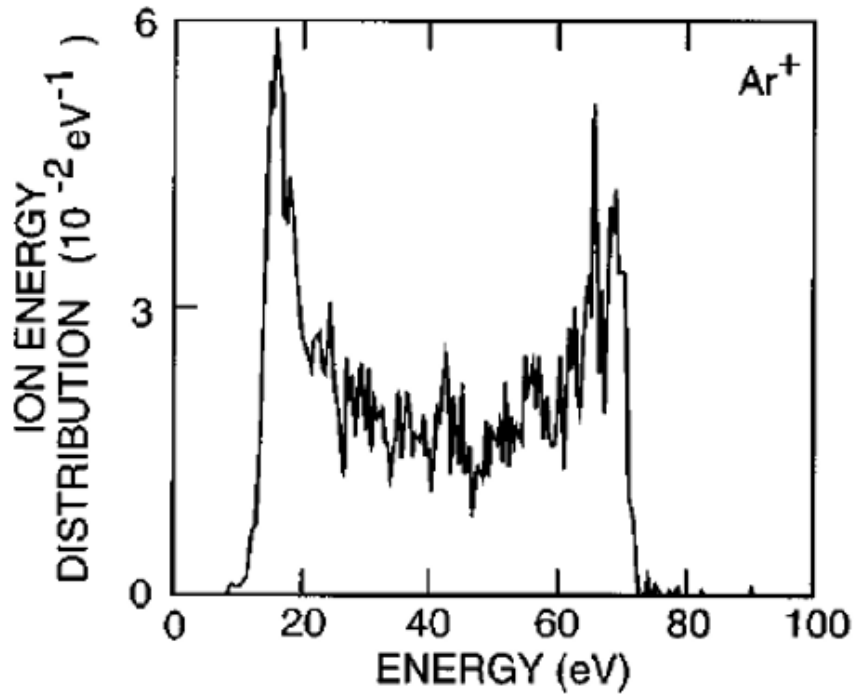


Figure 5.9: Ar^+ ion energy distribution averaged over the wafer for an ICP power deposition of 500 W, RF bias of 100 V, and -31 V calculated DC bias on the substrate reported by Hoekstra *et al.*⁹⁵

In contrast to the RF bias case, IAE threshold energies (~ 25 eV for the low flow rate and ~ 36 eV for the high flow rate experiments) are clearly seen when pulsed negative DC bias is applied to the sample stage (red dots for low flow rate and green dots for high flow rate in Figure 5.10). Below the threshold, etching is induced by VUV photons, and the etching rate under PAE condition (with sample stage grounded) is ~ 300 nm/min for low flow rate and ~ 400 nm/min for high flow rate. The lower PAE rate at low flow rate may be due to a “loading effect” that results in depleted Cl number density, relative to the higher flow rate. Assuming all of the Si exposed to the plasma (including the exposed edges of the underlying disc) is etching, and the product is SiCl_4 , only 1.6% of the Cl_2 feed gas is consumed at the high flow rate for an etching rate of 400 nm/min. Cl_2 consumption

would rise to 8.2% for the low flow rate at this etching rate (more details in section A.3). If the PAE rate scaled with Cl and Cl₂ number density, then the low flow rate PAE rate would drop no lower than 370 nm/min. The drop to the observed 300 nm/min at low flow rate indicates that additional changes with flow rate, such as a modest decrease in VUV intensity, are also occurring. At the highest ion energy investigated, the etching rate is about the same (~1,600 nm/min) at high and low Cl₂ flow rates, while the Cl₂ consumption is 7% and 32%, respectively. This trend is also not explained by the loading effect and suggests that IAE is limited by ion flux and not neutral flux. The estimated PAE yield for high flow rate and etching rate 400 nm/min is ~ 200 (more details in section A.7), and similar high yield (~ 100 for n-type Si) was also reported for photons with wavelength below 120 nm by Schwentner *et al.*,⁴¹ which could be due to photo-assisted hole-catalyzed reactions.⁹⁶

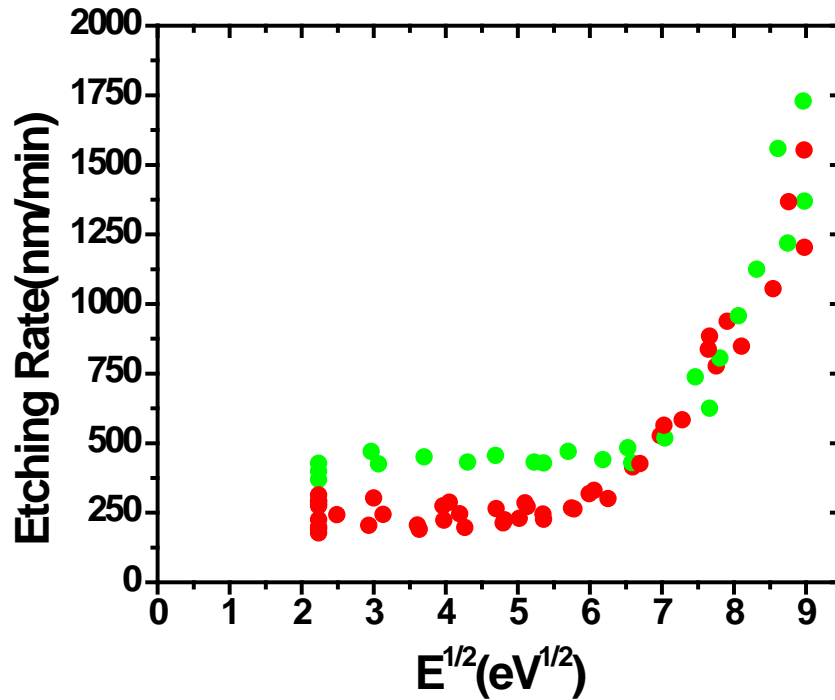


Figure 5.10: Absolute etching rates of p-Si as a function of $E^{1/2}$ (E = ion energy) with the application of pulsed negative DC bias at 10 kHz and 50% duty cycle (red dots for low flow rate and green dots for high flow rate).

Figure 5.10 also shows that, above the threshold, the etching rate under DC bias scales with $E^{1/2}$ as reported in other studies.^{46-48,97} Table 5.1 summarizes the threshold values of IAE of Si with chlorine. The reported thresholds range from 9 eV to 45 eV depending on conditions. The threshold energies observed in this work are consistent with some of the studies in Table 5.1, including our previous study¹⁸ under similar conditions. In the present study, considering the lower ionization potential of Cl vs Ar, the 9:1 flow rate ratio between Ar and Cl₂, and the expected high percent dissociation of Cl₂ at the high power density employed, the densities of Ar⁺ and Cl⁺ are likely roughly equal, with little Cl₂⁺, consistent with model predictions for somewhat different conditions.⁹⁸ The conditions in the present study most closely match those of Sawin and co-workers, who reported much lower thresholds of 16 eV or 10 eV with an Ar⁺ or a Cl⁺ ion beam and a Cl/Cl₂ neutral beam.^{46,47} The apparent discrepancy may be due to the way in which thresholds are defined, as illustrated in Figure 5.11. In the present study, the threshold corresponds to the ion energy, below which PAE occurs at a constant, appreciable rate. In the experiments of Sawin and co-workers, the threshold was determined from a linear extrapolation of the plot of etching rate vs. the square root of ion energy to zero etching rate. If PAE occurred in their experiment, this method would have led to a lower apparent threshold than those obtained in the present study.

Table 5.1: Threshold values of IAE of Si with chlorine reported in the literature.

Beam or Plasma	Species	Material	IAE Threshold	Ref.	other conditions
Beam	Ar ⁺ /Cl or Cl ₂	undoped poly-Si	16 eV	⁴⁶	6.2×10 ¹⁴ -1.2×10 ¹⁶ ions/cm ² /s for ion beam, 1.4×10 ¹⁶ -2.8×10 ¹⁷ atoms/cm ² /s for atom beam, sample T=40±5°C
Beam	Cl ⁺ /Cl or Cl ₂	undoped poly-Si	10 eV	⁴⁷	Ion flux 0.1-2mA/cm ² , IED 10 eV FWHM, 6.2×10 ¹⁴ -1.2×10 ¹⁶ ions/cm ² /s for ion beam, 1.4×10 ¹⁶ -2.8×10 ¹⁷ atoms/cm ² /s for atom beam, sample T=40±5°C
Beam	Cl ⁺ and Cl ₂ ⁺ /Cl or Cl ₂	Si	9 eV	⁹⁷	Plasma beam system with a mixture of Cl ₂ ⁺ (70%) and Cl ⁺ (30%) ions, neutral flux Cl ₂ (90%) and Cl (10%).
Beam	Cl ₂ ⁺ /Cl ₂	poly-Si	25 eV	⁴⁸	
Beam	Ar ⁺ /Cl ₂	poly-Si	45 eV	⁴⁸	
Beam	Ar ⁺ /Cl ₂	poly-Si	42 eV	⁹⁹	
Plasma	Ar and 1%-3% Cl ₂	p-Si	16 eV	¹⁷	Pulse Plasma with synchronous dc bias, 60mtorr
Plasma	50% Ar and 50% Cl ₂	p-Si	28 eV	¹⁸	CW plasma, 60mtorr
Plasma	90% Ar and 10% Cl ₂	p-Si	25 or 36 eV	This work	CW plasma, 60mtorr

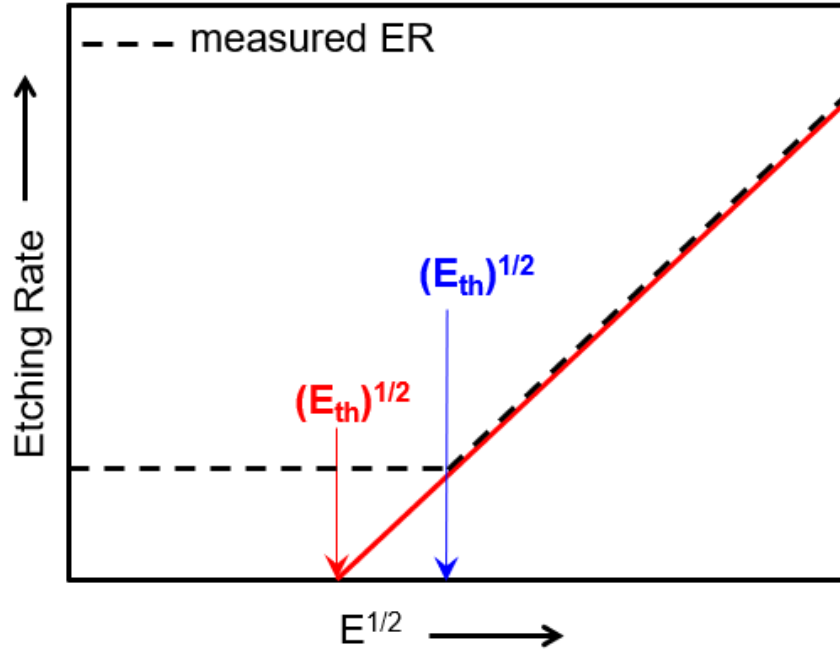


Figure 5.11: Definition of IAE threshold for this work (blue) and the study by Sawin and co-workers (red).

The IAE yield (number of Si atoms removed per incident ion) at high flow rate was calculated with the IAE rate (total etching rate minus PAE rate) under pulsed DC bias at 50% duty cycle and 10 kHz (shown in Figure 5.12). The estimated neutral-to-ion flux ratio under these conditions was ~ 30 and the energy-selected ion flux was $7 \times 10^{16} \text{ cm}^{-2}\text{s}^{-1}$. For 55 eV, 60 eV and 75 eV ion energy, the etching yield was found to be 0.25, 0.4 and 1.1, respectively (more details in section A.4). These yields are uncorrected for an apparent suppression of PAE by energetic ion bombardment, as addressed below and so the actual IAE yields can be up to twice these values at higher ion energies. Given these complexities, the yields found in this work are in reasonable agreement with the values reported by Chang *et al.*, which are 1.2 and 1.7 for 55 eV and 75 eV Cl^+/Cl , and 0.1 and 0.5 for 35 eV and 60 eV Ar^+/Cl .^{46,47}

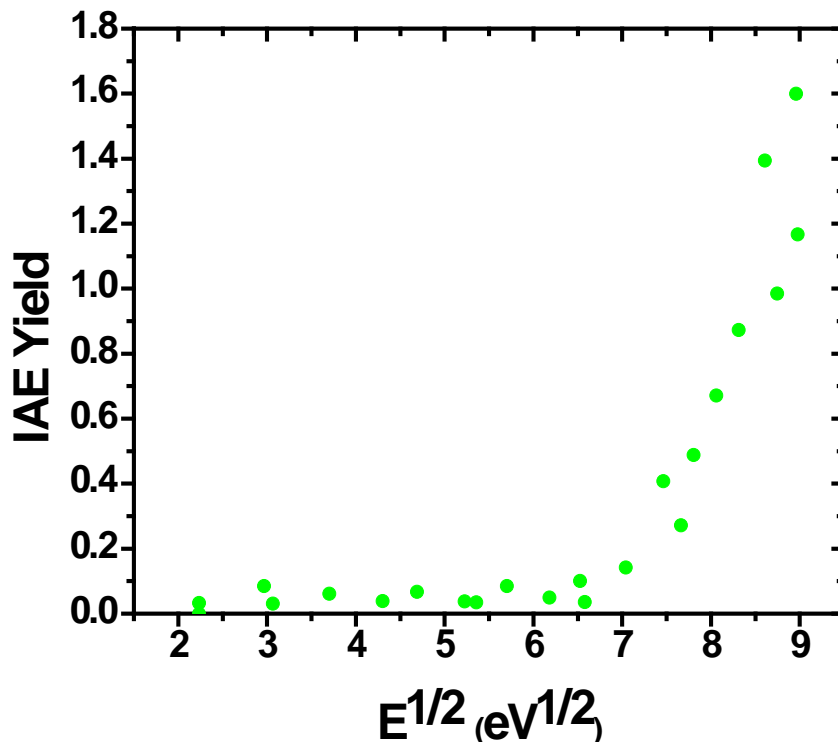


Figure 5.12: IAE yield of p-Si as a function of $E^{1/2}$ (E = ion energy) with the application of pulsed negative DC bias at 10 kHz and 50% duty cycle for high flow rate (derived from green dots in Figure 5.10).

5.3.2 Etching rate – duty cycle dependence

A central goal of this work was to explore the possibility of synergy between VUV photons and energetic ions, much like the well-known synergy between energetic ions and reactive neutrals in RIE.⁹ By employing a pulsed negative DC bias with variable duty cycle and relatively high frequency (10 kHz), the sample was subjected to etching stimulated by VUV photons only (when the DC bias was OFF), or the sum of VUV photons and energetic ions (when the DC bias was ON). Bias durations of between 0 and 90 μ s were used. In 90 μ s, only 0.0015 nm of Si (or about 1% of a monolayer) was etched away. This time is also fast compared to the gas average residence time in the reactor (\sim 0.1 s) or the time for

diffusion to the walls (~ 1 ms). Consequently, for a given duty cycle of the applied DC bias, the nature of the surface was the same (i.e., the same silicon chloride composition, sub-surface defect density, etc.), and the flux of neutral species to the surface was the same for the portion of the $100\ \mu\text{s}$ period when the bias was ON as it was for the remainder of the $100\ \mu\text{s}$ period when the bias was OFF. Therefore, by varying the bias duty cycle, the energetic ion flux averaged over many bias periods was conveniently varied while keeping the neutral flux and VUV photon flux constant. As addressed below, the surface nature and neutral flux could depend on duty cycle, however, as for example, in the case where the etching rate at high duty cycles becomes large enough to be limited by the supply of neutrals, causing chlorine coverage to fall-off.

If the total etching rate with the negative DC bias ON is simply the sum of IAE and PAE rates, then a linear variation of the etching rate as a function of the bias duty cycle is expected. Deviation above or below linearity could indicate positive or negative synergy, respectively, between above threshold energy ions and VUV photons. An etching rate that increases sub-linearly with increasing bias duty cycle could also simply be due to a transition into a neutral-starved regime, an explanation that is inconsistent with the flow rate behavior in Figure 5.10 and further discussed below.

Figure 5.13 presents measurements of the etching rate (black squares) and the integrated energetic ion current (blue line and open circles) vs. duty cycle of a 10 kHz - 60V DC bias. Making the PAE rate (the value at 0% duty cycle) the origin of the left y-axis, brings out the scaling of IAE rate (total etching rate minus PAE rate) vs. duty cycle.

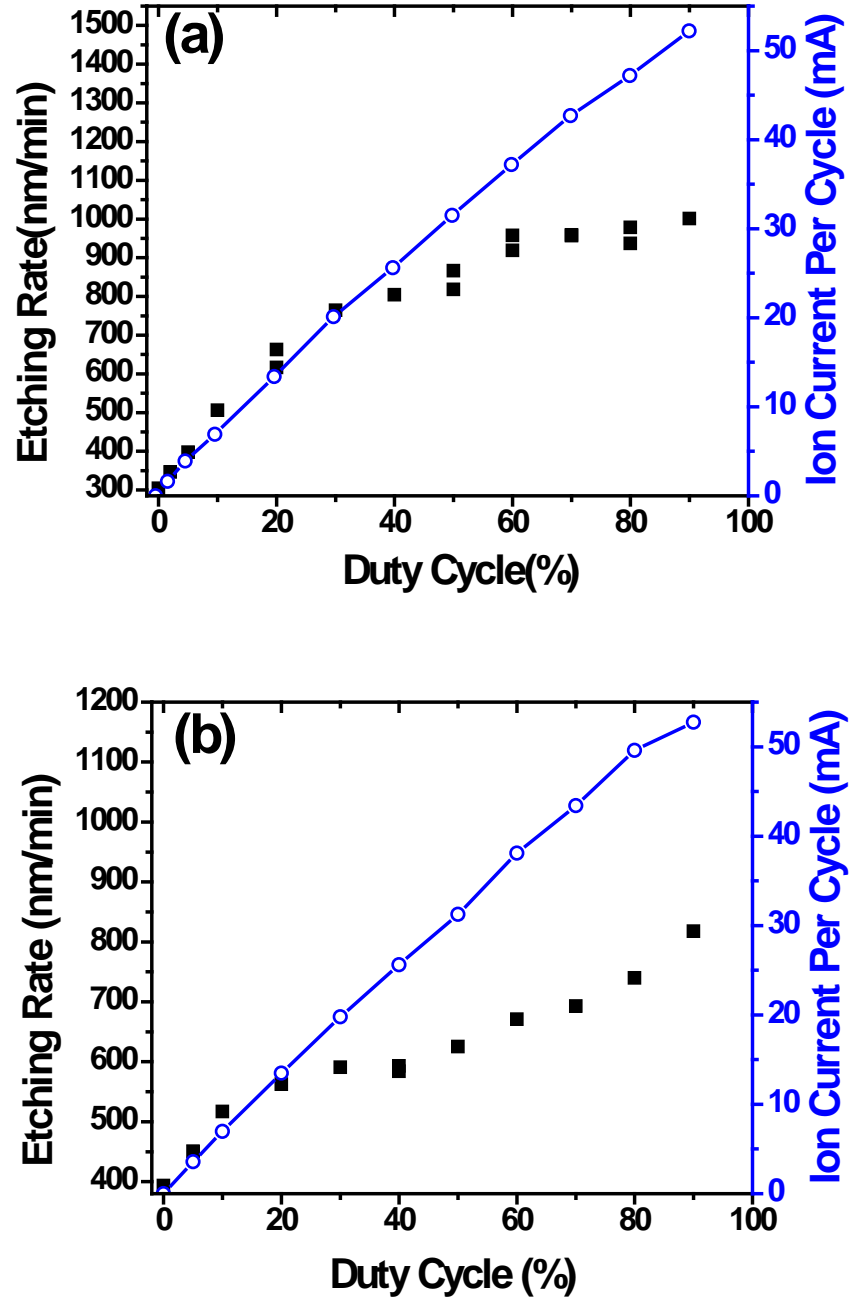
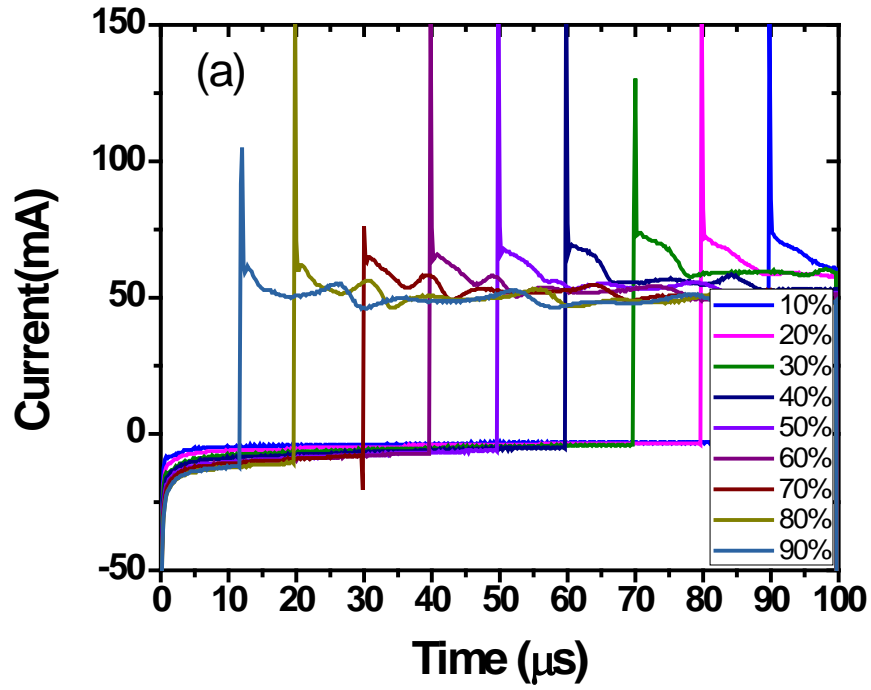


Figure 5.13: Total etching rate (both IAE and PAE) of p-Si as a function of duty cycle with -60 V pulsed DC bias at 10 kHz (black squares) for (a) low flow rate and (b) high flow rate. The PAE rate (0% duty cycle) was set as the origin on the left y-axis. The corresponding integrated energetic ion current per cycle is also shown (blue line and open circles).

The substrate ion current was obtained by measuring the voltage drop across a 200 Ω resistor using an oscilloscope, as shown in Figure 5.14. When negative DC bias is ON,

no electron current flows from the plasma to the substrate, and when bias is OFF, the electron and low energy ion currents balance, hence the detected net current is zero. The secondary electron emission coefficient reported by Qin *et al.* for Si is 0.74 for Ar^+ at 500 eV,¹⁰⁰ so with -60V bias, the effect of secondary electrons should be negligible. In any case, the secondary electron emission current will be proportional to the energetic ion current, so the trend of ion current vs. duty cycle will be valid even without correction for secondary electron emission.



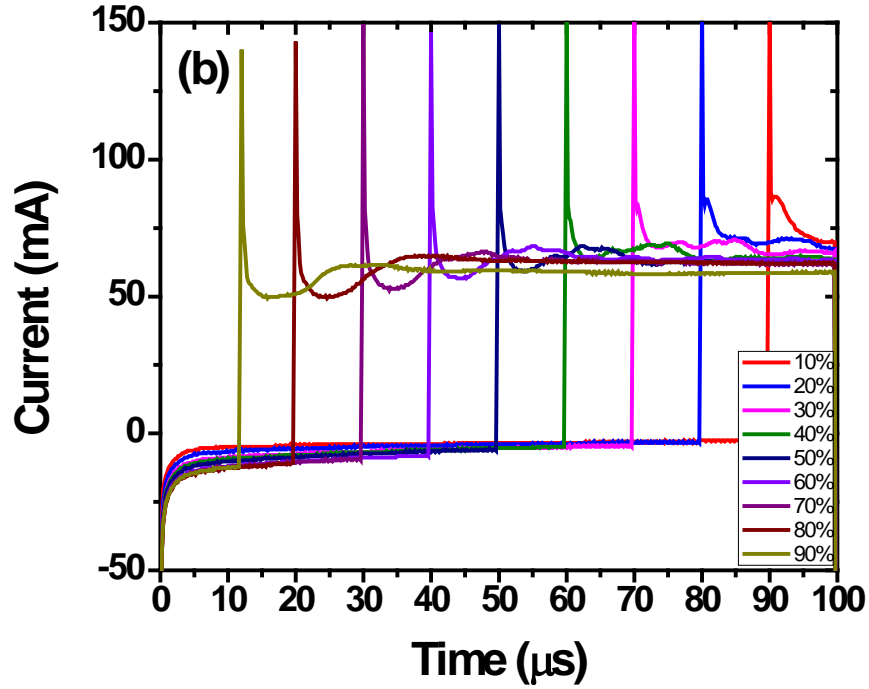


Figure 5.14: Time resolved energetic ion current measured on sample holder for a full period with the application of -60 V pulsed DC bias at 10 kHz (100 μ s per period) for (a) low flow rate and (b) high flow rate for duty cycle 10% - 90%.

As shown in Figure 5.13, the energetic ion current integrated over a full period of bias modulation increases nearly linearly with duty cycle, consequently the ion current to the surface was a nearly constant ~ 58 mA within a DC bias pulse (from an extrapolation of the currents in Figure 5.13 to 100% bias duty cycle). Given the 2.64 cm^2 area over which the current is collected, this corresponds to an ion flux of $1.4 \times 10^{17} \text{ cm}^{-2} \text{ s}^{-1}$. Note that this is the positive ion flux, regardless of the duty cycle. The *energetic* ion flux (an energy of the 5 V plasma potential plus the absolute value of the DC bias), averaged over many bias periods, is a nearly linearly increasing function of duty cycle, and is simply computed from the ion currents in Figure 5.13.

At low flow rate (Figure 5.13 (a)), the IAE rate increased linearly with increasing duty cycle (and therefore ion dose), up to about 30%. Above 30% duty cycle, the IAE rate became sublinear. This could be ascribed to several causes, including neutral-starved conditions and re-deposition of etching products. If either of these are the explanation, then a five-times higher Cl_2 flow rate should result in a deviation from linearity at higher duty cycle, or no deviation. The results in Figure 5.13 (b) show that the deviation from linearity starts at a *lower* ~20% duty cycle. This effect is attributed to a suppression of PAE by ion bombardment, as discussed below.

It should be noted that the etching rates in Figures 5.6, 5.8, 5.10, and 5.13 are higher than those typical of current manufacturing processes for Si etching in chlorine-containing plasmas, using commercial etching tools. These processes are carried out at lower power densities than in the present study, due mainly to the need for radial uniformity in etching rates. In addition, most of the required etching depths are not large and, therefore, very fast etching rates are not necessary. When very deep etching is required, SF_6 -containing plasmas are usually used. Though uncommon, it is possible to obtain fast etching rates approaching those in the present study. For example, Lane, *et al.* reported etching rates of 650 nm/min ($\sim 108 \text{ \AA/s}$ in Figure 5.15) for a 10 mTorr, 500 W (0.04 W/cm^3 , $n_e = 3 \times 10^{11} \text{ cm}^{-3} \approx \text{positive ion density}^{101}$) Cl_2 plasma in a Lam Research model 9400SE transformer-coupled plasma, with 150 W (0.85 W/cm^2) RF bias power on a chuck holding 150 mm diameter Si wafers.¹⁰² Given the higher volumetric power density (0.40 W/cm^3) and higher RF bias power density (2 W/cm^2) for the measurements in Figure 5.8, the ~3-fold higher etching rates in the present study are reasonable.

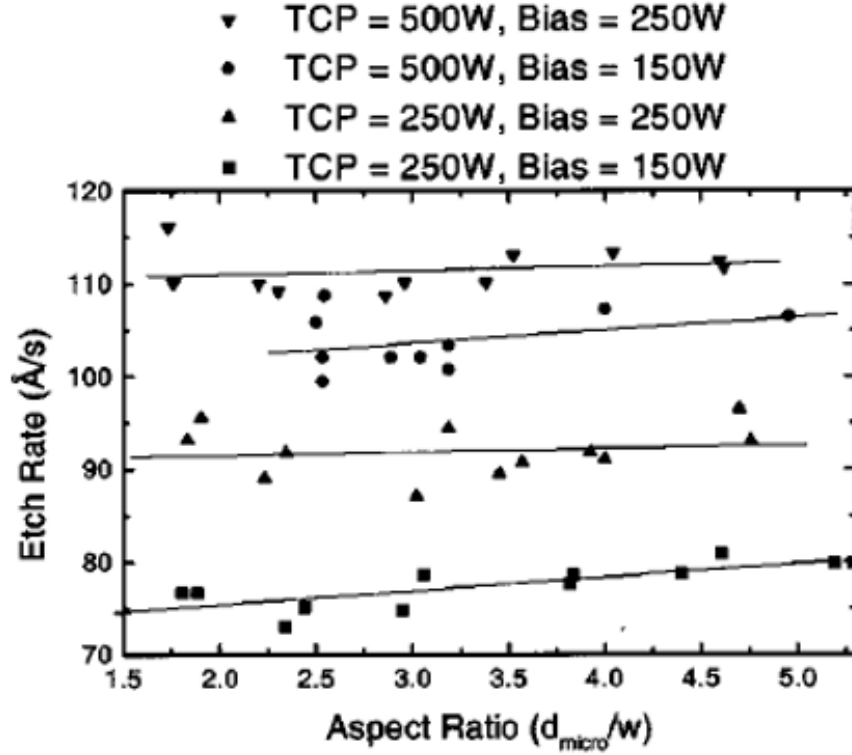


Figure 5.15: Etching rate vs aspect ratio at 10 mTorr by Lane *et al.* with Lam Research model 9400SE TCP.¹⁰²

The electron temperature (T_e) measured by a Langmuir probe for a continuously-powered, pure Ar plasma at 300 W and 50 mTorr in a similar setup was 2.0 eV (Figure 5.16).⁹⁴ The expected T_e for a Cl_2/Ar plasma is lower due to the lower ionization potential of Cl (12.96 eV) compared with Ar (15.8 eV). Assuming $T_e \sim 1.5$ eV in the present study and the ion mass ~ 40 amu for Cl^+ or Ar^+ , the calculated Bohm velocity is $u_B = 1.9 \times 10^5$ cm/s. Therefore, given the ion flux ($f_+ = 0.6 n_e u_B$) of $1.4 \times 10^{17} \text{ cm}^{-2} \text{ s}^{-1}$, the estimated plasma density is $7.0 \times 10^{11} \text{ cm}^{-3}$ at the sheath edge, and $1.2 \times 10^{12} \text{ cm}^{-3}$ in the bulk plasma (more details in section A.5). This plasma density is several times higher than in commercial processes, such as those noted above, again explaining the observed higher etching rates. Because a Faraday shield was required in the present study to obtain well defined ion

energy distributions, it was not possible to maintain a plasma at the low density required to slow the etching rate to a value more common in etching processes. Nonetheless, it is possible to apply our findings to these commercial processes by simple scaling of plasma density.

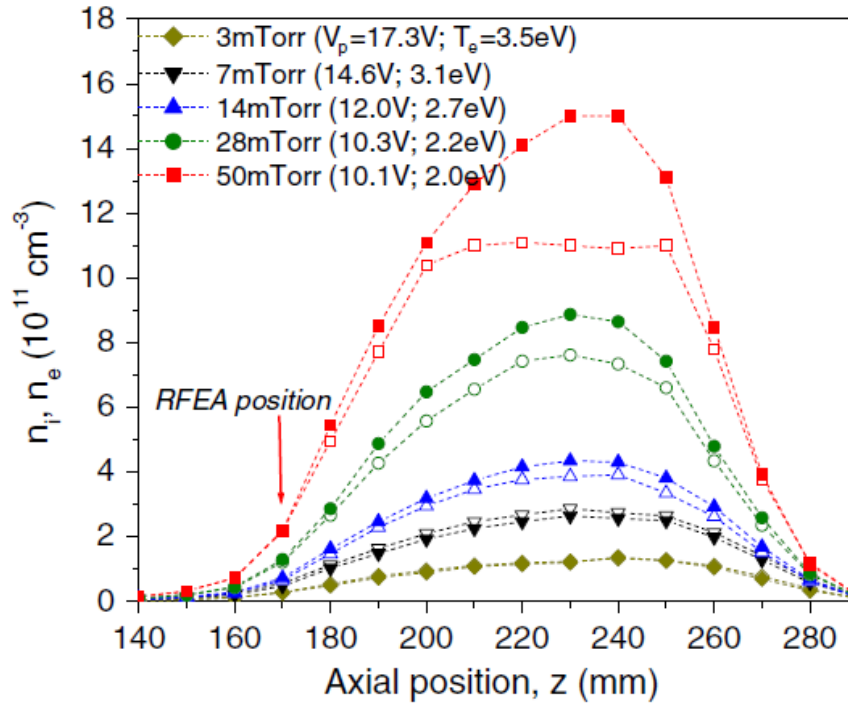


Figure 5.16: Ion (solid symbols) and electron (open symbols) density as a function of position and pressure measured by the Langmuir probe for CW plasma at 300 W and 40 sccm. The plasma potential and the electron temperature measured by the Langmuir probe at $Z = 170$ mm (location of RFEA) are shown in parentheses next to the corresponding pressure.⁹⁴

5.3.3 Mechanism

Assuming nearly complete dissociation of Cl_2 , and a gas temperature similar to a 6 mTorr Cl_2 plasma (600K)¹⁰³, at high flow rate (where little chlorine is present as SiCl_x), the Cl number density is $\sim 2 \times 10^{14} \text{ cm}^{-3}$, corresponding to a flux of $\sim 2 \times 10^{18} \text{ cm}^{-2}\text{s}^{-1}$ (more

details in section A.6). Therefore, when the DC bias is ON continuously, the Cl-to-ion flux ratio, f_{Cl}/f_+ , is ~ 15 , while for 5% duty cycle, f_{Cl}/f_+ , is ~ 240 . Here the ion flux was taken to be $1.4 \times 10^{17} \text{ cm}^{-2}\text{s}^{-1}$ as estimated above. Si yields derived from the data in Figure 5.13 (b) at high flow rate are presented in Figure 5.17. Given the small rate of consumption of Cl_2 at the maximum etching rate at high flow rate, these measurements are considered to represent a simpler case in which the ion flux (mainly a mix of Ar^+ and Cl^+) and neutral flux (mainly Cl , with little Cl_2 or SiCl_x) are better defined than at low flow rate.

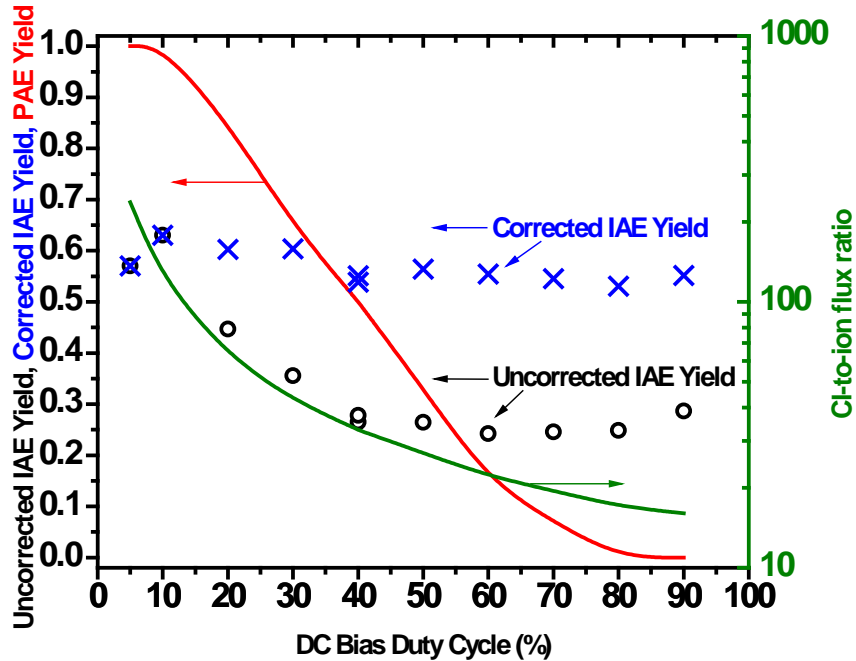


Figure 5.17: Etching yields as a function of pulsed DC bias duty cycle, derived from Figure 5.13 (b). The PAE relative yield (red line) was assumed to smoothly transition from 0 in the limit of zero Cl-to-ion flux ratio (f_{Cl}/f_+), to unity at high f_{Cl}/f_+ values. The corrected IAE yields (blue x's) account for a declining PAE rate as f_{Cl}/f_+ decreases with increasing bias duty cycle. Estimated f_{Cl}/f_+ values as a function of bias duty cycle are included (green line).

Computing the IAE yield from the observed (Figure 5.13 (b)) total etching rate minus the PAE rate, the latter in the absence of substrate bias, results in the open circles in Figure 5.17 (labeled uncorrected IAE yields). Shown in Figure 5.18 is the Si etching yield

at high flow rate as a function of the Cl-to-Cl⁺ flux ratio before and after correction. Etching yields increased from 0.29 to 0.36 to 0.60 as f_{Cl}/f_+ increased from 16 to 40 to 240. Chang and Sawin have reported Si etching yields of ~1.2, 2.5 and 3.1 at these Cl-to-Cl⁺ flux ratios for 75 eV ions.⁴⁷ When Ar⁺ was used instead of Cl⁺, Si yields of ~0.5, 1.0 and 1.8 were found at the same respective Cl-to-Ar⁺ flux ratios at an ion energy of 60 eV.⁴⁶ The yields in the present study are lower than the reported values, but the relative trend in yield vs neutral-to-ion flux ratio is in reasonable agreement with these prior studies. Furthermore, the etching rate in the present study at 90% duty cycle is about half that expected from a linear extrapolation of the 20% duty cycle value (Figure 5.13 (b)). As discussed above, ascribing this behavior to a too-low Cl-to-ion flux ratio is inconsistent with the flow rate dependence in Figure 5.13.

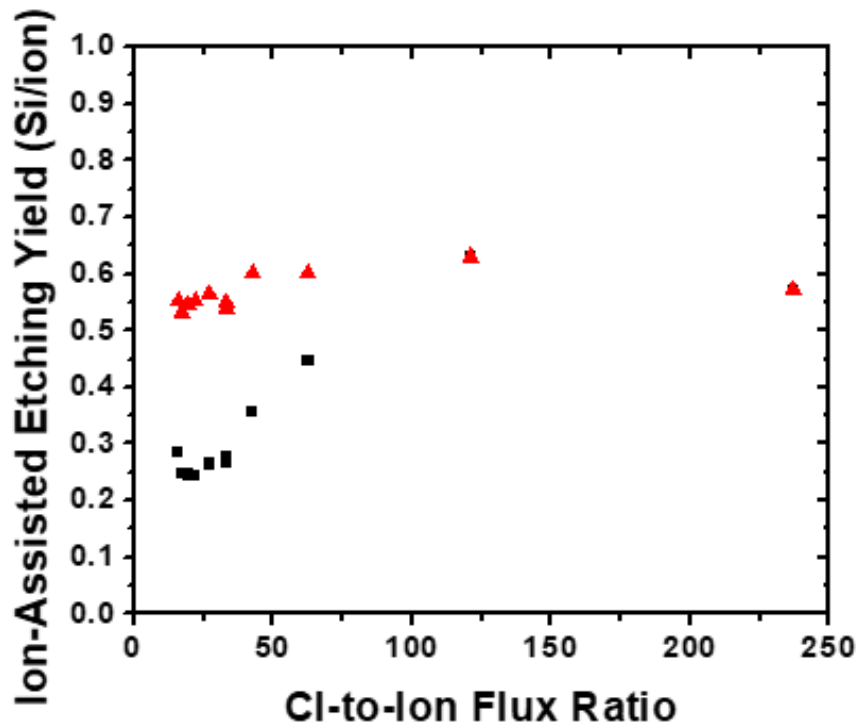


Figure 5.18: Uncorrected (black squares) and corrected (red triangles) Si etching yield at high flow rate as a function of Cl-to-Cl⁺ flux ratio derived from Figure 5.13 (b).

In addition, this explanation leads to a further inconsistency. The etching yield should be independent of ion flux and increase with the concentration of chlorine in the near surface region. Chang *et al.* found that the yield increased with increasing f_{Cl}/f_+ but was independent of ion flux for a given f_{Cl}/f_+ .^{46,47} They also attributed the increase and then saturation of the etching yield with increasing f_{Cl}/f_+ to the increasing chlorine coverage, but no measurements were made of chlorine coverage vs. f_{Cl}/f_+ . The XPS measurements in the present study, shown in Figure 4.15 conflict with this conclusion. Cl coverage increases by ~20% as f_{Cl}/f_+ decreases from ~300 (at a duty cycle of ~3%) to 15 (at a duty cycle of 100% i.e., CW). This would lead to the unreasonable conclusion that the IAE yield decreases as chlorine coverage increases, and furthermore the yield when most surface chlorine is in the form of $SiCl_2$ and $SiCl_3$ is *lower* than when chlorine is present solely as $SiCl$.

We therefore conclude that the IAE yield should be nearly independent of f_{Cl}/f_+ for the conditions in the present study. The only way this is possible, is if ion bombardment suppresses the PAE process. In the limit of very high f_{Cl}/f_+ (i.e., for small DC bias duty cycles), there is no suppression and the relative PAE yield (normalized to the value at zero duty cycle) is unity. At the opposite limit of low f_{Cl}/f_+ at high DC bias duty cycles, a nearly complete suppression could occur, in which case the PAE yield is close to zero. The red curve in Figure 5.17 represents the relative PAE yield with these limits and an intermediate regime that will produce a f_{Cl}/f_+ -independent IAE yield when the modified PAE etching rate is subtracted from the total etching rate to obtain the IAE yield as a function of f_{Cl}/f_+ . These corrected IAE yields are given as the ✕'s in Figure 5.17.

A possible mechanism leading to this conclusion could be that ion bombardment suppresses PAE by disrupting the silicon lattice, introducing electron-hole (e-h) Shockley-Read-Hall recombination centers. This occurs above a certain (critical) ion dose requiring a minimum duty cycle of the applied DC bias. The end result is a reduction in the concentration of carriers available for chemical reaction on the surface, and hence a lower PAE rate, pointing to anti-synergism between above threshold-energy ions and VUV photons.

To further support this mechanism, the dependence of the total etching rate on the period of the pulsed negative DC bias was examined with 50% duty cycle at high flow rate (Figure 5.19). The ion flux, neutral flux, and VUV photon flux are all constant and independent of pulsing period. If there is no synergism (positive or negative), then PAE and IAE are two completely independent processes, and the total etching rate is the sum of the IAE rate during half the period and the PAE rate over the full period. Hence the total etching rate should be independent of bias pulsing period. Instead, the etching rate decreases as the bias period increases. At very short bias periods, the PAE rate must be constant during the period, since the time is too short to alter the state of the surface or degree of damage. From the data in Figure 5.19, this condition corresponds to the removal of only about 0.01 to 0.007 monolayers at high (etching rate ~2400 nm/min) or low (etching rate ~1100 nm/min) bias voltage. As the pulsing period increases, the increasing energetic ion dose per cycle causes an increase in the degree of damage of the surface, leading to a suppression of PAE and a decrease in the total etching rate, as is observed in the measurements in Figure 5.19, consistent with the proposed negative synergism between energetic ions and VUV photons.

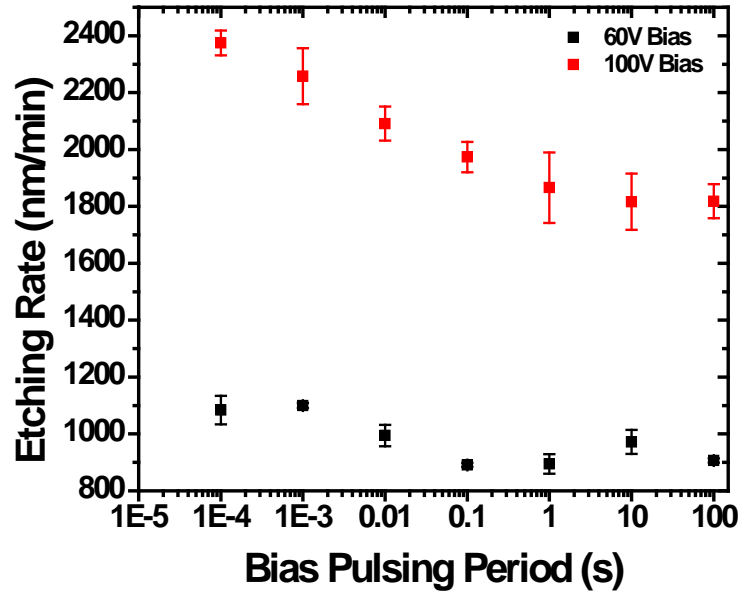


Figure 5.19: Total etching rate (sum of IAE and PAE) as a function of pulsed DC bias period with 50% duty cycle, and for negative bias voltage of 60V (black) and 100V (red), at high flow rate.

Finally, the higher etching rate at high bias duty cycles found at low flow rate (Figure 5.13 (a)), compared to that at high flow rate (Figure 5.13 (b)), neither supports nor rules out the anti-synergy between ions and photons suggested by the other results in this study. It appears that ion bombardment at the low flow rate behaves differently than that at the high flow rate. At low flow rate, the 1000 nm/min etching rate at 90% duty cycle depletes ~20% of the Cl_2 feed gas, while at high flow rate, the 800 nm/min etching rate at 90% duty cycle consumes only 3%. At high flow rate, the ions bombarding the Si substrate are expected to be Ar^+ and Cl^+ . At low flow rate, SiCl_x^+ is likely to become important, since the electron impact ionization rate constants (k_x) favor SiCl_x molecular ion formation near $T_e = 1.5$ eV ($k_{\text{Ar}} : k_{\text{Cl}} : k_{\text{Cl}_2} : k_{\text{SiCl}_4} : k_{\text{SiCl}_2} : k_{\text{SiCl}_3} : k_{\text{SiCl}} = 1.0 : 7 : 20 : 60 : 150 : 205 : 980$) (more details in section A.8).^{86,104-106} Energetic molecular ions will fragment into atoms

upon impact,¹⁰⁷ leading to a reduction of the energy per atom and hence less sub-surface penetration. This could reduce the suppression of PAE at the low flow rate, and cause an increase in the total etching rate, and a fall-off from linearity at higher bias duty cycles, provided that the IAE rate does not drop off correspondingly.

Photo-generated carriers in the bulk of semiconductors could recombine via three mechanisms (Figure 5.20). Radiative recombination emits a photon with energy corresponding to the bandgap energy, when an electron spontaneously falls from the conduction band to the valence band in direct bandgap semiconductors.¹⁰⁸ Auger recombination involves interaction among three carriers with a second electron or hole excited by absorbing the energy released in the recombination process. The energy eventually dissipates through a series of collisions in the lattice.¹⁰⁹ SRH recombination occurs when a structural defect or material impurity creates a localized trap state within the bandgap that facilitates carrier recombination without emitting photons. Electrons and holes trapped in these states could recombine and release energy to the lattice in form of phonons.^{110,111} In this process, an electron is trapped in the mid gap state and then recombines with a hole, or vice versa.

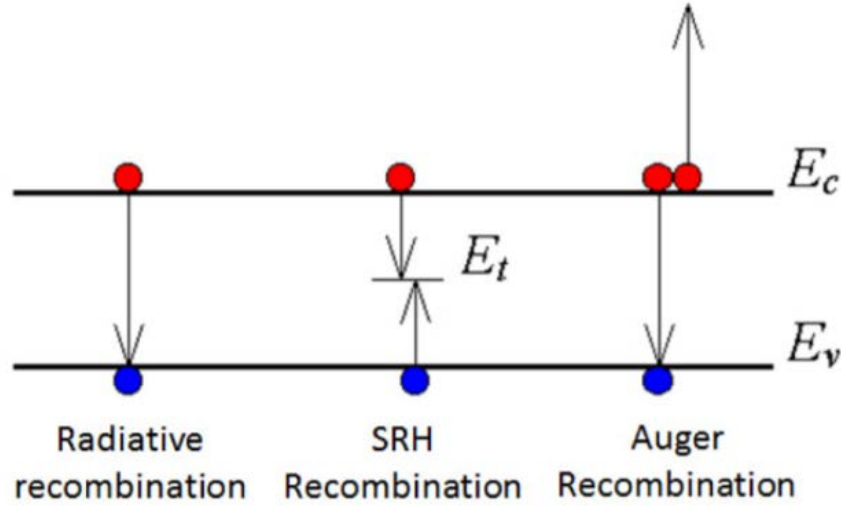


Figure 5.20: Three types of carrier recombination mechanisms in semiconductors.¹¹⁰

The plasma-generated photons striking the Si substrate will be absorbed near the surface, generating electron hole pairs. The minority carrier (i.e., electron for p-type Si) could diffuse to the surface, react with the chlorinated surface layer, and induce etching before being lost due to SRH recombination. The most striking aspect of this study is the high PAE yield and the large enhancement in PAE at short VUV wavelengths (90% of the total PAE rate was caused by radiation at wavelengths $< 120 \text{ nm}^{18}$). Higher etching yields for VUV versus visible radiation could be due to hot or energetic carriers created by photon energies well above the bandgap energy. These hot photo-electrons, possessing sufficient energy, could have a higher probability of avoiding being trapped by the mid-gap states and recombining with holes at defect sites via SRH mechanism, thereby preserving a higher concentration of carriers and a higher PAE rate. Wu *et al.* reported that the electron capture cross section of the gold donor state and the hole capture cross section of the gold acceptor state showed T^{-2} and $T^{-1.3}$ dependence for n-type Si (Figure 5.21).¹¹² With numerical

modeling, Fardi *et al.* showed that hot electrons led to an increase in short circuit current in quantum well $\text{Al}_x\text{Ga}_{1-x}\text{As}/\text{GaAs}$ p-i-n photodiodes, which was due to hot carriers with long energy relaxation lifetime escaping from the quantum wells without significant SRH recombination.¹¹³ An intuitive explanation for this negative temperature or energy dependence of the SRH recombination rate could be that hot electrons and holes with excess kinetic energy, generated by ~ 10 eV VUV photons, “bounce off” mid-gap traps (either unoccupied, or occupied with the opposite charge carrier) and hence have a lower recombination rate. This would at least partly explain why VUV photons are so much more efficient than visible or UV photons for etching Si in the presence of chlorine.

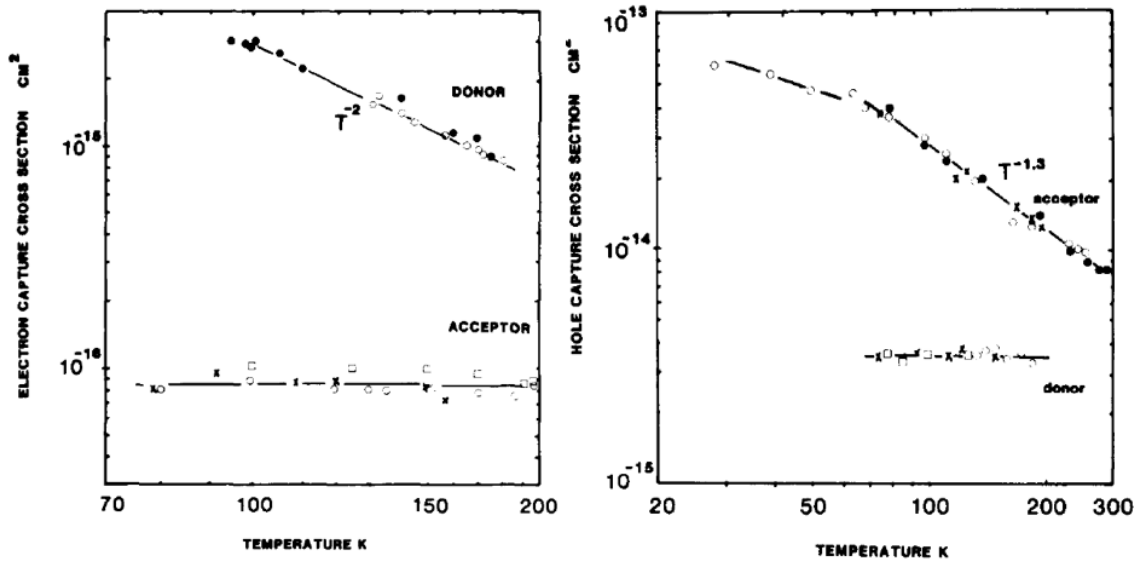


Figure 5.21: Electron capture cross sections of the gold donor and acceptor (left) and hole capture cross sections of the gold donor and acceptor (right) as a function of temperature. The symbols represent different samples.¹¹²

Chapter 6 – Summary, Conclusions, and Future Directions

6.1 Summary and conclusions

In this work, p-type Si etching was studied in a radio frequency (RF) high density, inductively coupled plasma, with Cl₂(10%)/Ar(90%) mixed gas feed at 60 mTorr. A Faraday shield was used to prevent capacitive coupling to the plasma so that the ion energy could be precisely controlled especially on the low energy end, due to a very low plasma potential (~5 V).^{17,18} Real time etching rates were measured *in-situ* by laser interferometry for both photo-assisted etching with the sample on a grounded substrate stage, and ion-assisted etching with either RF or pulsed negative DC bias applied to the substrate stage. The Si surface chemical composition after etching was determined by vacuum-transfer XPS and PAE was compared to IAE. Possible synergy between VUV photons and energetic (above threshold-energy) ion bombardment was investigated by varying the duty cycle and period of the pulsed negative DC bias applied to the substrate stage.

Etching rates under pulsed negative DC bias (with a pulsing frequency of 10 kHz and 50% duty cycle) showed an IAE threshold of ~ 25 eV for low chlorine flow rate and ~36 eV for high chlorine flow rate. The sub-threshold PAE etching rate was ~ 300 nm/min for low flow rate and ~ 400 nm/min for high flow rate. Above threshold, the etching rate scaled linearly with $E^{1/2}$, where E = ion energy. Etching rates measured with RF bias did not show an energy threshold due to a wide (bimodal) ion energy distribution (IED).

XPS measurements showed excellent agreement of the relative chlorine concentration determined using low resolution survey spectra, high resolution Si(2p) spectra, and the corresponding deconvoluted spectra. Importantly, under PAE conditions

(with VUV photons and only sub-threshold ions bombarding the surface), the chlorine content was significantly lower, compared to that under IAE conditions, and the chlorinated surface layer contained only SiCl. Under IAE conditions (with both VUV photons and above threshold-energy ions bombarding the surface), the chlorinated layer contained silicon dangling bonds (Si•), SiCl₂, and SiCl₃ in addition to SiCl, with relative abundance of SiCl>SiCl₂>SiCl₃. The missing higher chlorides and Si dangling bonds under PAE suggested that, in contrast to VUV photons, energetic ions are more capable of disrupting multiple Si-Si bonds, promoting reactions between Si and adsorbed chlorine leading to higher chlorides. Under IAE conditions, the relative chlorine concentration increased with increasing bias voltage on the substrate stage, as the thickness of the reactive chlorinated layer also increased.

The IAE rate and the energetic ion dose per cycle (with pulsed negative DC bias applied on the sample stage) were closely correlated, increasing linearly with duty cycle, but only at low duty cycles. Above a certain duty cycle (30% for low flow rate and 20% for high flow rate), as duty cycle increased, the IAE rate fell below the straight line and the IAE apparent yield decreased with increasing chlorine coverage on the surface. This unreasonable trend of IAE yield indicated that the assumption of PAE rate being constant with increasing duty cycle is not valid and suggested the existence of negative synergy (anti-synergism) between VUV photons and energetic ion bombardment, when surface damage reaches a certain (critical) value. This anti-synergism was further supported by the observed drop of total etching rate with increasing period of the pulsed DC bias. The underlying mechanism could be that ion bombardment creates Si lattice defects, which act

as Shockley-Read-Hall recombination centers for photoelectrons and holes, lowering their respective concentration on the surface, thereby restricting PAE.

6.2 Future work

6.2.1 Plasmonics

While studying etching of patterned silicon wafers in chlorine-containing plasmas under conditions of PAE, we observed the formation of intriguing features, where the etching rate was much higher at the bottom corners of the initially rectangular trenches (Figure 2.18). The formation of these nanotrenches could be due to surface plasmons.

Surface plasmons are electromagnetic waves that propagate along the interface of a conductor (usually metal) and a dielectric (the dielectric can be air or vacuum). Surface plasmons are collective oscillations of free electrons in the conductor, in resonance with an exciting light wave.¹¹⁴ While surface plasmons propagate along the interface, the field perpendicular to the interface decays exponentially with distance into the metal (evanescent wave). In addition, the field attenuates in the propagation direction, due to losses arising from absorption in the metal. Surface plasmons have been exploited to concentrate photon energy into nanoscale volumes in sub-wavelength features (e.g., holes, trenches) or to enhance transmission of light through holes in metal films. Sub-wavelength refers to the situations in which the feature size is smaller than the wavelength of light.

Figure 6.1 shows that the light intensity at the corners of the trench has its maximum value, which is significantly larger than that at the central area.¹¹⁵ Such intensity maxima might be responsible for the greatly enhanced PAE forming the nanotrenches observed in

Figure 2.18. As the nanotrench becomes deeper, the freshly exposed silicon sidewall acts as a conductor for further plasmon propagation to the bottom of the feature, leading to a much higher etching rate compared to that of the middle area of the trench.

The cavity width (W) and especially the height (H) are of paramount importance. In fact, for a given value of W and wavelength, the light wave will couple into surface plasmons more efficiently for specific values of H.¹¹⁶

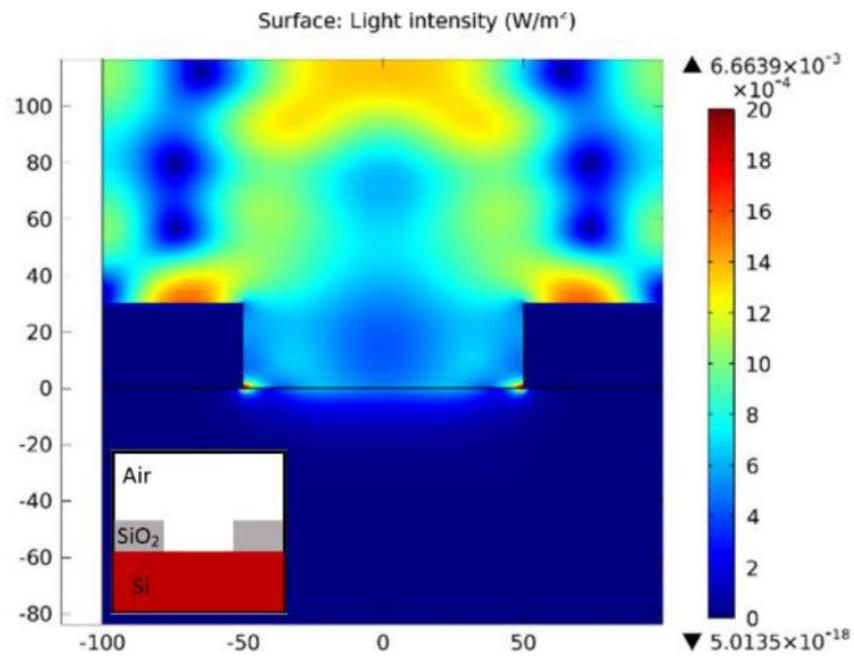


Figure 6.1: Simulation of light intensity (W/m²) for a planewave ($\lambda=106.7$ nm, 1V/m) normally incident onto a 30 nm-thick SiO₂ mask with L/S=100nm, on top of Si. Strong light intensity is observed at the trench corners.¹¹⁵

While surface plasmonics may be an exciting new discovery in plasma etching, there is, however, a mundane explanation for the profiles observed in Figure 2.18. It is well known that glancing incidence ion specular reflection off etching feature sidewalls causes an enhanced ion flux at the sidewall-surface boundary. The resulting microtrenches formed

in standard etching processes at high bias energies are only moderately deeper than the majority of the trench (unlike the several-fold deeper nanotrenches in Figure 2.18), and furthermore, in the absence of bias, the ion energy is very low. It is possible that such low energy ions (as well as specularly reflected VUV photons) could aid the removal of a native oxide and lead to fast PAE near the sidewalls before the oxide clears over most of the trench width. To rule out this possibility, etch profiles for the exact conditions used to produce the sample shown in Figure 2.18 can be recorded for different times, with or without a very brief initial bias to remove all native oxide.

If this simple explanation is ruled out, then further experiments may be conducted whereby the depth of etching of a nanohole is measured (using cross sectional SEM imaging) as a function of etching time. The etching rate should be non-linear. When the depth of the hole H is just right, so that a surface plasmon can be launched efficiently, etching will proceed at relatively higher rate. When there is no surface plasmon, etching will be much slower. Plasmons from adjacent features can even interact with one another.¹¹⁷ This would result in very different etching rates in areas of densely packed features compared to open areas.

6.2.2 Turning off PAE

Future processes will require atomic-layer precision of etched depths, and extremely high selectivity with respect to different materials. This in turn will require the use of very low energy (10s of eV) ions. The emergence of PAE at such low ion energies can greatly complicate the design of etching processes with atomic precision. Therefore, it is worthwhile to develop methodologies for turning PAE off.

One option is to add a small percentage of O_2 to the plasma. O_2 oxidizes the surface and alters the surface condition. If the oxide film is thick enough, sub-threshold etching will be blocked, choking PAE. With oxygen added, the silicon etching rate will depend on the rate of oxide growth and the rate of oxide removal via sputtering by energetic ions. The minimal amount of O_2 needed to stop PAE, while maintaining a reasonably high Si IAE rate, can be found. Then, the dependence of etching rate on ion energy, at the presence of the minimal oxygen concentration that chokes PAE, can be established and compared to the case without oxygen addition.

Another option is to set the sample downstream of the plasma, where the VUV photon density is expected to be considerably lower. One can change the distance between plasma and sample by moving the ICP coil at different positions along the reactor axis. With the sample immersed in the plasma, the photon flux on the sample surface will be relatively high, resulting in high PAE rate. On the other hand, when the sample is placed some distance away from the plasma, the photon flux on the sample surface will be relatively low, due to radiation trapping. VUV photons are emitted as a result of resonant electronic transitions from a high energy state to the ground state. Such photons have just the right energy to induce the opposite transition, i.e., excite a ground state atom to a high energy state. Thus, the photon can be easily reabsorbed by ground state atoms. The process of emission, absorption, and re-emission continues many times before the photon finally escapes. This process is referred to as “radiation trapping”.¹¹⁸ If photons are efficiently trapped and very few photons make it to the sample surface, then PAE will be negligible.

References

- ¹ F. F. Chen, in *Introduction to Plasma Physics and Controlled Fusion; Vol. 1*, Second ed. (1984).
- ² Y. Horiike, N. Hayasaka, M. Sekine, T. Arikado, M. Nakase, and H. Okano, *Appl. Phys. a-Mater.* **44**, 313 (1987).
- ³ C. P. Huang and Y. Y. Zhu, *Act. Passiv. Electron. Compon.* **2007**, 1 (2007).
- ⁴ V. M. Donnelly and A. Kornblit, *J. Vac. Sci. Technol. A* **31** (2013).
- ⁵ MIT Open CourseWare. ocw.mit.edu/courses/electrical-engineering-and-computer-science/6-152j-micro-nano-processing-technology-fall-2005/lecture-notes/lecture17.pdf.
- ⁶ B. E. E. Kastenmeier, P. J. Matsuo, J. J. Beulens, and G. S. Oehrlein, *J. Vac. Sci. Technol. A* **14**, 2802 (1996).
- ⁷ S. M. Irving, *Solid State Technol.* **14**, 47 (1971).
- ⁸ T. C. Penn, *Ieee T. Electron Dev.* **26**, 640 (1979).
- ⁹ J. W. Coburn and H. F. Winters, *J. Appl. Phys.* **50**, 3189 (1979).
- ¹⁰ J. Chang and J. P. Chang, *J. Phys. D: Appl. Phys.* **50**, 253001 (2017).
- ¹¹ N. Marchack and J. P. Chang, *J. Phys. D: Appl. Phys.* **44** (2011).
- ¹² S. D. Athavale and D. J. Economou, *J. Vac. Sci. Technol. B* **14**, 3702 (1996).
- ¹³ G. S. Oehrlein, D. Metzler, and C. Li, *Ecs J. Solid State Sc.* **4**, N5041 (2015).
- ¹⁴ K. J. Kanarik, T. Lill, E. A. Hudson, S. Sriraman, S. Tan, J. Marks, V. Vahedi, and R. A. Gottscho, *J. Vac. Sci. Technol. A* **33**, 020802 (2015).
- ¹⁵ A. Agarwal and M. J. Kushner, *J. Vac. Sci. Technol. A* **27**, 37 (2009).

- ¹⁶ R. A. Gottscho, C. W. Jurgensen, and D. J. Vitkavage, *J. Vac. Sci. Technol. B* **10**, 2133 (1992).
- ¹⁷ H. Shin, W. Y. Zhu, V. M. Donnelly, and D. J. Economou, *J. Vac. Sci. Technol. A* **30**, 021306 (2012).
- ¹⁸ W. Y. Zhu, S. Sridhar, L. Liu, E. Hernandez, V. M. Donnelly, and D. J. Economou, *J. Appl. Phys.* **115**, 203303 (2014).
- ¹⁹ S. Sridhar, L. Liu, E. W. Hirsch, V. M. Donnelly, and D. J. Economou, *J. Vac. Sci. Technol. A* **34**, 061303 (2016).
- ²⁰ H. Okano, Y. Horiike, and M. Sekine, *Jpn. J. Appl. Phys. 1* **24**, 68 (1985).
- ²¹ F. A. Houle, *Phys. Rev. B* **39**, 10120 (1989).
- ²² W. Sesselmann, E. Hudeczek, and F. Bachmann, *J. Vac. Sci. Technol. B* **7**, 1284 (1989).
- ²³ S. Samukawa, B. Jinnai, F. Oda, and Y. Morimoto, *Jpn. J. Appl. Phys. 2* **46**, L64 (2007).
- ²⁴ M. Fukasawa, Y. Miyawaki, Y. Kondo, K. Takeda, H. Kondo, K. Ishikawa, M. Sekine, H. Matsugai, T. Honda, M. Minami, F. Uesawa, M. Hori, and T. Tatsumi, *Jpn. J. Appl. Phys.* **51**, 026201 (2012).
- ²⁵ M. Fukasawa, H. Matsugai, T. Honda, Y. Miyawaki, Y. Kondo, K. Takeda, H. Kondo, K. Ishikawa, M. Sekine, K. Nagahata, F. Uesawa, M. Hori, and T. Tatsumi, *Jpn. J. Appl. Phys.* **52**, 05ED01 (2013).
- ²⁶ D. Nest, D. B. Graves, S. Engelmann, R. L. Bruce, F. Weilmboeck, G. S. Oehrlein, C. Andes, and E. A. Hudson, *Appl. Phys. Lett.* **92**, 153113 (2008).

- 27 E. Pargon, M. Martin, K. Mengueli, L. Azarnouche, J. Foucher, and O. Joubert,
Appl. Phys. Lett. **94**, 153113 (2009).
- 28 Z. C. Liu, M. Imamura, A. Asano, K. Ishikawa, K. Takeda, H. Kondo, O. Oda, M.
Sekine, and M. Hori, Appl. Phys. Express **10**, 086502 (2017).
- 29 P. Tian and M. J. Kushner, Plasma Sources. Sci. T. **24**, 034017 (2015).
- 30 P. Tian and M. J. Kushner, Plasma Sources. Sci. T. **26**, 024005 (2017).
- 31 S. Y. Tian, V. M. Donnelly, P. Ruchhoeft, and D. J. Economou, Appl. Phys. Lett.
107, 193109 (2015).
- 32 S. Y. Tian, V. M. Donnelly, and D. J. Economou, J. Vac. Sci. Technol. B **33**,
030602 (2015).
- 33 N. Cabrera and N. F. Mott, Rep. Prog. Phys. **12**, 163 (1949).
- 34 H. F. Winters, J. W. Coburn, and T. J. Chuang, J. Vac. Sci. Technol. B **1**, 469
(1983).
- 35 F. A. Houle, Phys. Rev. Lett. **61**, 1871 (1988).
- 36 T. Kirimura, K. Shudo, Y. Hayashi, Y. Tanaka, T. Ishikawa, and M. Tanaka,
Phys. Rev. B **73** (2006).
- 37 R. Kullmer and D. Bauerle, Appl. Phys. a-Mater. **43**, 227 (1987).
- 38 P. Mogyrosi, K. Piglmayer, R. Kullmer, and D. Bauerle, Appl. Phys. a-Mater.
45, 293 (1988).
- 39 R. B. Jackman, H. Ebert, and J. S. Foord, Surf. Sci. **176**, 183 (1986).
- 40 U. Streller, B. Li, A. Krabbe, H. P. Krause, I. Twesten, and N. Schwentner, J.
Electron Spectrosc. **80**, 49 (1996).
- 41 U. Streller, A. Krabbe, and N. Schwentner, Appl. Phys. Lett. **69**, 3004 (1996).

- 42 U. Streller, B. Li, A. Krabbe, and N. Schwentner, Appl. Surf. Sci. **96-8**, 448
(1996).
- 43 B. Li, U. Streller, H. P. Krause, I. Twesten, and N. Schwentner, J. Appl. Phys. **77**,
350 (1995).
- 44 V. Ney and N. Schwentner, J. Phys.-Condes. Matter **18**, S1603 (2006).
- 45 R. Brunetti, C. Jacoboni, F. Nava, L. Reggiani, G. Bosman, and R. J. J. Zijlstra, J.
Appl. Phys. **52**, 6713 (1981).
- 46 J. P. Chang, J. C. Arnold, G. C. H. Zau, H. S. Shin, and H. H. Sawin, J. Vac. Sci.
Technol. A **15**, 1853 (1997).
- 47 J. P. Chang and H. H. Sawin, J. Vac. Sci. Technol. A **15**, 610 (1997).
- 48 M. Balooch, M. Moalem, W. E. Wang, and A. V. Hamza, J. Vac. Sci. Technol. A
14, 229 (1996).
- 49 J. Hopwood, Plasma Sources. Sci. T. **1**, 109 (1992).
- 50 V. M. Donnelly and J. A. Mccauley, J. Vac. Sci. Technol. A **8**, 84 (1990).
- 51 V. M. Donnelly, D. E. Ibbotson, and C. P. Chang, J. Vac. Sci. Technol. A **10**,
1060 (1992).
- 52 J. A. Mccauley, V. M. Donnelly, M. Vernon, and I. Taha, Phys. Rev. B **49**, 7408
(1994).
- 53 S. Agarwal, A. Takano, M. C. M. van de Sanden, D. Maroudas, and E. S. Aydil, J.
Chem. Phys. **117**, 10805 (2002).
- 54 P. R. I. Cabarrocas, S. Hamma, S. N. Sharma, G. Viera, E. Bertran, and J. Costa,
J. Non-Cryst. Solids **227**, 871 (1998).
- 55 S. Hamma and P. R. I. Cabarrocas, J. Appl. Phys. **81**, 7282 (1997).

- 56 P. G. Snyder, Y. M. Xiong, J. A. Woollam, E. R. Krosche, and Y. Strausser, *Surf. Interface Anal.* **18**, 113 (1992).
- 57 *Handbook of Ellipsometry* (William Andrew, 2015).
- 58 G. E. Jellison, M. F. Chisholm, and S. M. Gorbalkin, *Appl. Phys. Lett.* **62**, 3348 (1993).
- 59 G. E. Jellison, M. Keefer, and L. Thornquist, *Mat. Res. S. C.* **283**, 561 (1993).
- 60 *Practical surface analysis by Auger and X-ray Photoelectron Spectroscopy; Vol. I*, edited by D. Briggs and M. P. Seah (John Wiley & Sons, 1983).
- 61 W. S. M. Werner, *Surf. Interface Anal.* **31**, 141 (2001).
- 62 M. P. Seah, *Surf. Interface Anal.* **44**, 497 (2012).
- 63 M. Kot, Thesis, Brandenburg University of Technology Cottbus - Senftenberg, 2014.
- 64 H. R. T., in *Practical Materials Characterization*, edited by S. M. (Springer, New York, NY, 2014).
- 65 N. Layadi, V. M. Donnelly, and J. T. C. Lee, *J. Appl. Phys.* **81**, 6738 (1997).
- 66 N. Layadi, V. M. Donnelly, J. T. C. Lee, and F. P. Klemens, *J. Vac. Sci. Technol. A* **15**, 604 (1997).
- 67 A. Alyamani and O. M. Lemine, in *Scanning Electron Microscopy*, edited by V. Kazmiruk (InTech. London, 2012).
- 68 G. McMahon, *Analytical instrumentation: A guide to laboratory, portable and miniaturized instruments*, 1st ed. (Chichester: Wiley, 2007).
- 69 J. K. Goldstein and H. Yakowitz, *Practical scanning electron microscopy: Electron and ion microprobe analysis* (New York: Plenum Press, 1975).

- 70 J. K. Goldstein, D. E. Newbury, P. Echlin, and D. C. Joy, *Scanning electron microscopy and x-ray microanalysis*, 2nd ed. (New York: Plenum Press, 1992).
- 71 D. Brabazon and A. Raffer, in *Emerging nanotechnologies for manufacturing*, edited by W. Ahmed and M. J. Jackson (Boston: William Andrew Publishing, 2010).
- 72 D. Bondeson, in *Department of engineering design and materials* (Trondheim: Norwegian University of Science and Technology, 2007).
- 73 D. L. Flamm and V. M. Donnelly, *Plasma Chem. Plasma Process.* **1**, 317 (1981).
- 74 D. L. Flamm, V. M. Donnelly, and D. E. Ibbotson, in *VLSI electronics. Microstructure science.; Vol. 8*, edited by N. G. Einspruck and D. M. Brown (Academic, New York, 1984), p. 189.
- 75 D. M. Manos and D. L. Flamm, *Plasma etching : an introduction* (Academic Press, Boston, 1989).
- 76 K. H. A. Bogart and V. M. Donnelly, *J. Appl. Phys.* **86**, 1822 (1999).
- 77 K. H. A. Bogart and V. M. Donnelly, *J. Appl. Phys.* **87**, 8351 (2000).
- 78 G. C. Smith and A. K. Livesey, *Surf. Interface Anal.* **19**, 175 (1992).
- 79 C. C. Cheng, K. V. Guinn, V. M. Donnelly, and I. P. Herman, *J. Vac. Sci. Technol. A* **12**, 2630 (1994).
- 80 L. J. Whitman, S. A. Joyce, J. A. Yarmoff, F. R. McFeely, and L. J. Terminello, *Surf. Sci.* **232**, 297 (1990).
- 81 T. Takahagi, I. Nagai, A. Ishitani, H. Kuroda, and Y. Nagasawa, *J. Appl. Phys.* **64**, 3516 (1988).
- 82 Z. H. Walker and E. A. Ogryzlo, *J. Appl. Phys.* **69**, 2635 (1991).

- 83 Z. H. Walker and E. A. Ogryzlo, J. Appl. Phys. **69**, 548 (1991).
- 84 E. A. Ogryzlo, D. E. Ibbotson, D. L. Flamm, and J. A. Mucha, J. Appl. Phys. **67**, 3115 (1990).
- 85 M. A. Lieberman, *Principles of Plasma Discharges and Materials Processing* (Wiley, New York, 1994).
- 86 C. Lee, D. B. Graves, and M. A. Lieberman, Plasma Chem. Plasma Process. **16**, 99 (1996).
- 87 D. L. Flamm, in *Plasma Etching: An Introduction; Vol. 1*, edited by D. M. Manos and D. L. Flamm (Academic, Boston, 1989).
- 88 J. P. Chang, A. P. Mahorowala, and H. H. Sawin, J. Vac. Sci. Technol. A **16**, 217 (1998).
- 89 G. S. Oehrlein, Surf. Sci. **386**, 222 (1997).
- 90 K. Nishikawa, K. Ono, M. Tuda, T. Oomori, and K. Namba, Jpn. J. Appl. Phys. 1 **34**, 3731 (1995).
- 91 J. W. Coburn, J. Vac. Sci. Technol. B **12**, 1384 (1994).
- 92 V. M. Donnelly, J. Appl. Phys. **79**, 9353 (1996).
- 93 M. Tuda and K. Ono, Jpn. J. Appl. Phys. 1 **36**, 2482 (1997).
- 94 H. Shin, W. Y. Zhu, L. Xu, V. M. Donnelly, and D. J. Economou, Plasma Sources. Sci. T. **20**, 055001 (2011).
- 95 R. J. Hoekstra and M. J. Kushner, J. Appl. Phys. **79**, 2275 (1996).
- 96 S. Ghosh and N. L. Bauld, Journal of Catalysis **95**, 300 (1985).
- 97 S. A. Vitale, H. Chae, and H. H. Sawin, J. Vac. Sci. Technol. A **19**, 2197 (2001).
- 98 N. L. Bassett and D. J. Economou, J. Appl. Phys. **75**, 1931 (1994).

- 99 J. A. Levinson, E. S. G. Shaqfeh, M. Balooch, and A. V. Hamza, J. Vac. Sci. Technol. A **15**, 1902 (1997).
- 100 S. Qin, M. P. Bradley, P. L. Kellerman, and K. Saadatmand, Rev. Sci. Instrum. **73**, 1153 (2002).
- 101 M. V. Malyshev, V. M. Donnelly, A. Kornblit, N. A. Ciampa, J. I. Colonell, and J. T. C. Lee, J. Vac. Sci. Technol. A **17**, 480 (1999).
- 102 J. M. Lane, F. P. Klemens, K. H. A. Bogart, M. V. Malyshev, and J. T. C. Lee, J. Vac. Sci. Technol. A **18**, 188 (2000).
- 103 V. M. Donnelly and M. V. Malyshev, Appl. Phys. Lett. **77**, 2467 (2000).
- 104 S. Ashida and M. A. Lieberman, Jpn. J. Appl. Phys. 1 **36**, 854 (1997).
- 105 M. V. Malyshev and V. M. Donnelly, J. Appl. Phys. **87**, 1642 (2000).
- 106 S. Ashida, C. Lee, and M. A. Lieberman, J. Vac. Sci. Technol. A **13**, 2498 (1995).
- 107 L. Stafford, O. Langlois, J. Margot, M. Gaidi, and M. Chaker, J. Vac. Sci. Technol. A **25**, 425 (2007).
- 108 W. v. Roosbroeck and W. Shockley, Physical Review **94**, 1558 (1954).
- 109 A. Richter, S. W. Glunz, F. Werner, J. Schmidt, and A. Cuevas, Phys. Rev. B **86** (2012).
- 110 G. Soehnel, Optics Express **23**, 1256 (2015).
- 111 W. Shockley and W. T. Read, Physical Review **87**, 835 (1952).
- 112 R. H. Wu and A. R. Peaker, Solid-State Electronics **25**, 643 (1982).
- 113 H. Z. Fardi, D. W. Winston, R. E. Hayes, and M. C. Hanna, Ieee T. Electron Dev. **47**, 915 (2000).

- ¹¹⁴ J. A. Schuller, E. S. Barnard, W. S. Cai, Y. C. Jun, J. S. White, and M. L. Brongersma, *Nat. Mater.* **9** (2010).
- ¹¹⁵ T. Siyuan, Thesis, University of Houston 2015.
- ¹¹⁶ A. Degiron, H. J. Lezec, W. L. Barnes, and T. W. Ebbesen, *Appl. Phys. Lett.* **81**, 4327 (2002).
- ¹¹⁷ *Introduction to Semiconductor Device Modeling; Vol.*, edited by C. M. Snowden (World Scientific Publisher: Singapore, 1998).
- ¹¹⁸ A. F. Molisch and B. P. Oehry, *Radiation trapping in atomic vapours* (Clarendon Press, New York, 1998).
- ¹¹⁹ J. R. Woodworth, M. E. Riley, V. A. Arnatucci, T. W. Hamilton, and B. P. Aragon, *J. Vac. Sci. Technol. A* **19**, 45 (2001).

Appendices

Appendix A: Related calculations

A.1 Ion collision probability in the sheath

Assuming $T_e \sim 1.5$ eV and $n_e = 1.2 \times 10^{12} \text{ cm}^{-3}$, the Debye length is

$$\lambda_{De} = 743 \sqrt{\frac{T_e}{n_e}} = 8.3 \mu m. \quad (A.1)$$

At $V_0 = -100$ V bias, based on the Child Law sheath model, the sheath thickness is

$$s = \frac{\sqrt{2}}{3} \lambda_{De} \left[\frac{2V_0}{T_e} \right]^{3/4} = 154 \mu m. \quad (A.2)$$

The mean free path $\lambda = 5$ cm for N_2 at pressure of 1 mTorr, so at 60 mTorr the mean free path of the ions is

$$\lambda = \frac{5 \text{ cm}}{60} = 830 \mu m.$$

Then the probability of an ion suffering collision in the sheath is

$$P = 1 - e^{\left(-\frac{s}{\lambda}\right)} = 17\%. \quad (A.3)$$

Similarly, at $V_0 = -30$ V bias, the sheath thickness is $62 \mu m$, and the corresponding collision probability of ions is 7%.

A.2 Charging of SiO₂ mask

The ion flux computed from the ion current density measurements is $f_+ = 1.4 \times 10^{17}$ cm⁻²s⁻¹. For a parallel-plate capacitor with capacitance C , plate separation d , and plate area A , the charge is

$$Q = CV = \frac{k\epsilon_0 A}{d} V, \quad (A.4)$$

where ϵ_0 is the permittivity of free space, and k is the dielectric constant of SiO₂ (=3.9).

This charge is a function of time and is determined by the positive ion flux

$$Q = f_+ Ate, \quad (A.5)$$

where t is time and e is the elemental charge. Equating these expressions for Q , we get

$$V = \frac{f_+ de}{k\epsilon_0} t. \quad (A.6)$$

Assuming $d = 1 \times 10^{-4}$ cm, one obtains $V = 6.5 \times 10^6 t$. Consequently, SiO₂ charges up from -60 V to 0 V in ~ 10 μ s, so above $\sim 10\%$ duty cycle, the SiO₂ mask will charge up to 0 V potential.

A.3 Chlorine consumption

For Si disk, the diameter is $d = 2$ cm, and the area is $S_{\text{disk}} = \pi \text{ m}^2$. For patterned Si sample with 50% density, the exposed Si area is $S_{\text{sample}} = 1 \text{ cm}^2 \times 0.5 = 0.5 \text{ cm}^2$. Then the total exposed Si surface area is $S = \pi - 1 + 0.5 = 2.64 \text{ cm}^2$.

Si number density per unit volume is

$$\frac{2.33 \text{ g/cm}^3}{28 \text{ g/mol}} = 0.08 \text{ mol/cm}^3 = 5 \times 10^{22} \text{ Si/cm}^3.$$

For high flow rate and etching rate = 1,600 nm/min, the number of Si removed per minute is

$$1600 \text{ nm/min} \times 2.64 \text{ cm}^2 \times 5 \times 10^{22} \text{ Si/cm}^3 = 2.1 \times 10^{19} / \text{min}.$$

Assuming SiCl₄ as the etching product, the number of Cl needed per minute is

$$2.1 \times 10^{19} / \text{min} \times 4 = 8.4 \times 10^{19} / \text{min}.$$

For 25 sccm Cl₂ flow rate, the number of Cl₂ per minute provided from the gas feed is

$$25 \text{ sccm} \times 2.6 \times 10^{19} \text{ Cl}_2 / \text{sccm} = 6.5 \times 10^{20} \text{ Cl}_2 / \text{min}.$$

The percent of Cl₂ consumed is

$$\frac{8.4 \times 10^{19}}{6.5 \times 10^{20} \times 2} \% = 6.4\%.$$

Thus, for low flow rate and etching rate 1,600 nm/min, the percent of Cl₂ consumed is 32%, which is 5 times that of high flow rate.

Similarly, for high flow rate and PAE rate = 400 nm/min, the number of Si removed per minute is

$$400 \text{ nm/min} \times 2.64 \text{ cm}^2 \times 5 \times 10^{22} \text{ Si/cm}^3 = 5.3 \times 10^{18} / \text{min}.$$

Assuming SiCl₄ as the etching product, the number of Cl needed per minute is

$$5.3 \times 10^{18} / \text{min} \times 4 = 2.1 \times 10^{19} / \text{min}.$$

The percent of Cl₂ consumed is

$$\frac{2.1 \times 10^{19}}{6.5 \times 10^{20} \times 2} \% = 1.6\%.$$

Then, for low flow rate and PAE rate 400 nm/min, the percent of Cl₂ consumed is 8%.

A.4 IAE yield

For pulsed DC bias with 50% duty cycle, the ion flux is $f_+ = 7 \times 10^{16} \text{ cm}^{-2}\text{s}^{-1}$, so the number of ions striking the sample surface per second is

$$2.64 \text{ cm}^2 \times 7 \times 10^{16} \text{ cm}^{-2}\text{s}^{-1} = 1.85 \times 10^{17} \text{ ion/s}.$$

The Si number density per unit volume is $5 \times 10^{22} \text{ Si/cm}^3$.

At ion energy $\sim 75 \text{ eV}$ and high flow rate, the total etching rate is 1559 nm/min (Figure 5.10). Thus, the IAE rate is 1159 nm/min, since the PAE rate under this condition is 400 nm/min.

The number of Si removed per second due to IAE is

$$\frac{2.64 \text{ cm}^2 \times 5 \times 10^{22} \text{ Si/cm}^3 \times 1159 \text{ nm/min} \times 10^{-7} \text{ cm/nm}}{60 \text{ s/min}} = 2.55 \times 10^{17} \text{ Si/s}.$$

The Si yield is

$$\frac{2.55 \times 10^{17}}{1.85 \times 10^{17}} = 1.3.$$

A.5 Plasma density

Assuming T_e is $\sim 1.5 \text{ eV}$ and ion mass M_i is $\sim 40 \text{ amu}$ for Cl⁺ or Ar⁺, the Bohm velocity u_B is

$$u_B = 9.7 \times 10^5 \times \sqrt{\frac{Te}{M_i}} = 1.9 \times \frac{10^5 cm}{s}. \quad (A.7)$$

So, the plasma density in the bulk is

$$n_e = \frac{f_+}{0.6 \times u_B} = 1.2 \times 10^{12} cm^{-3}. \quad (A.8)$$

A.6 Cl neutral flux

Assuming complete dissociation of molecular chlorine, and a gas temperature of 600 K, a total pressure of 60 mTorr, yields a Cl number density from ideal gas law of

$$\begin{aligned} n_{Cl} &= \frac{N_A P}{RT} = \frac{6.022 \times \frac{10^{23}}{mol} \times 60 \text{ mTorr} \times 10\% \times 2 \times 133.3 \times \frac{10^{-3} \text{ Pascal}}{\text{mTorr}}}{\frac{8.314 J}{mol} \cdot K \times 600 K} \\ &= 2 \times 10^{14} cm^{-3}. \end{aligned} \quad (A.9)$$

The thermal velocity is

$$\begin{aligned} v &= \sqrt{\frac{8k_B T}{\pi m}} = \sqrt{\frac{8 \times 1.38 \times 10^{-23} m^2 kg s^{-2} K^{-1} \times 600 K \times 6.022 \times \frac{10^{23}}{mol}}{3.14 \times 35 \times \frac{10^{-3} kg}{mol}}} \\ &= 6 \times \frac{10^4 cm}{s}. \end{aligned} \quad (A.10)$$

Then, the Cl neutral flux f_{Cl} is

$$f_{Cl} = \frac{n_{Cl} v}{4} = \frac{2 \times 10^{14} cm^{-3} \times 6 \times \frac{10^4 cm}{s}}{4} = 3 \times 10^{18} cm^{-2} s^{-1}. \quad (A.11)$$

A.7 VUV photon flux and PAE yield

The surface area of the cylindrical reactor (ID = 3.125 inch, height h = 13 inch) is

$$A = 2 \times \pi \times \left(\frac{3.125^2}{4} \right) + 2 \times \pi \times \frac{3.125}{2} \times 13 = 922 \text{ cm}^2.$$

For 250 W ICP power, assuming 0.1% of the source power ends up as VUV photons¹¹⁹

and the VUV photon energy is 11.5 eV, the photon flux is

$$f_{\text{photon}} = \frac{250 \text{ W} \times 0.1\%}{922 \text{ cm}^2 \times 11.5 \text{ eV}} = 1.5 \times 10^{14} \text{ cm}^{-2} \text{ s}^{-1}.$$

The number of photons striking the sample surface per second is

$$2.64 \text{ cm}^2 \times 1.5 \times 10^{14} \text{ cm}^{-2} \text{ s}^{-1} = 3.96 \times 10^{14} \text{ ion/s}.$$

The number of Si removed per second for PAE rate at 400 nm/min is

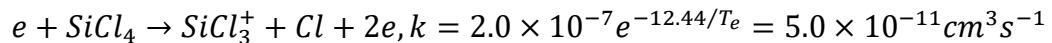
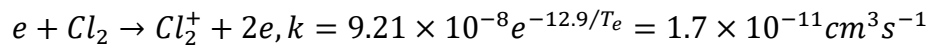
$$\frac{2.64 \text{ cm}^2 \times 5 \times 10^{22} \text{ Si/cm}^3 \times 400 \text{ nm/min} \times 10^{-7} \text{ cm/nm}}{60 \text{ s/min}} = 8.8 \times 10^{16} \text{ Si/s}.$$

Thus, the PAE yield is

$$\frac{8.8 \times 10^{16}}{3.96 \times 10^{14}} = 222.$$

A.8 Electron impact ionization rate constant

Assuming T_e is ~ 1.5 eV, the electron impact ionization rate constants for all possible species^{86,105,106} are as follows:



$$e + SiCl_3 \rightarrow SiCl_3^+ + 2e, k = 1.68 \times 10^{-8} e^{-7.65/T_e} = 1.02 \times 10^{-10} cm^3 s^{-1}$$

$$\begin{aligned} e + SiCl_3 &\rightarrow SiCl_2^+ + Cl + 2e, k = 4.9 \times 10^{-8} e^{\left(-13.9/T_e + 6.89/T_e^2 - \frac{1.45}{T_e^3}\right)} \\ &= 6.7 \times 10^{-11} cm^3 s^{-1} \end{aligned}$$

$$\therefore \sum SiCl_3 = 1.69 \times 10^{-10} cm^3 s^{-1}$$

$$e + SiCl_2 \rightarrow SiCl^+ + Cl + e, k = 8.93 \times 10^{-8} e^{(-9.81/T_e)} = 1.29 \times 10^{-10} cm^3 s^{-1}$$

$$e + SiCl \rightarrow SiCl^+ + 2e, k = 7.5 \times 10^{-8} e^{\left(-\frac{6.79}{T_e}\right)} = 8.1 \times 10^{-10} cm^3 s^{-1}$$

$$e + Ar \rightarrow Ar^+ + 2e, k = 2.3 \times 10^{-14} T_e^{0.68} e^{-15.76/T_e} m^3 s^{-1} = 8.29 \times 10^{-13} cm^3 s^{-1}$$

$$e + Cl \rightarrow Cl^+ + 2e, k = 3 \times 10^{-14} T_e^{0.559} e^{-13.21/T_e} m^3 s^{-1} = 5.63 \times 10^{-12} cm^3 s^{-1}$$

$$\text{So } k_{Ar} : k_{Cl} : k_{Cl_2} : k_{SiCl_4} : k_{SiCl_2} : k_{SiCl_3} : k_{SiCl} = 1.0 : 7 : 20 : 60 : 150 : 205 : 980.$$

Appendix B: Hardware modifications to eliminate contamination and improve run-to-run reproducibility

B.1 Results obtained with chamber contamination

Early experiments, using the existing experimental apparatus, were plagued by sample contamination issues. Sample contamination could be caused by impurities originated from unwanted sputtering of materials inside the plasma chamber, which could lead to artifacts in the experimental results and bring in confusion and difficulties in the data analysis. Early on in this study, carbon, oxygen, fluorine, and metal contamination on the sample surface was routinely detected with XPS. A sample XPS survey spectrum is shown in Figure B.1, which corresponds to a p-type Si sample after etching in pure Cl₂ plasma for 1 minute at a pressure of 4 mTorr with RF power on the sample stage yielding a self-bias of -140 V. The elemental composition on the surface for this particular sample was Si:Cl:C:O:F:Ni = 71:22:5:2:0.4:0.4.

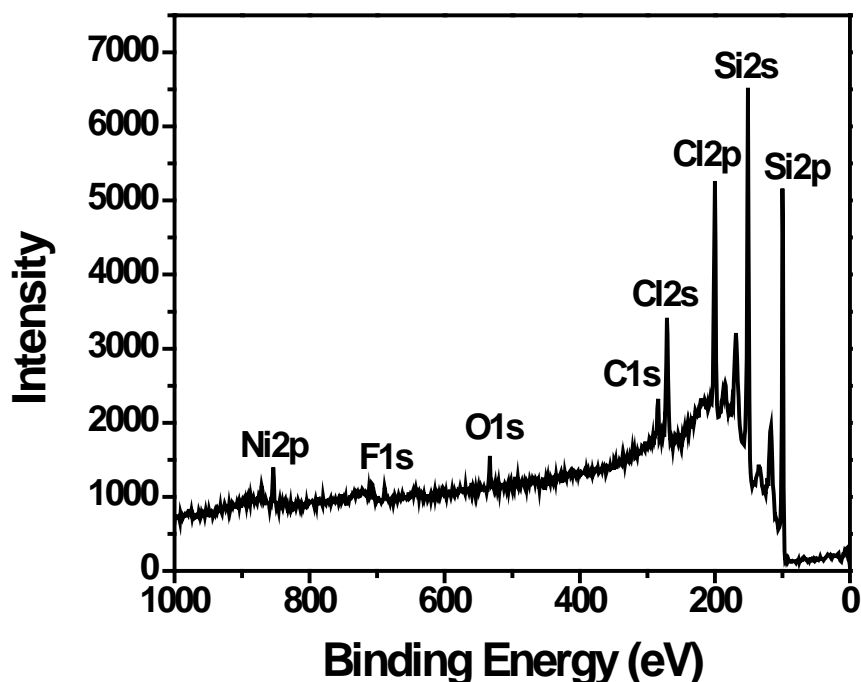


Figure B.1: An XPS survey spectrum of p-type Si after etching in pure Cl₂ plasma for 1 minute at 4 mTorr with RF self-bias voltage -140 V.

XPS high resolution Si(2p) spectrum of a sample after etching in pure Cl₂ plasma with RF self-bias -70V, showed some puzzling features (Figure B.2). When the Si sample was located in the middle of the plasma (black line), the sample surface was rough and appeared black in color. An SEM image of the surface showed the formation of needles perpendicular to the sample surface (Figure B.3). This was probably due to micro-masking by contaminants sputtered from around the sample stage. In this case, XPS is mostly probing the “sidewall” of these needle-like features at take-off-angle 30°, instead of the horizontal surfaces of the sample. The low chlorine content or the lack of silicon chloride tail in the Si(2p) HR spectrum from the feature sidewalls is consistent with the study by Bogart *et al.*⁷⁷ The ion energy dependence of the Cl content is also missing, when the

sample surface is rough due to contamination. For comparison, a case without contamination was shown in Figure 4.11.

On the other hand, moving the sample downstream of the plasma significantly lowered the amount of impurities on the sample surface. The spectrum obtained in this case (red line in Figure B.2) exhibits a chloride tail between 101 and 104 eV under IAE condition, which is consistent with previous studies.^{65,76} In addition, the sample surface after etching was shiny and smooth.

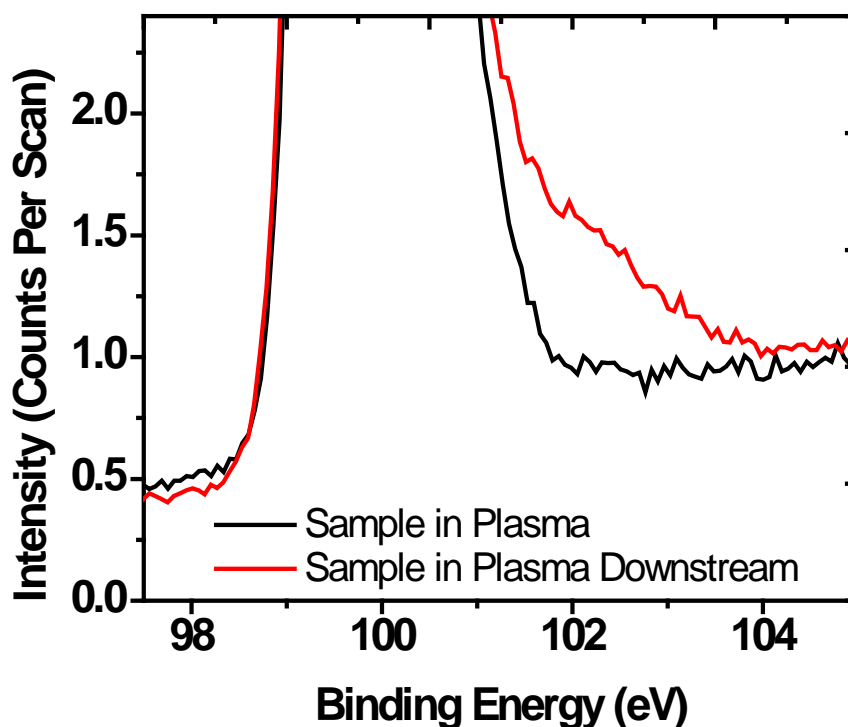


Figure B.2: High resolution Si(2p) spectra at $\theta = 30^\circ$ of sample in the center of the plasma (black) and downstream of the plasma (red), etched with -70 V self-bias voltage.

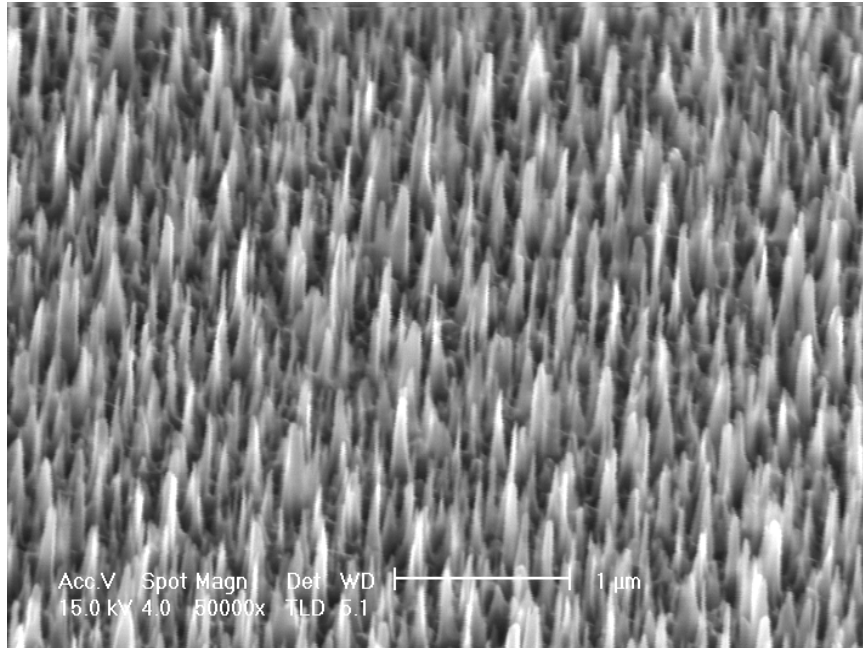


Figure B.3: SEM image (measured at 45° angle) of p-Si after etching for 1minute in Ar/Cl₂ plasma at pressure 60 mTorr with -70 V bias applied on sample.

B.2 Origin of the contaminations

Probable sources of contamination are listed below:

1. Carbon contamination probably came from the carbon tape that was used to bond the Si sample to the sample holder, and a Si donut-shaped disk (2-inch OD and 1-inch ID) to the top SS plate of the sample stage, to prevent metal sputtering. The carbon tape was found to be degraded or partly etched away, especially the carbon tape used to bond the Si donut-shaped disk to the sample stage.
2. Fluorine contamination probably came from sputtering of a Teflon piece used for insulation between the sample and the ground.

3. Oxygen contamination probably came from sputtering of: (a) the chamber wall (alumina), (b) the anodized aluminum film on the periscope frame used for optical emission spectroscopy (OES) measurements, and (c) a Kapton tape used for insulation around the stage.
4. Metal contamination probably came from sputtering of a metal rod used to apply bias to the sample stage, and of the top SS plate of the sample stage.

B.3 Contamination elimination

A series of modifications of the sample stage was done to eliminate various contaminations in the chamber. The sample stage after modifications is shown in Figure B.4. All critical modifications are listed below.



Figure B.4: Sample stage after modifications to eliminate contamination and secondary plasma.

1. To prevent metal sputtering, the SS rod, used to apply bias to the sample stage, was wrapped in ceramic tubing, then grounded SS mesh, then another layer of ceramic tubing. Ceramic-based adhesion (PELCO #16026) was used to cover the exposed metal mesh at the joints.
2. A quartz tubing was placed on the platform in the middle to cover the grounded sample stage acting as a shroud to prevent metal sputtering.
3. Ceramic-based adhesion (PELCO #16026) was used to fill the gap in between the top plate of the stage, ceramic disk, and the grounded sample stage to improve the insulation and heat transfer.
4. A ceramic cap was machined to cover the top plate of the stage to replace the Si donut-shape disk, so carbon tape was not needed for bonding.
5. Carbon tape used to bond sample and SS sample holder was replaced by indium soldering or silver paste (Mung II).
6. Kapton tape and the OES periscope were removed from the chamber. The etching rates were measured by laser interferometry instead of OES.

B.4 Secondary Plasma Elimination

A secondary plasma existed around the SS bias rod between the RF power feedthrough to the top plate of the sample stage prior to the stage modification. It was eliminated by the sandwich structure (ceramic tube, grounded SS mesh, another ceramic tube) wrapped around the rod. The absence of this secondary plasma greatly improved the

run-to-run reproducibility probably due to the elimination of the perturbation of the main plasma from the secondary plasma.

B.5 Source Stability

Source stability was improved, especially at high operating pressure, by adding an adjustable vacuum capacitor on the high voltage end of the coil (shown in Figure 3.2) and increasing the spacing between the source copper coil and the outer chamber shield from 2 inches to 2.75 inches.

All data reported in chapters 4 and 5 were collected after the stage modifications to eliminate contamination and improve run-to-run reproducibility.

